

Mechanics and Dynamics of Multi-Point Threading of Thin-Walled Oil Pipes

by

Mohammad Rezayi Khoshdarregi

BSc. Mechanical Engineering, Sharif University of Technology, 2010

MASc. Mechanical Engineering, The University of British Columbia, 2012

A THESIS SUBMITTED IN PARTIAL FULFILLMENT
OF THE REQUIREMENTS FOR THE DEGREE OF

Doctor of Philosophy

in

THE FACULTY OF GRADUATE AND POSTDOCTORAL
STUDIES

(Mechanical Engineering)

The University of British Columbia

(Vancouver)

July 2017

© Mohammad Rezayi Khoshdarregi, 2017

Abstract

The pipelines used in the offshore extraction of oil and gas are connected by threaded joints. Any geometrical error or vibration marks left on the thread surface during the machining process can lead to stress concentration and fatigue failure of the joint. Such instances in the past have led to massive oil leakage and environmental disasters.

Threading is a form cutting operation resulting in wide chips with complex geometries. Multi-point inserts used in mass production can have different custom profiles on each tooth. The chip thickness as well as the effective oblique cutting angles, cutting force coefficients, and direction of local forces vary along the cutting edge. Since the tool moves one thread pitch over each spindle revolution, the vibration marks left by a tooth affect the chip thickness on the following tooth. Threading of oil pipes imposes additional complexities due to the flexural vibrations of thin-walled pipes, which lead to severe chatter instability.

This thesis develops a novel and generalized model to formulate, simulate, and optimize general multi-point threading processes. A systematic semi-analytical methodology is first proposed to determine the chip geometry for custom multi-point inserts with arbitrary infeed strategies. A search algorithm is developed to systematically discretize the chip area along the cutting edge considering the chip flow direction and chip compression at the corners. The cutting force coefficients are evaluated locally for each element, and the resultant forces are summed up over the engaged teeth.

Multi-mode vibrations of the tool and pipe are projected in the direction of local chip thickness, and the dynamic cutting and process damping forces are calculated locally along the cutting edge. A novel chip regeneration model for multi-point threading is developed, and stability is investigated in frequency domain using Nyquist criterion. The process is simulated by a time-marching numerical method

based on semi-discretization. An optimization algorithm is developed to maximize productivity while respecting machine's limits. The proposed models have been verified experimentally through real scale experiments.

The algorithms are integrated into a research software which enables the industry to optimize the process ahead of costly trials.

Lay Summary

Pipelines used in offshore oil extraction are subject to severe loads and abrasive environment, making them susceptible to failure and leakage. Investigations have shown that the thread connection between the pipes is the weakest point in the pipeline. The accuracy and surface quality of the threads have direct impact on the reliability of the connection.

The threads are generated by incrementally removing material from the pipe to get the final thread shape. This thesis studies the threading process of oil pipes and develops mathematical and physical models to explain the behaviour of this operation. The developed models can simulate the process ahead of costly trials and recommend conditions to achieve highest quality, productivity, and safety of the process.

Preface

This research has been defined and carried out at Manufacturing Automation Laboratory under supervision of Professor Yusuf Altintas to address the challenges observed in threading thin-walled oil pipes. The practical aspect of the problem was put forward by the Research and Development Centre of TenarisTAMSA (Veracruz, Mexico), one of the major manufacturers of steel tubes for the global oil and gas industry. Research methodologies were proposed by the author and approved by the supervisor.

- The cutting force validation experiments presented in Chapter 3 were mostly carried out during author's five-month industrial internship at Metal Cutting Research Department at Sandvik Coromant, Sandviken, Sweden. The experiments were entirely planned and analyzed by the author, and the company provided the cutting tools and machines.
- A concise version of Chapter 3 has been published in [1], "Rezayi Khoshdarregi, M., and Altintas, Y., 2015, Generalized modeling of chip geometry and cutting forces in multi-point thread turning, *International Journal of Machine Tools and Manufacture*, 98, pp. 21-32". The manuscript was written by the first author and edited by the supervisor.
- The experimental modal analyses and chatter tests presented in Chapter 5 were carried out at the R&D center of TenarisTAMSA, Veracruz, Mexico. Experiment planning, measurements, and data analysis were performed by the author, and the company provided the cutting tools and pipes.
- Concise versions of Chapters 4 and 5 have been submitted (at the time of defence) as two related papers to ASME Journal of Manufacturing Science and Engineering, 1) "Khoshdarregi, M., and Altintas, Y., 2017, Dynamics

of multi-point threading: Part I: general formulation”, 2) “Khoshdarregi, M., and Altintas, Y., 2017, Dynamics of multi-point threading: Part II: application to thin-walled oil pipes”.

Table of Contents

Abstract	ii
Lay Summary	iv
Preface	v
Table of Contents	vii
List of Tables	xi
List of Figures	xii
List of Symbols and Abbreviations	xv
Acknowledgments	xxi
Dedicationxxiii
1 Introduction	1
2 Literature Review	6
2.1 Overview	6
2.2 Mechanical Behaviour of Threaded Connections	6
2.3 Mechanics of Form Cutting Operations	7
2.4 Process Dynamics and Chatter Stability	9
2.5 Turning Thin-walled Workpieces	11
2.6 Summary	12

3	Chip Geometry and Cutting Forces	13
3.1	Overview	13
3.2	Discrete Representation of the Cutting Edge	13
3.3	Chip Geometry for General Engagement	15
3.4	Chip Geometry for Partial Root Engagement	20
3.4.1	Re-evaluation of The Left Engagement Point (\mathbf{p}_{sc})	20
3.4.2	Re-evaluation of The Right Engagement Point (\mathbf{p}_{ec})	22
3.4.3	Updating the Upper and Lower Bands	22
3.4.4	Thread Profile After Each Cut	22
3.4.5	Lower Band in Partial Engagement	24
3.5	Systematic Chip Discretization	24
3.6	Cutting Force Calculation	28
3.6.1	Local Oblique Cutting Angles	29
3.6.2	Local Cutting Force Coefficients	32
3.6.3	Total Cutting Forces	35
3.7	Experimental Validation of Mechanics Model	36
3.7.1	Semi-Orthogonal Identification Tests	37
3.7.2	Validation of Threading Force Prediction	39
3.8	Summary	45
4	Dynamics of Multi-Point Threading	47
4.1	Overview	47
4.2	Chip Regeneration Mechanism	47
4.3	Calculation of Dynamic Cutting Forces	48
4.3.1	Dynamic Chip on The Upper Band	48
4.3.2	Dynamic Chip on The Lower Band	51
4.3.3	Dynamic Chip on The First Tooth	52
4.3.4	Total Dynamic Cutting Forces	52
4.4	Calculation of Process Damping Forces	53
4.5	Total Forces on The Insert	56
4.6	Stability Analysis in Frequency Domain	57
4.7	Dynamic Equation of Motion in Time Domain	59
4.8	Time-Marching Numerical Simulation	61
4.8.1	Remarks: Cutter Disengagement Due to Large Vibrations	65

4.9	Sample Simulation Results and Discussions	65
4.10	Numerical Remarks	68
4.10.1	Efficiency of Time-marching Numerical Methods	68
4.10.2	Frequency Resolution in Nyquist Stability Analysis	71
4.11	Process Optimization	73
4.12	Summary	74
5	Threading Thin-Walled Oil Pipes	77
5.1	Overview	77
5.2	Structural Dynamics of Cylindrical Shells	77
5.3	Response of Cylindrical Shells to Threading Loads	78
5.3.1	Dynamic Equation of Motion	79
5.3.2	Sample Time Simulation Results	84
5.4	Application: Threading Oil Pipes	85
5.4.1	Experimental Setup	86
5.4.2	Dynamic Behaviour Across Clamping Chucks	88
5.4.3	Effect of Jaw Configuration	89
5.5	Mode Shape Analysis of Oil Pipes	90
5.5.1	Finite Element Mode Shape Extraction	90
5.5.2	Experimental Mode Shape Extraction	92
5.6	Chatter Experiments	98
5.6.1	Threading Over Several Passes	99
5.6.2	Threading at Different Infeed Values	102
5.6.3	Threading With V-profile Insert	104
5.6.4	Remarks: Change in Pipe Dynamics During Threading	104
5.7	Chatter Suppression Strategies	106
5.7.1	Effect of Additional Damping	107
5.7.2	Using Different Spindle Speeds For Subsequent Passes	109
5.8	Threading Toolbox Simulation Software	110
5.9	Summary	111
6	Conclusions and Future Directions	113
6.1	Summary and Contributions	113
6.2	Future Research Directions	115

Bibliography	117
A Mode Shape Extraction From ANSYS	125

List of Tables

Table 3.1	Parameters in the semi-orthogonal identification tests	38
Table 3.2	Threading with V-profile insert at radial infeed of 0.15 mm/pass .	42
Table 3.3	Threading with V-profile insert at radial infeed of 0.3 mm/pass .	42
Table 3.4	Threading with V-profile insert at flank infeed of 0.15 mm/pass .	43
Table 3.5	Threading V-profile at alternate flank infeed of 0.15 mm/pass . .	43
Table 3.6	Threading with single buttress insert at 0.075 mm/pass	45
Table 3.7	Measured forces in threading with twin buttress insert	45
Table 4.1	Dynamic parameters of the workpiece used in simulations.	66
Table 4.2	Minimum discretization intervals for time-marching simulations .	69
Table 4.3	Optimization constraints for the case study with V-profile insert .	74
Table 4.4	Optimization results and the limiting factors	74
Table 5.1	Measured dynamic parameters of the dominant mode in pipes D7	93
Table 5.2	Comparison of experimental and predicted stability conditions . .	101
Table 5.3	Predicted stability charts at different infeed values	104
Table 5.4	Predicted stability charts for three-point V-profile insert	105
Table 5.5	Dynamic parameters of pipe D13 before and after threading . . .	106

List of Figures

Figure 1.1	Threaded connection between oil pipes	1
Figure 1.2	Different types of infeed plans in thread turning operations . . .	3
Figure 1.3	Local forces at different locations along a threading chip.	4
Figure 1.4	Chatter vibrations and the resultant surface finish in threading. .	5
Figure 3.1	Tool and insert coordinate systems.	14
Figure 3.2	Definitions of radial infeed and depth of cut	16
Figure 3.3	Calculation of lower band for different cases	17
Figure 3.4	Chip boundaries and thread profile in partial root engagement . .	21
Figure 3.5	Overlapping of chip flow lines due to chip interference	25
Figure 3.6	Search algorithm and forming the chip discretization lines. . . .	26
Figure 3.7	Sample chip discretization results	28
Figure 3.8	Sensitivity of chip modelling to the discretization length	28
Figure 3.9	Local oblique cutting parameters and cutting forces	29
Figure 3.10	Sample effective oblique angles for V-profile and buttress inserts	31
Figure 3.11	Local and total forces exerted on the tool	32
Figure 3.12	Edge vectors defining the chip elements.	33
Figure 3.13	Ploughing and the effect of edge radius.	35
Figure 3.14	Experimental setup for the semi-orthogonal tests	37
Figure 3.15	Experimentally identified cutting force coefficients	39
Figure 3.16	Experimental setup for the threading experiments	39
Figure 3.17	Measured cutting forces for single V-profile insert	41
Figure 3.18	Measured cutting forces for single and twin buttress inserts . . .	44
Figure 4.1	Chip regeneration mechanism in multi-point thread turning. . . .	49
Figure 4.2	Dynamic chip area due to the current and previous vibrations. .	50

Figure 4.3	Chip regeneration on the first tooth.	52
Figure 4.4	Local process damping forces in threading.	54
Figure 4.5	Semi-discretization of delay differential equations	62
Figure 4.6	Insert geometry and workpiece dynamics used in the simulation	65
Figure 4.7	Simulated stability charts for three-point V-profile insert	67
Figure 4.8	Comparison of Semi-discretization and Euler's methods	69
Figure 4.9	Sensitivity of the stability lobes to numerical discretization	70
Figure 4.10	Nyquist plots with different frequency resolutions	72
Figure 4.11	Simulated results for the optimized plan	75
Figure 5.1	Vibration modes of a clamped thin-walled workpiece.	78
Figure 5.2	Response of cylindrical shells to machining loads.	79
Figure 5.3	Simulated shell response under threading loads	85
Figure 5.4	Experimental setup for the chatter threading tests	86
Figure 5.5	Pipes and the cutting inserts used in the experimental tests.	87
Figure 5.6	Measurement devices used in the experimental threading tests	87
Figure 5.7	Effectiveness of chuck clamping in vibration isolation	88
Figure 5.8	Effect of jaw configuration on pipe dynamic	89
Figure 5.9	Finite element modal analysis of pipe D13	91
Figure 5.10	Grids for experimental mode shape analysis.	92
Figure 5.11	Circumferential mode shape analysis of pipe D13	94
Figure 5.12	Axial mode shape analysis of pipe D13	95
Figure 5.13	Circumferential mode shape analysis of pipe D7	96
Figure 5.14	Axial mode shape analysis of pipe D7	97
Figure 5.15	Parameters affecting chatter stability in threading oil pipes.	98
Figure 5.16	Measured FRFs before each threading set	99
Figure 5.17	Experimental results for threading test Set 1	100
Figure 5.18	Experimental results for threading test Set 2	101
Figure 5.19	Experimental results for threading test Set 3	102
Figure 5.20	Experimental results at different infeed values	103
Figure 5.21	Experimental results with three-point V-profile insert	105
Figure 5.22	Change in the FRF of pipe D13 after a threading pass	106
Figure 5.23	Effect of the damping ring on pipe dynamics	107
Figure 5.24	Effect of the damping ring on stability	108

Figure 5.25	Effect of adding rubber between the pipe and the clamping jaws	109
Figure 5.26	Effect of using different speeds for chatter suppression	110
Figure 5.27	User interface of the developed <i>Threading Toolbox</i> software . .	112

List of Symbols and Abbreviations

Symbols

\mathbf{A}_0	time-invariant state matrix
A_c	area of chip element
A_{cm}	cross section of compressed material under flank face
A_{dl}, A_{du}	dynamic chip area on lower and upper bands
a	thread depth
\mathbf{B}_c	current state matrix
\mathbf{B}_d	delayed state matrix
$\mathbf{b}_l, \mathbf{b}_u$	local width vectors on lower and upper bands
$\mathbf{C}_{m,1}$	modal structural damping matrix
$\mathbf{C}_{m,2}$	modal process damping matrix
\mathbf{C}_p	equivalent process damping coefficient matrix
d_w	workpiece diameter
du	discretization length
\mathbf{e}_r	unit radial direction vector
\mathbf{F}_c	total cutting force vector
\mathbf{F}_d	dynamic cutting force vector
$\mathbf{F}_{dl}, \mathbf{F}_{du}$	local dynamic cutting force vectors on lower and upper bands
F_{fc}, F_{rc}, F_{tc}	feed, radial, and tangential cutting forces
\mathbf{F}_{Gr}	generalized radial force vector
\mathbf{F}_p	process damping force vector
\mathbf{F}_{pf}	process damping force in feed direction
\mathbf{F}_{pt}	process damping force in tangential direction
$\mathbf{F}_{p,L}$	local process damping force vector

F_s	static cutting force vector
$F_{s,L}$	local static cutting force vector
F_{sm}	modal static cutting force vector
F_u	orthogonal friction force
F_v	orthogonal normal force
f_a	axial feedrate
f_{cr}	radial force at cutting point
\mathbf{G}	matrix of relative FRFs between tool and workpiece
\mathbf{G}_r	generalized radial dynamics of cylindrical shell
\mathbf{G}_p	three-dimensional FRF matrix at point p
G_{p_k, q_n}	cross FRF between DOFs p_k and q_n
$\mathbf{G}_t, \mathbf{G}_w$	FRF matrices of tool and workpiece
g_j	boolean function for tooth entry
\mathbf{h}	local chip thickness vector
\bar{h}	local average chip thickness
$\tilde{\mathbf{h}}$	local candidate chip thickness vector
h_{dl}, h_{du}	dynamic chip thickness on lower and upper bands
h_p	thread pitch
i	index of lower band point
i_c	number of waves in circumferential pattern
i_k	index of lower band point paired with point k of upper band
i_m	index of centre point of moving window
i_p	index of previous selected point of lower band
j	tooth number
j_l	number of half-waves in axial pattern
$\mathbf{K}_{dc}, \mathbf{K}_{dd}$	equivalent current and delayed dynamic force coefficient matrices
\mathbf{K}_e	equivalent cutting force coefficient vector for chip element
K_{fc}, K_{rc}, K_{tc}	feed, radial, and tangential cutting force coefficients
$\mathbf{K}_{mc,1}$	modal squared natural frequency matrix
$\mathbf{K}_{mc,2}$	modal current dynamic cutting force coefficient matrix
\mathbf{K}_{md}	modal delayed dynamic cutting force coefficient matrix
K_{sp}	process damping indentation force coefficient
K_u, K_v	friction and normal cutting force coefficients

\mathbf{K}_{uv}	vector of orthogonal cutting force coefficients
k	index of cutting edge point
k_{c1}	Kienzle coefficient
$k_{s,i}$	modal stiffness of mode i
L	length of workpiece after chuck
$\bar{\mathbf{L}}_l, \bar{\mathbf{L}}_u$	local unit vector tangent to lower and upper bands
$\mathbf{L}_l, \mathbf{L}_u$	local vectors tangent to lower and upper bands
L_w	width of wear land on flank face
m	number of discretizations around circumference of workpiece
m_c	Kienzle coefficient
m_i	modal mass of mode i
m_t, m_w	number of modes of tool and workpiece
\mathbf{N}_c	shape function
${}^j N_e$	number of elements on tooth j
N_p	total number of discrete edge points
N_t	total number of teeth on insert
N_l, N_u	number of discrete points of lower and upper bands
n	spindle speed
n_g	total number of grid points
n_p	pass number
\mathbf{P}	discrete representation of cutting edge in global coordinates
\mathbf{P}_{IC}	discrete representation of cutting edge in insert coordinates
${}^j_{n_p} \mathbf{P}_l, {}^j_{n_p} \mathbf{P}_u$	discrete representation of lower and upper bands on tooth j and pass n_p
$\mathbf{P}_{lL}, \mathbf{P}_{lM}, \mathbf{P}_{lR}$	discrete representation of left, middle, and right segments of lower band
${}^j_{n_p} \mathbf{P}_f$	discrete representation of thread profile on tooth j and pass n_p
\mathbf{P}_{fs}	shifted previous profile
P_{ec}, P_{ep}	current and previous intersection points on right edge
P_{sc}, P_{sp}	current and previous intersection points on left edge
$P_{e,u1}, P_{e,u2}$	first and second candidate points on right engagement (upper band)
$P_{s,u1}, P_{s,u2}$	first and second candidate points on left engagement (upper band)
$P_{e,l}$	temporary candidate for right engagement (lower band)
$P_{s,l}$	temporary candidate for left engagement (lower band)
\mathbf{Q}_r	generalized radial vibration vector

\mathbf{q}	relative vibration vector between tool and workpiece
q_{cr}	radial vibration at cutting point
q_i	radial vibration at point i
\mathbf{q}_t	vibration vector of tool
\mathbf{q}_w	vibration vector of workpiece
$R_{kl,i}$	residue of mode i in FRF between points k and l
r_ε	edge radius of cutting edge
\mathbf{S}	static forcing function vector
S_l, S_u	projection of candidate chip thickness on lower and upper bands
T	spindle period
\mathbf{T}_{IG}	insert to global transformation
\mathbf{T}_{LG}	local (TFR) to global transformation
\mathbf{T}_{ob}	orthogonal to oblique transformation
\mathbf{T}_{sc}	transformation from shell coordinates to tool CS
t	time
t_0	initial time
t_w	wall thickness of workpiece
$\mathbf{U}_{fc}, \mathbf{U}_{rc}, \mathbf{U}_{tc}$	unit direction vectors of local cutting forces
$\mathbf{U}_{fl}, \mathbf{U}_{fu}$	chip thickness direction on lower and upper bands
$\hat{\mathbf{U}}_t, \hat{\mathbf{U}}_w$	mass-normalized mode shape matrix of tool and workpiece
$\mathbf{U}_{p,i}$	mass-normalized mode shape vector of point p in mode i
$\hat{\mathbf{U}}_r$	mass-normalized radial mode shape matrix
u	subscript for friction orthogonal direction
$u_{pk,i}$	mass-normalized eigen value of k th DOF of node p in mode i
V_{cm}	volume of compressed material under flank face
\mathbf{V}_f	axial velocity vector due to tool feed
\mathbf{V}_t	total cutting velocity vector
\mathbf{V}_w	circumferential velocity vector at workpiece surface
v	subscript for normal orthogonal direction
XYZ	global CS
$X'Y'Z'$	insert CS
y_w	coordinate of workpiece surface line in insert CS
Y_t	coordinate of tip of final tooth in insert CS

α	local effective rake angle
α_0	nominal rake angle of insert
$\bar{\alpha}$	local unit vector normal to rake face
β_l, β_u	corner angles on lower and upper bands
β_s	summation of corner angles
Γ	combined modal displacement vector of tool and workpiece
γ	local effective clearance angle
γ_0	nominal clearance angle of cutting edge
$\bar{\gamma}$	local unit vector normal to clearance face
Δa	radial infeed
Δt	time step
$\Delta \omega$	frequency resolution
ε_{fx}	axial infeed offset
ζ	damping ratio
η	chip flow angle
θ	local approach angle
θ_{FL}	flank angle
θ_M	deviation angle in modified flank infeed
Λ	characteristic function
λ	inclination angle
μ	Coulomb friction coefficient between tool and workpiece
ρ	helix angle of thread, shim angle
φ	circumferential angle
Ψ	modal displacement vector
Ψ_r	modal radial displacement vector
Ω	state vector
ω	frequency
ω_c	chatter frequency
ω_n	natural frequency
ω_{sp}	spindle rotation frequency

Abbreviations

CAD	Computer-Aided Design
CAM	Computer-Aided Manufacturing
CS	Coordinate System
DDE	Delay Differential Equation
DOF	Degree of Freedom
FEM	Finite Element Method
FFT	Fast Fourier Transform
FRF	Frequency Response Function
MAL	Manufacturing Automation Laboratory
MPa	Mega Pascal
ODE	Ordinary Differential Equation
SD	Semi-discretization
TFR	Tangential, Feed, Radial
TPI	Thread Per Inch

Acknowledgments

First and foremost, I would like to sincerely thank my supervisor, professor Yusuf Altintas, who has been the greatest source of support, encouragement, and inspiration for me over the past seven years of my Master's and PhD studies at the Manufacturing Automation Laboratory. He has created an environment in MAL where everyone feels safe, valued, and motivated.

I am also thankful to the members of my PhD supervisory committee, Dr. Hsi-Yung Feng, Dr. A. Srikantha Phani, and Dr. Reza Vaziri for their valuable input on different technical aspects of this thesis.

This research has been partly sponsored by TenarisTAMSA, Veracruz, Mexico. I owe special thanks to Dr. Ramón Aguilar, manager of Process Development and Mechanical Solutions Group, for providing industrial input and coordinating my on-site experiments during my visit. I am also grateful to the engineers and machining technicians especially Omar, Antonio, Naum, and Octavio for their kind help with the experiments.

Most of the cutting tools used for the experiments in this research have been kindly provided by Sandvik Coromant, Sweden. I am deeply grateful to the engineers and technicians at Coromant for sharing their experience and knowledge during my five-month industrial internship in the company. Special thanks to Mr. Mikael Lundblad and Dr. Anders Liljerehn for scheduling my experiments and offering consultation. I thank Sandvik Coromant for providing housing, and NSERC-CANRIMT for covering my travel expenses during the internship.

I thank DMG Mori for providing a Mori Seiki NT3150 Mill Turn Centre to MAL. The machine has been extensively used for preliminary verification of the models in this thesis.

The past seven years at MAL have been full of great memories. I feel absolutely lucky to have got the chance to work with many passionate students and scholars.

I am particularly grateful to Dr. Keivan Ahmadi, former post-doctoral fellow, for preparing a preliminary code which I used as a starting point for my research. I also thank our software engineer, Mr. Byron Reynolds, for his collaboration in developing a user interface for my threading simulation engine.

Last but not least, I am indebted to my family for their unconditional support throughout all these years, for believing in me, and for allowing me to go after my dreams no matter where they take me.

To my family for their unconditional support...

Chapter 1

Introduction

Threaded connections are widely used in industry in making impermanent joints. Internal and external threads are generated either by forming (plastic deformation) [2] or thread cutting (tapping [3], machining [4]). While higher surface hardness can be achieved in thread forming, cutting operations are more suitable for precision applications. In contrast to conventional tapping, thread machining such as turning and milling operations provides easier chip removal and more control over the cutting parameters, thus results in improved accuracy, surface quality, and productivity.

Drill pipes, tubes, and casings used in the exploration and extraction of oil and gas from deep offshore reservoirs are connected through threaded joints as illus-

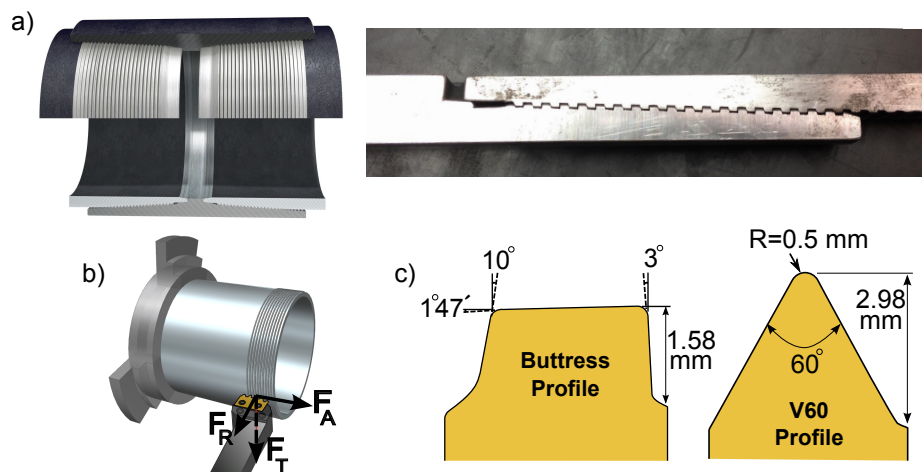


Figure 1.1: a) Threaded connection between oil pipes, b) schematic thread turning operation, c) sample API buttress and API V60 profiles.

trated in Figure 1.1.a. The pipelines must typically reach few kilometres deep in the ocean where they are subject to high pressure, torque, cyclic stresses, varying internal pressure, and severe abrasive wear. Based on finite element and experimental investigations, the threaded joints are the weakest point in the pipelines. The threads are cut using turning operations (Figure 1.1.b) on large scale industrial lathes. Any form error or chatter marks on the thread surface left during the machining operation can initiate fatigue failure and leakage of the joint.

Thread specifications and tolerances are regulated mainly based on Spec 5B of American Petroleum Institute (API) standard [5]. Figure 1.1.c shows two types of threads commonly used in oil and gas industry: API V60 profile for shouldered connections, and API Buttress profile for casings and tubes. These two profiles are extensively used in this thesis for demonstrations, but the developed models are generalized and can be used for any custom profile.

As shown in Figure 1.1.c, the depth of the thread is typically around 1.5 mm to 3 mm. Due to the limited power of machines, structural flexibilities of the setup, and chip removal problems, the entire depth of the thread cannot be cut in one axial travel (pass) of the cutting tool along the pipe axis. Normally, the thread is cut over 6-12 passes, the first few of which are for roughing, and the final passes are for finishing. As illustrated in Figure 1.2.a for a V-profile thread, there are four main strategies which determine how much and in which direction the cutting tooth penetrates into the thread over each pass. The arrows in the figure represent the infeed direction. Each of these strategies, also called *Infeed Plans*, has certain advantages and disadvantages. Radial infeed is the simplest strategy and can be performed by all conventional lathes. It also results in cancellation of axial forces due to equal chip thickness on side edges. Figure 1.2.b shows the cross section of the actual chip for the first, intermediate, and final passes when threading with a V-profile insert at radial infeed of 0.15 mm/pass. It can be seen that towards final passes, a long section of the tooth is engaged in the cut, which leads to poor chip formation.

Flank infeed, on the other hand, cuts with only one side of the tooth. Even though the thickness of the chip is twice as the one in radial infeed (assuming same chip area), the cutting section has a smaller width and a more straight profile. The problem, however, is that not only the insert wears out unevenly but also the two sides of the finished thread will have different surface characteristics. Alternate

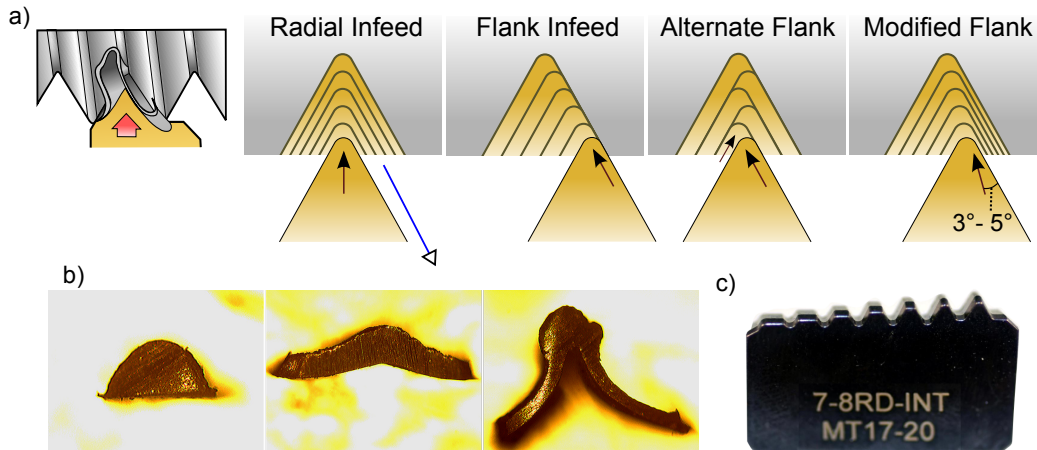


Figure 1.2: a) Different types of infeed plans, b) cross section of actual chip (microscope image), c) sample multi-point threading insert (Ningbo Sanhan).

flank infeed is designed to mitigate this problem by alternating between the sides of the tooth and cut surface.

The main issue in both flank and alternate is that over each pass one side of the cutting edge (free edge) is constantly rubbing against the thread surface, resulting in elevated temperatures, faster tool wear, and degraded surface quality. Modified flank solves this problem by combining the advantages of the other three strategies; due to cutting with both edges, the wear and surface quality is relatively even on both sides. Since the chip on one side is very thin and easy to deform, the chip evacuation is also superior to radial infeed. Most modern machine tools can automatically perform all these infeed strategies. Similar infeed plans can be defined for other types of profiles to change the chip load distribution. In this thesis, a generalized model has been developed which can systemically determine the chip geometry for any custom profile and arbitrary infeed strategy.

In order to improve the productivity of threading operations, especially in mass production such as oil and gas industry, it is common to use multi-point inserts (Figure 1.2.c). In one axial travel of the tool along the workpiece, the first few teeth perform rough cutting and the final teeth gradually finish the surface. In some cases, more than one pass might be still needed. Unlike single-point threading, multi-point inserts are designed for only a specific pitch. Custom infeed strategies can be integrated in the design of multi-point inserts by shifting each tooth in the axial (feed) direction relative to its previous tooth. This axial shift does not change

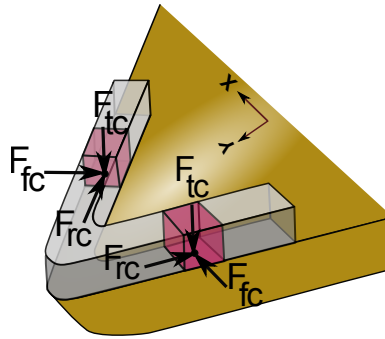


Figure 1.3: Local forces at different locations along a threading chip.

the pitch of the thread since the insert still travels one pitch per spindle revolution.

Figure 1.3 illustrates a sample threading chip and the local cutting forces. The chip thickness as well as the cutting force coefficients, oblique cutting angles, and the direction of local forces can vary significantly along the cutting edge. In this thesis, a systematic chip discretization method is proposed which allows local evaluation of cutting forces. The developed technique can form the elements based on the local chip flow direction while considering the chip compression at sharply curved segments.

Due to the structural flexibilities of the tool and workpiece, any change in the cutting forces can cause the setup to vibrate. As illustrated in Figure 1.4, the current vibrations and the vibration marks left from the previous cut lead to variation in the instantaneous chip thickness. The closed loop interaction between the cutting forces and the structure can lead to unstable chip regeneration (regenerative chatter). Dynamics and stability of multi-point threading is different than regular turning in that each tooth is affected by the previous vibration marks left by a different tooth. Due to the variation of local approach angle in threading inserts, the effect of current and previous vibrations must be analyzed locally at each point along the cutting edge.

Relative vibrations between the tool and workpiece also result in additional damping in the system. The effect of process damping is especially more significant when the rotation frequency of the spindle is considerably smaller than the structural vibration frequency. Thread turning operations are often run at low spindle speeds (below 1000 rpm) since the tool has to move one thread pitch over each spindle revolution. Process damping has therefore a significant effect on chatter stability limits in threading operations. Threading of oil pipes imposes additional

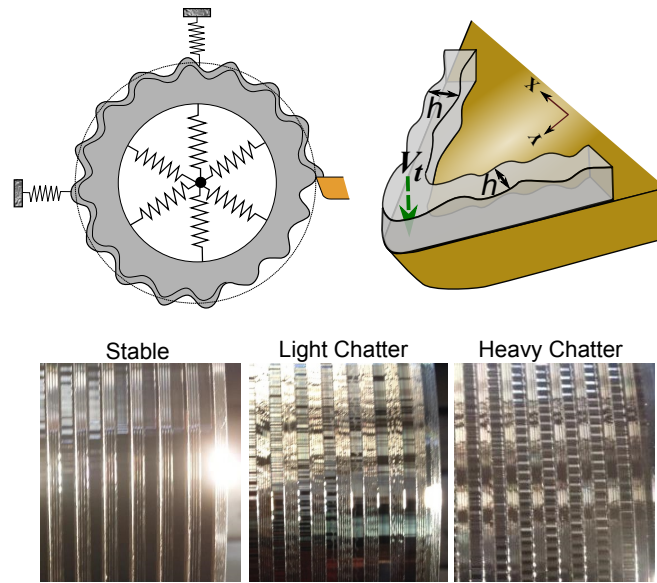


Figure 1.4: Chatter vibrations and the resultant surface finish in threading.

complexities due to the shell dynamics of thin-walled pipes. This thesis develops a generalized dynamic model and predicts the chatter stability diagrams for thread turning with custom multi-point inserts subject to three-dimensional flexibilities of the tool and workpiece. The model is extended to threading thin-walled cylindrical shells as well.

The rest of this thesis is structured as follows. Chapter 2 reviews some of the previous literature related to threading operations. Chapter 3 presents the mechanics of multi-point threading process. A generalized methodology is first proposed to determine the chip boundaries for custom multi-point inserts. The chip is discretized along the cutting edge, and the cutting forces are evaluated locally for each chip element. The mechanics model is validated experimentally.

Generalized dynamics of multi-point threading is developed in Chapter 4. The dynamic equation of motion is derived in time and frequency domains, and the stability of the process is investigated. An optimization algorithm is presented to find the optimum infeed settings subject to user-defined constraints.

The model is extended in Chapter 5 to threading thin-walled workpieces with dominant shell vibrations. The proposed dynamic model is validated experimentally through extensive tests on real scale oil pipes. The thesis is concluded in Chapter 6 by summarizing the research contributions and possible future directions.

Chapter 2

Literature Review

2.1 Overview

This chapter reviews some of the past research related to threading operations. Section 2.2 discusses the effect of machining parameters on mechanical characteristics of threaded connections. Section 2.3 presents the previous methodologies proposed for calculation of chip geometry and cutting forces in general form cutting operations. Dynamics and chatter stability of turning and threading operations are discussed in Section 2.4, followed by more specific application to thin-walled cylindrical workpieces in Section 2.5. The chapter is concluded by the summary in Section 2.6.

2.2 Mechanical Behaviour of Threaded Connections

Researchers have extensively studied mechanical characteristics of threaded joints in the pipelines. Using finite element analysis, Shahani and Sharifi [6] showed that the threads near the shoulder and free end of drill pipes bear the maximum load. Lu and Wu [7] carried out fractographic analysis on the joints between drill pipes, and observed that fatigue cracks nucleated mostly at the root of the first thread. Yuen et al. [8] studied stress distribution in the thread connection during the make and break process of oil pipes and showed that the reliability of the connection can be improved by decreasing the local stress concentration and improving the rigidity of thread surface. Abrahmi et al. [9] analyzed the effect of threading process on the mechanical and tribological behaviour of triangular threads. They concluded that

compared to machining operations, rolling processes lead to improved mechanical resistance of the thread joints. However, the accuracy and efficiency of rolling process is not satisfactory for oil and gas applications.

Researchers have also studied the effect of machining parameters on thread performance. Fetullazade et al. [10] carried out several sets of thread turning experiments on SAE 4340 steel at different values of cutting speed, depth of cut, and tool wear. They measured the residual stresses at the root of the machined thread using electro-chemical layer removal technique, and observed residual stress ranging from 600MPa to 1450MPa as compared to the material tensile strength of 850MPa. They also found strain hardening in the range of 320HV-430HV at the thread root as compared to the base hardness of 260HV. Akyildiz and Livatyali [11] investigated the effect of machining parameters on fatigue strength of test specimens threaded on a turning machine. They analyzed the endurance limit of the threaded parts using a rotary fatigue test machine, and concluded that higher cutting velocity and larger tool wear improves the fatigue strength of the threads due to strain hardening.

2.3 Mechanics of Form Cutting Operations

The toothed profile of the cutter in form cutting operations such as threading, hobbing and gear shaping can generally result in multi-flank chips. Klocke et al. [12] developed a finite element-based machining simulation to model the chip formation, thermal and stress distribution, and tool wear along the cutting edge in multi-flank form cutting. Cutter-workpiece engagement can be obtained using solid or discrete geometric modelling kernels [13]. Bouzakis [14] used a solid kernel in SolidWorks® to model the chip geometry in hobbing. Although solid modelling provides highly accurate representation due to its analytical approach, the computational load is intensive. Discrete representation of the engagement using meshed geometries, on the other hand, can provide fast yet reliable approximate solutions. Brecher et al. [15] modelled the chip geometry in bevel gear cutting using the discrete volume representation of the tool and workpiece. Erkorkmaz et al. [13] used multi-dexel volume representation to extract the cutter-workpiece engagement at each time step during gear shaping operation. Unlike the methods used in the research cited above, this thesis uses the kinematics of the process and geometry of the tool to semi-analytically determine the boundaries of the chip on each tooth in

threading with multi-point inserts.

Thread milling is used mainly in generating internal threads especially for applications involving asymmetrical workpieces or hard-to-cut materials. Araujo et al. [4] simplified thread milling as a common end milling operation by ignoring the feeding motion of the tool along the hole axis (z-direction). Fromentin and Poulachon [16, 17] derived a mathematical model to describe the tool envelope profile, cutting angles, and uncut chip thickness in thread milling. Jun and Araujo [18] developed a force model for “thrilling” operation, which performs drilling and threading with the same tool. Wan and Altintas [19] studied the mechanics and dynamics of thread milling processes, and modelled the varying cutter-workpiece engagement based on the kinematics of the process. They also predicted process stability along the helical threading path using semi-discretization method [20]. Araujo et al. [21] presented geometrical and cutting force analysis for thread milling of API threads, and analyzed the surface roughness at different vertical positions for different feedrates. Unlike for thread milling and other form cutting operations, the mechanics of general thread turning processes have not been studied systematically before.

Researchers have used different approaches for modelling the chip geometry in typical turning operations. Eynian and Altintas [22] divided the chip area based on the linear and curved edges of the insert. Reddy et al. [23], Lazoglu et al. [24], and Ozlu and Budak [25] obtained a more accurate approximation through discretization of the chip along the cutting edge. The chip geometry in thread turning is more complicated and cannot be modelled using the approaches cited above. Akyildiz and Livatyali [26] presented a force calculation method for thread turning based on chip discretization, but their method is limited to V-profile with radial infeed. In addition, they used a linear cutting force coefficient model, and observed considerable discrepancy between the simulated and measured forces especially towards the final passes. Akyildiz [27] reported the change in the shear angle [28] over subsequent threading passes as the main source of this discrepancy. Kafkas [29] carried out an experimental study on cutting forces in thread turning, and observed an increase in the cutting force coefficients over deeper passes; chip interference was claimed to be the reason for this behaviour.

This thesis develops a generalized systematic model which can determine the chip geometry and predict the cutting forces for thread turning with custom multi-point inserts and arbitrary infeed plans.

2.4 Process Dynamics and Chatter Stability

Instability of machining processes due to self-excited vibrations, known as chatter, was first recognized and modelled by Taylor [30], Tobias [31], Tlustý [32], and Meritt [33]. They described the dynamics of the process as delay differential equations. Fundamentals of machining dynamics have been summarized by Schmitz and Smith in [34]. Researchers have developed numerous methods to solve the process dynamic equations and predict chatter stability for different operations, as reviewed by Altintas and Weck [35]. Minis and Yanushevsky [36] proposed a frequency domain solution based on Fourier analysis and Floquet's theory. Altintas and Budak [37] approximated the direction factors by their average, and proposed an analytical zero-order solution. Insperger and Stepan [20, 38] developed a time domain semi-discretization method which approximates the delay differential equation by a series of ODEs. In this method, the delay state and the time-varying coefficient matrices are approximated numerically. Ding et al. [39, 40] proposed full-discretization and numerical integration methods to analyze the stability of the process. Asl and Ulsoy [41] solved the linear delay differentials using Lambert functions while Butcher et al. [42] employed Chebyshev polynomials and collocation methods. Mann et al. [43] used Temporal Finite Element Analysis (TFEA) for simultaneous prediction of stability and surface location error in milling operations. Eksioğlu et al. [44] implemented an extended version of semi-discretization method to predict the stability and surface location errors in machining thin-walled workpieces. Honeycutt and Schmitz [45] proposed a metric for automated stability identification in time domain simulations based on periodic sampling of signals. Frequency domain solutions provide a faster stability prediction model while time domain solutions can provide both stability and time simulation of the process. This thesis uses frequency domain and semi-discretization methods to analyze and simulate the dynamics of multi-point threading process.

Dynamics of typical turning operations have been extensively studied by researchers. Ozlu and Budak [25] developed an analytical chatter stability model for turning and boring operations based on a simple chip discretization method. In their proposed technique, all chip elements are formed parallel to the feed direction even at the curved nose of the insert. Dynamics of multi-point threading has some similarities to parallel turning in that more than one cutting edge is engaged simultaneously. Lazoglu et al. [46] derived the dynamic model for parallel turning

when the two tools cut different surfaces of the workpiece. Budak and Ozturk [47] developed a frequency domain stability model for parallel turning on the same surface. In both [46] and [47], the two cutting tools were positioned on the opposite sides of the workpiece (180° apart), and it was shown that if the natural frequencies of the two tools are close, chip regeneration can be altered and productivity can be improved compared to single turning. Brecher et al. [48] modelled the dynamics of parallel turning as a function of the circumferential angle between the two turrets (cutting tools). They showed that in the cases where the two tools are dynamically coupled, the circumferential angle can be used to optimize the process stability.

One of the main challenges in stability prediction for turning operations such as thread turning is the accurate modelling of process damping effect. Researchers have used indentation models along with experimental calibrations to quantify the process damping contribution. Albrecht [49] considered the roundness of the cutting edge and modelled the ploughing under the clearance face of the tool. Sisson and Kegg [50] analyzed the effect of edge radius on additional damping at low speed cutting. Shaw and DeSalvo [51] studied the plastic flow under the flank face of worn tools, and suggested that process damping force in the feed direction is proportional to the volume of the indented material. Chiou and Liang [52] modelled the volume of the compressed material as a function of the ratio of the vibration velocity to cutting velocity, and calculated the process damping forces using an experimentally identified damping coefficient. Clancy and Shin [53] further extended this model and presented a three-dimensional mechanistic frequency domain chatter stability for face turning processes including the flank wear effect. Altintas et al. [54] used a fast piezo actuator to generate controlled vibrations and identified the process damping coefficients. Budak and Tunc [55] presented an identification method based on the results of stable and chatter tests, and Ahmadi and Altintas [56] proposed a technique using output-only modal analysis. Ahmadi [57] further expanded the process damping terms by considering the nonlinearities of the damping effect. Tyler et al. [58] proposed an analytical multi-degree of freedom process damping model for turning operations which considers the effect of both depth of cut and cutting velocity. They were able to predict the stability limits using only one empirical coefficient. They also concluded that identification of process damping coefficients in multi degree of freedom systems must be carried out based on the most flexible vibration mode.

While typical turning operations have been extensively studied in the past, the developed models cannot be used for multi-point thread turning processes. Not only is the chip geometry more complicated, but also the regeneration mechanism is different in that the effect of previous vibrations left by each tooth is seen by another tooth over the next spindle revolution. This thesis develops a novel model to describe the dynamics of multi-point threading with custom profiles.

2.5 Turning Thin-walled Workpieces

Turning of thin-walled workpieces imposes additional complexities due to the non-linear low-damped shell modes of the tube. Flexural vibrations in shells have been extensively studied in the past as summarized by Meirovitch [59] and Leissa [60]. Several nonlinear models have been proposed based on Love's equations for elasticity [61] and Donnell's shallow shell theory [62]. The case of cylindrical shell, in particular, involves greater complexity due to the cross coupling of different axial and circumferential modes, as studied by Evensen [63, 64] and Dowell [65]. However, analytical models become impractically complex when considering the boundary conditions and varying geometry of the workpiece in turning operations. Rahman and Ito [66] and Lai and Chang [67] showed that the frequency and direction of mode shapes can change significantly as a function of the contact length between the three-jaw clamping chuck and the workpiece. Finite element models along with experimental measurements have been the main practice in analyzing the dynamics of thin-walled workpieces.

Lai and Chang [67] studied chatter stability in turning thin-walled cylindrical shells and showed that tubes allow smaller depth of cut compared to solid bars even if they have the same moment of inertia. Dospel and Keskinen [68] derived the equations of motion for a rotating cylindrical shell subject to machining operations. Chanda et al. [69] analyzed the stability in turning cylindrical shells using semi-discretization method [38]. Chen et al. [70] employed optimization techniques to find the optimum cutting conditions in turning thin-walled workpieces. Fischer and Eberhard [71] designed an adaptronic chisel retrofitted with vibration sensors to damp out the shell vibrations in real time and achieved higher stability limits. Mehdi et al. [72, 73] presented a numerical model to simulate the turning process of thin-walled workpieces. Lorong et al. [74] considered the varying dynamics of the thin-walled workpiece during turning operation using finite element and numerical

simulation. They showed that the pattern and angle of vibration marks change along the tube axis due to varying dynamics.

There has not been any research in the past focused on the dynamics of threading of thin-walled workpieces. This thesis employs finite element and experimental modal analyses combined with the proposed dynamic models to investigate chatter stability in threading real scale oil pipes.

2.6 Summary

Chip geometry and regeneration mechanism in multi-point threading are very different than those in typical turning operations. There is currently no research available on the generalized mechanics and dynamics of thread turning. This thesis aims at filling this gap and proposes novel generalized models for calculation of chip boundaries, cutting forces, and chatter stability in multi-point threading. Application to thin-walled oil pipes is studied.

Chapter 3

Chip Geometry and Cutting Forces

3.1 Overview

This chapter proposes a semi-analytical generalized model which can systematically determine the chip geometry and cutting forces for any given multi-point threading insert and infeed settings. The chip is first discretized along the cutting edge using a systematic technique. The local chip thickness and cutting force coefficients are determined for each element, followed by the calculation of the local and total cutting forces.

Unlike most CAD/CAM software packages which calculate the tool-workpiece engagement (chip geometry) based on the intersection of the full CAD models, the proposed method integrates the kinematics of the process and the mathematical representation of the geometries. As a result, not only is the algorithm stand-alone and more accurate, but also the processing time is significantly shorter than full intersection methods.

3.2 Discrete Representation of the Cutting Edge

In the proposed methodology, all curves including the cutting edge and chip boundaries are represented by a series of discrete points laid evenly along the curve. As illustrated in Figure 3.1, two coordinate systems (CS) are used to define the setup geometry. These two CSs share the same origin, which is chosen arbitrarily at any location on the insert. The XYZ axes of the tool CS (global) are aligned with the axial, radial, and tangential directions of the workpiece, respectively. In order to

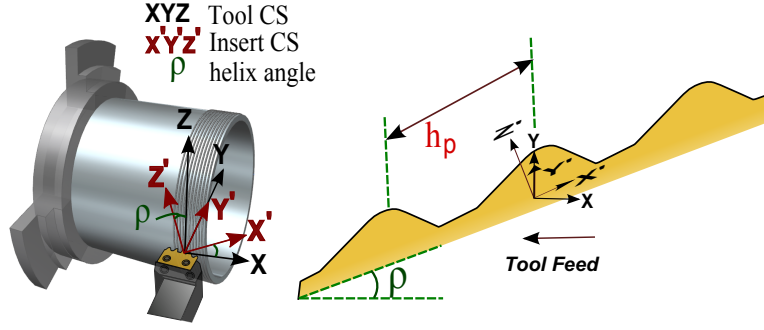


Figure 3.1: Tool and insert coordinate systems.

match the helix angle of the thread path, shims are used to rotate the insert around the radial (Y) axis equal to the helix angle

$$\rho = -\tan^{-1}(h_p/\pi d_w) \quad (3.1)$$

where h_p is the thread pitch and d_w is the workpiece diameter. The minus sign in Eq. (3.1) is to account for the negative rotation based on the defined CS (Figure 3.1). The transformation from the insert CS to the global CS is thus obtained as:

$$\mathbf{T}_{IG} = \begin{bmatrix} \cos \rho & 0 & \sin \rho \\ 0 & 1 & 0 \\ -\sin \rho & 0 & \cos \rho \end{bmatrix} \quad (3.2)$$

Consider the custom multi-point insert shown in Figure 3.2.a. Assume that the cutting edge of the insert has been designed using custom linear, circular, and spline curve segments. As the first step, the entire cutting edge is continuously interpolated by discrete points at constant intervals of du , which has been chosen as $10 \mu\text{m}$ in this thesis based on the cutting edge length (1 mm-5 mm) in common threading operations.

The geometry of the cutting edge represented in the insert CS is stored as an array of N_p number of points with ascending values of x' :

$$\mathbf{P}_{IC} = \left\{ \begin{matrix} \mathbf{P}_{x'} \\ \mathbf{P}_{y'} \\ \mathbf{P}_{z'} \end{matrix} \right\}_{IC} = \left\{ \left\{ \begin{matrix} x'_1 & x'_2 & \times & \times & x'_{N_p} \\ y'_1 & y'_2 & \times & \times & y'_{N_p} \\ z'_1 & z'_2 & \times & \times & z'_{N_p} \end{matrix} \right\} \right\}_{IC, (3 \times N_p)} \quad (3.3)$$

The edge points \mathbf{P}_{IC} are transformed from the insert CS to the global CS using the \mathbf{T}_{IG} transformation in Eq. (3.2)

$$\mathbf{P}_{GC} = \left\{ \begin{array}{c} \mathbf{P}_x \\ \mathbf{P}_y \\ \mathbf{P}_z \end{array} \right\}_{GC} = \mathbf{T}_{IG} \mathbf{P}_{IC} \quad (3.4)$$

Hereafter, all geometric parameters are represented in the global CS unless otherwise stated.

3.3 Chip Geometry for General Engagement

This section presents the general chip calculation methodology based on the assumption that each tooth cuts a fresh profile and does not intersect with the previous thread surface. In other words, both sides of the cutting tooth intersect with the outer cylinder of the workpiece surface (Figure 3.2.b). The case of partial root engagement is presented in Section 3.4 as an extension to this general procedure.

Figure 3.2.b illustrates the tool-workpiece engagement for a sample threading tooth. The chip geometry is determined as the area confined between the upper and lower bands. The upper band is formed during the current cut thus follows the shape of the current tooth. The lower band consists of several segments; the two linear edges on the left and right correspond to the workpiece surface, and the middle segment is the thread surface generated by the previous tooth. In case of single-point inserts, the middle segment is the thread profile from the previous pass. Assume the multi-point threading insert shown in Figure 3.2.a has N_t number of teeth with custom profiles. The tip of the final tooth, which performs the deepest cut, has radial coordinate of $Y_t = \max(\mathbf{P}_y)$. In order to carry out the threading operation over pass n_p , the radial penetration of the final tooth into the workpiece is incremented by infeed value of Δa relative to the previous pass. The tool travels parallel to the workpiece axis (X) at the axial feed rate of f_a . The achieved thread depth after pass n_p is calculated as:

$$a(n_p) = a(n_p - 1) + \Delta a(n_p) \quad (3.5)$$

where $a(n_p - 1)$ is the thread depth at the previous pass, and $\Delta a(n_p)$ is the current radial infeed. The outer surface of the workpiece can be represented in the current

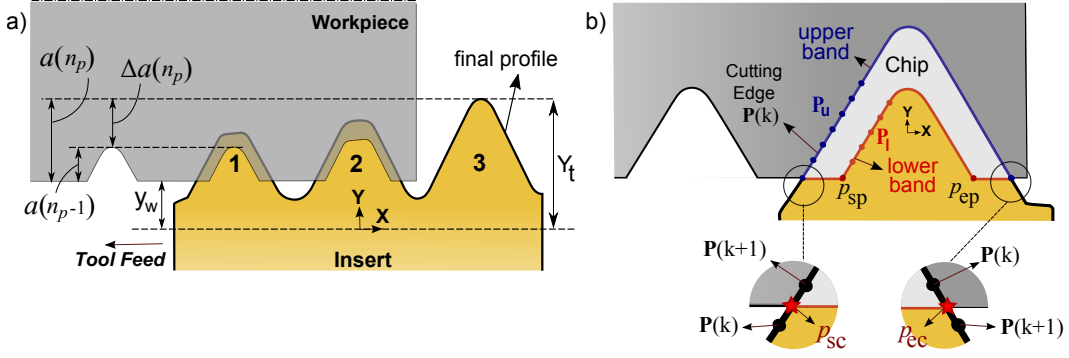


Figure 3.2: a) Definitions of radial infeed and depth of cut, b) discrete representation of the cutting edge and chip boundaries.

CS as a horizontal line (Figure 3.2.a):

$$y_w = Y_t - a(n_p) \quad (3.6)$$

In order to determine the engagement points between the cutting edge and the workpiece surface, all the points on the cutting edge, $\mathbf{P}(k)$, are swept from smallest to largest x values, and every time two consecutive points lie on the two sides of the workpiece surface, it marks an intersection point. The engagement point on the left ($^j p_{sc}$) and right ($^j p_{ec}$) of tooth j are located using the sign change in $\mathbf{P}_y - y_w$:

$$\left. \begin{array}{l} \text{if } \mathbf{P}_y(k) - y_w < 0 \\ \mathbf{P}_y(k+1) - y_w > 0 \end{array} \right\} \rightarrow \begin{array}{l} ^j p_{sc} \text{ lies between } \mathbf{P}(k) \text{ and } \mathbf{P}(k+1) \\ \text{(left engagement point)} \end{array} \quad (3.7)$$

$$\left. \begin{array}{l} \text{if } \mathbf{P}_y(k) - y_w > 0 \\ \mathbf{P}_y(k+1) - y_w < 0 \end{array} \right\} \rightarrow \begin{array}{l} ^j p_{ec} \text{ lies between } \mathbf{P}(k) \text{ and } \mathbf{P}(k+1) \\ \text{(right engagement point)} \end{array}$$

The exact location of the intersection points are obtained by interpolating between $\mathbf{P}(k)$ and $\mathbf{P}(k+1)$ and knowing that $p_{sc,y} = p_{ec,y} = y_w$. In Figure 3.2.b, p_{sp} and p_{ep} mark the intersection points over the previous cut, and are assumed to be known from similar analysis.

The discrete point representation of the upper band on tooth j over pass n_p , i.e. $^j_{n_p} \mathbf{P}_u = \left[^j_{n_p} \mathbf{P}_{ux}, ^j_{n_p} \mathbf{P}_{uy}, ^j_{n_p} \mathbf{P}_{uz} \right]^T$, is obtained by extracting part of the cutting edge which lies between the current intersection points $^j p_{sc}$ and $^j p_{ec}$ (Figure 3.2.b). Cal-

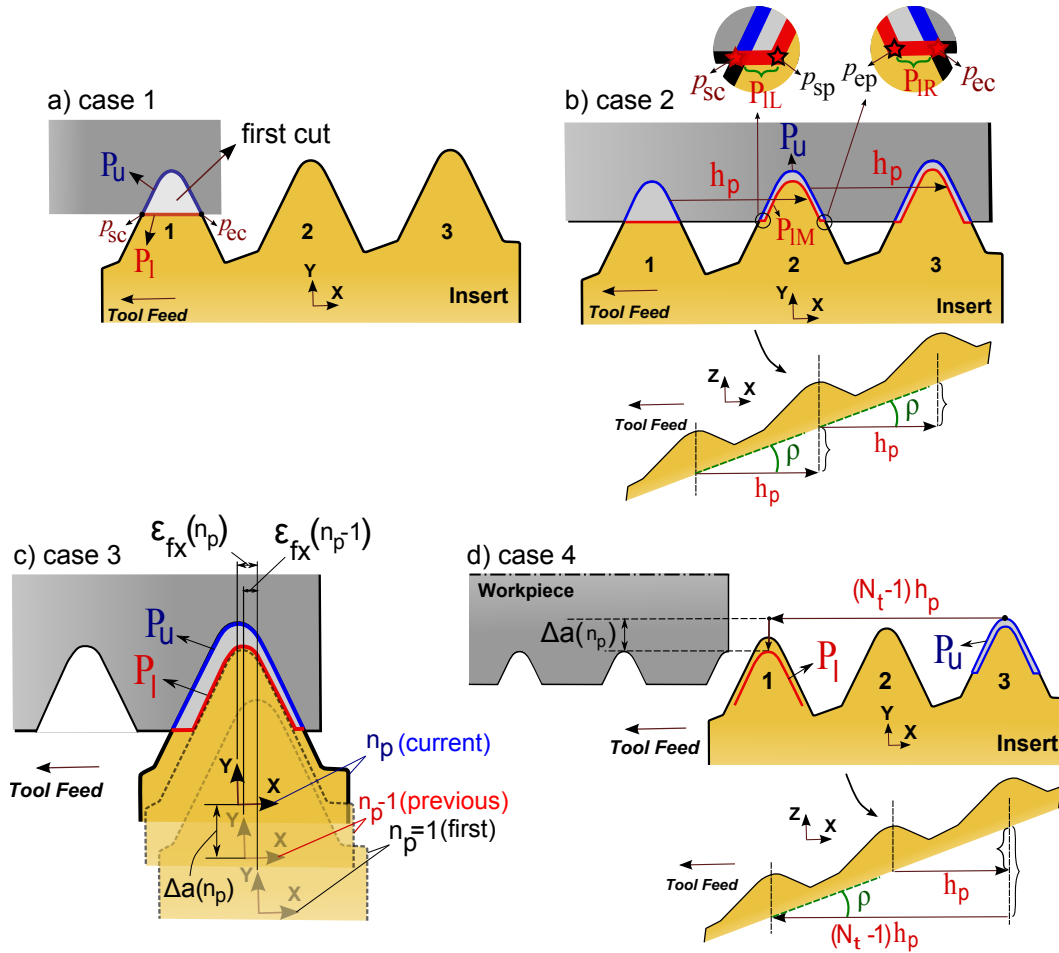


Figure 3.3: Calculation of lower band for different cases, a) first pass, first tooth, b) next teeth, c) next passes for single insert, d) next passes for multi-point insert.

calculation of the lower band ${}^j_{n_p} \mathbf{P}_l$, on the other hand, depends on the tooth number, pass number, and whether the insert is single-point or multi-point. All the possible combinations can be categorized into four cases shown in Figure 3.3. The lower band in each case is calculated as follows.

Case 1 – First Tooth ($j = 1$), First Pass ($n_p = 1$), Single- or Multi-Point Insert

As illustrated in Figure 3.3.a, the lower band of the chip in the first cut is a straight line corresponding to the workpiece surface. The discrete representation of the lower band is obtained by linear interpolation between the left (\mathbf{p}_{sc}) and right (\mathbf{p}_{ec}) intersection points using $N_l = \text{round}(|\mathbf{p}_{sc} - \mathbf{p}_{ec}| / du)$ number of points, where du is

the discretization length and chosen the same as for the upper band, i.e. $du = 10 \mu\text{m}$.

Case 2 – Next Teeth ($j > 1$), Any Pass ($n_p \geq 1$), Multi-Point Insert

As shown in Figure 3.3.b, the lower band of the chip has three segments: left (${}^j_{n_p}\mathbf{P}_{lL}$), middle (${}^j_{n_p}\mathbf{P}_{lM}$), and right (${}^j_{n_p}\mathbf{P}_{lR}$). The middle lower band is obtained by shifting the upper band of the previous tooth (${}^{j-1}_{n_p}\mathbf{P}_u$) in the X direction equal to one thread pitch h_p :

$${}^j_{n_p}\mathbf{P}_{lM} = \begin{bmatrix} {}^{j-1}_{n_p}\mathbf{P}_{ux} + h_p \\ {}^{j-1}_{n_p}\mathbf{P}_{uy} \\ {}^{j-1}_{n_p}\mathbf{P}_{uz} + h_p \tan \rho \end{bmatrix}_{j,n_p} \quad \begin{matrix} j > 1 \\ n_p \geq 1 \end{matrix} \quad (3.8)$$

Note that due to the inclination angle ρ around Y axis (Figure 3.1), the z component of the shifted upper band has been adjusted using the term $h_p \tan \rho$.

The left segment, which corresponds to the workpiece surface, is obtained by linear interpolation between \mathbf{p}_{sc} and \mathbf{p}_{sp} using $du = 10 \mu\text{m}$. The right segment is similarly interpolated between \mathbf{p}_{ep} and \mathbf{p}_{ec} , and the complete lower band on tooth j is obtained by combining all three segments, i.e ${}^j_{n_p}\mathbf{P}_l = [{}^j_{n_p}\mathbf{P}_{lL}, {}^j_{n_p}\mathbf{P}_{lM}, {}^j_{n_p}\mathbf{P}_{lR}]$.

Case 3 – Subsequent Passes ($n_p > 1$), Single-Point Insert

After finishing the first pass, the tool retracts and moves back to the starting position (tip of the workpiece). Before cutting the new pass, the radial depth and axial shift of the tool must be set based on the infeed plan (Figure 3.3.c). Since the coordinate system is attached to the insert, the middle lower band ${}^1_{n_p}\mathbf{P}_{lM}$ is obtained by transforming the upper band of the previous pass (${}^1_{n_p-1}\mathbf{P}_u$) from the previous CS to the current CS:

$${}^1_{n_p}\mathbf{P}_{lM} = \begin{bmatrix} {}^1_{n_p-1}\mathbf{P}_{ux} + [\varepsilon_{fx}(n_p) - \varepsilon_{fx}(n_p - 1)] \\ {}^1_{n_p-1}\mathbf{P}_{uy} - \Delta a(n_p) \\ {}^1_{n_p-1}\mathbf{P}_{uz} + [\varepsilon_{fx}(n_p) - \varepsilon_{fx}(n_p - 1)] \tan \rho \end{bmatrix}_{j,n_p} \quad \begin{matrix} N_t = 1 \\ n_p > 1 \end{matrix} \quad (3.9)$$

where $\Delta a(n_p) = a(n_p) - a(n_p - 1)$ is the radial infeed relative to the previous depth, and $\varepsilon_{fx}(n_p)$ is the axial shift of the tool in pass n_p measured relative to the axial start position of the tool in the first pass (Figure 3.3.c). $\varepsilon_{fx}(n_p)$ can be calculated

for different infeed plans as (see Figure 1.2.a):

$$\begin{aligned}
 \text{Radial Infeed:} & \quad \varepsilon_{fx}(n_p) = 0 & (n_p > 1) \\
 \text{Flank Infeed:} & \quad \varepsilon_{fx}(n_p) = a(n_p) \cdot \tan(\theta_{Fl}) \\
 \text{Alternate Flank Infeed:} & \quad \varepsilon_{fx}(n_p) = (-1)^{n_p} \cdot a(n_p) \cdot \tan(\theta_{Fl}) \\
 \text{Modified Flank Infeed:} & \quad \varepsilon_{fx}(n_p) = a(n_p) \cdot \tan(\theta_{Fl} - \theta_M)
 \end{aligned} \tag{3.10}$$

where θ_{Fl} is the flank angle and equals to half of the nose angle in V-profile. $\theta_M \sim 3^\circ\text{-}5^\circ$ is the deviation angle in Modified Flank (Figure 1.2.a). In Eq. (3.9), the term $[\varepsilon_{fx}(n_p) - \varepsilon_{fx}(n_p - 1)]$ calculates the axial shift (x component) of the tool in the new pass relative to the previous pass, and the term $[\varepsilon_{fx}(n_p) - \varepsilon_{fx}(n_p - 1)] \tan \rho$ adjusts the z component due to the inclination (shim) angle of the insert.

Similar to Case 2, the left and right linear segments are interpolated between the current and previous intersection points, and the complete lower band is obtained by combining the three segments.

Case 4 – First Tooth ($j = 1$), Subsequent Passes ($n_p > 1$), Multi-Point Insert

In this case, the lower band on the first tooth is formed by the the final tooth ($j = N_t$) during the previous pass. As illustrated in Figure 3.3.d, the last upper band (${}_{n_p-1}^{j=N_t} \mathbf{P}u = [{}_{n_p-1}^{j=N_t} \mathbf{P}u_x, {}_{n_p-1}^{j=N_t} \mathbf{P}u_y, {}_{n_p-1}^{j=N_t} \mathbf{P}u_z]^T$) is shifted onto the first tooth and transformed from the previous CS to the new CS:

$${}_{n_p}^{j=1} \mathbf{P}_{IM} = \begin{bmatrix} {}_{n_p-1}^{j=N_t} \mathbf{P}u_x - (N_t - 1) h_p + [\varepsilon_{fx}(n_p) - \varepsilon_{fx}(n_p - 1)] \\ {}_{n_p-1}^{j=N_t} \mathbf{P}u_y - \Delta a(n_p) \\ {}_{n_p-1}^{j=N_t} \mathbf{P}u_z - (N_t - 1) h_p \tan \rho + [\varepsilon_{fx}(n_p) - \varepsilon_{fx}(n_p - 1)] \tan \rho \end{bmatrix}_{j,n_p} \tag{3.11}$$

$j = 1$
 $N_t > 1$
 $n_p > 1$

where N_t is the total number of teeth engaged in the cut during the previous pass. The term $(N_t - 1) h_p$ shifts the previous upper band in the axial direction onto the first tooth, and $(N_t - 1) h_p \tan \rho$ adjusts the z component due to the shim angle. The terms $\Delta a(n_p)$ and $[\varepsilon_{fx}(n_p) - \varepsilon_{fx}(n_p - 1)]$ adjust the radial and axial shift of the current CS relative to the previous CS, and $[\varepsilon_{fx}(n_p) - \varepsilon_{fx}(n_p - 1)] \tan \rho$ corrects for the insert's inclination angle.

Similar to Cases 2 and 3, the linear segments on the left and right are interpolated between the current and previous intersection points, and the complete lower

band is obtained by combining the three segments.

3.4 Chip Geometry for Partial Root Engagement

As illustrated in Figure 3.4, multi-point inserts are commonly designed such that few teeth perform rough cutting of the root, and the following teeth finish the thread profile. Partial engagement is especially common for buttress threads as the side edges are nearly parallel to the infeed (radial) direction; cutting the sides with all teeth may lead to impractically small chip load thus severe ploughing and poor surface finish.

In the case of partial root engagement, at least one side of the tooth cuts inside the previous thread profile (Figure 3.4.a). Partial engagement on each tooth can be detected using the following conditions:

$$\left. \begin{array}{l} 1) \mathbf{p}_{sc,x} > \mathbf{p}_{sp,x} \quad (\text{left}) \\ \text{and/or} \\ 2) \mathbf{p}_{ec,x} < \mathbf{p}_{ep,x} \quad (\text{right}) \end{array} \right\} \rightarrow \text{Partial Engagement} \quad (3.12)$$

where \mathbf{p}_{sc} , \mathbf{p}_{ec} , \mathbf{p}_{sp} , and \mathbf{p}_{ep} are the intersection points calculated based on the assumptions of general engagement (Eq. (3.7)). If the conditions in Eq. (3.12) hold, \mathbf{p}_{sc} and/or \mathbf{p}_{ec} must be re-evaluated to find the correct engagement points between the tooth and workpiece.

3.4.1 Re-evaluation of The Left Engagement Point (\mathbf{p}_{sc})

The following steps must be taken to find the correct left engagement point (convexity of the profile is assumed):

Step 1. Calculate the upper and lower bands of the chip assuming complete engagement as explained in Section 3.3.

Step 2. Find the first and second far left points (smallest x coordinates) on the upper band, marked as $\mathbf{p}_{s,u1}$ and $\mathbf{p}_{s,u2}$ in Figure 3.4.c.

Step 3. Construct the equation of the line connecting $\mathbf{p}_{s,u1}$ and $\mathbf{p}_{s,u2}$.

Step 4. Find the point $\mathbf{p}_{s,l}$ on the lower band which has smallest x coordinate and satisfies $\mathbf{p}_{s,l}(x) > \mathbf{p}_{s,u1}(x)$.

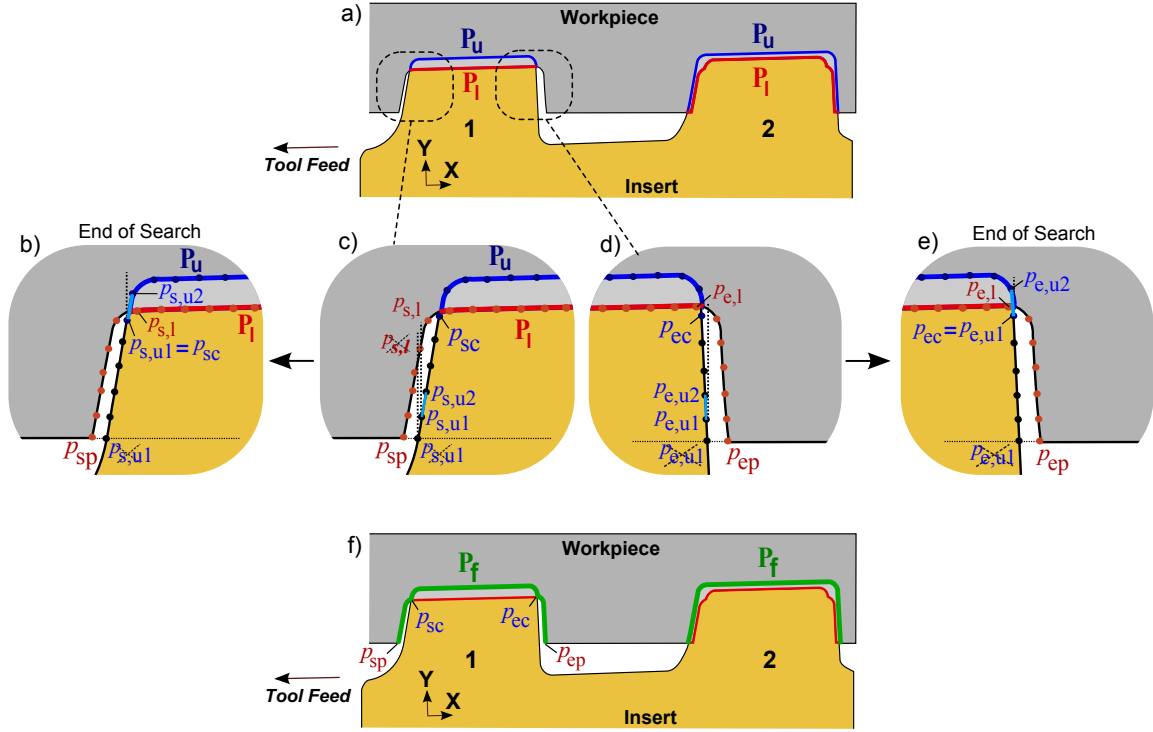


Figure 3.4: Determining the chip boundaries and thread profile in the case of partial root engagement.

Step 5. Project $p_{s,l}$ in the Y direction onto the line $(\overline{p_{s,u1}, p_{s,u2}})$ from Step 3. Check if $p_{s,l}$ is located under this line segment (or its extension) and also between $p_{s,u1}$ and $p_{s,u2}$ in the Y direction, i.e.

$$\begin{cases} p_{s,l}(y) < \frac{p_{s,u2}(y) - p_{s,u1}(y)}{p_{s,u2}(x) - p_{s,u1}(x)} (x - p_{s,u1}(x)) + p_{s,u1}(y) \\ \text{and} \\ p_{s,u1}(y) < p_{s,l}(y) < p_{s,u2}(y) \end{cases} \quad (3.13)$$

If both conditions in Eq. (3.13) hold, $p_{sc} = p_{s,u1}$ is chosen as the correct left intersection point, and the search is completed. Otherwise, $p_{s,u1}$ is deleted from the upper band, and $p_{s,u2}$ becomes the new $p_{s,u1}$. The search restarts from Step 2 with the new $p_{s,u1}$ and continues until the correct intersection is found.

3.4.2 Re-evaluation of The Right Engagement Point (\mathbf{p}_{ec})

The procedure follows similar steps presented above but the conditions must be adjusted for the right side edge. As marked in Figure 3.4.d, assume $\mathbf{p}_{e,u1}$ and $\mathbf{p}_{e,u2}$ are the first and second far right points (largest x coordinates) on the upper band. $\mathbf{p}_{e,l}$ is the point on the lower band with the largest x coordinate which satisfies $\mathbf{p}_{e,l}(x) < \mathbf{p}_{e,u1}(x)$. $\mathbf{p}_{e,l}$ is projected in the Y direction onto the line connecting $\mathbf{p}_{e,u1}$ and $\mathbf{p}_{e,u2}$. If

$$\left\{ \begin{array}{l} \mathbf{p}_{e,l}(y) < \frac{\mathbf{p}_{e,u2}(y) - \mathbf{p}_{e,u1}(y)}{\mathbf{p}_{e,u2}(x) - \mathbf{p}_{e,u1}(x)} (x - \mathbf{p}_{e,u1}(x)) + \mathbf{p}_{e,u1}(y) \\ \text{and} \\ \mathbf{p}_{e,u1}(y) < \mathbf{p}_{e,l}(y) < \mathbf{p}_{e,u2}(y) \end{array} \right. \quad (3.14)$$

the search is completed and $\mathbf{p}_{ec} = \mathbf{p}_{e,u1}$ is chosen as the correct right intersection point (Figure 3.4.e); otherwise, $\mathbf{p}_{e,u1}$ is deleted and the search restarts with the new points.

3.4.3 Updating the Upper and Lower Bands

Once the correct intersection points are found using the above procedure, part of the previously calculated upper band (based on Section 3.3) which lies between the updated \mathbf{p}_{sc} and \mathbf{p}_{ec} is extracted as the tooth-workpiece engagement (upper band). Calculation of the lower band requires knowing the previous thread profile; as shown in Figure 3.4.f, in case of partial engagement, the resulting profile consists of several segments corresponding to the current and one or more of the preceding cuts. The following section presents a general methodology to obtain the thread profile.

3.4.4 Thread Profile After Each Cut

For each of the four cases defined in Section 3.3 (Figure 3.3), the previous thread profile is shifted from the previous tooth (or pass) onto the current tooth. The new profile, ${}^j_{n_p} \mathbf{P}_f$, follows the shape of the current tooth in the engaged sections (upper band) and keeps the previous profile for the uncut parts (Figure 3.4.f). Calculation of the thread profile for each case is presented below.

Case 1. – First cut ($j = 1, n_p = 1$)

The thread profile in this case is the same as the upper band of the first tooth, i.e.

$$\left(\begin{matrix} j=1 \\ n_p=1 \end{matrix} \mathbf{P}_f \right) = \left(\begin{matrix} j=1 \\ n_p=1 \end{matrix} \mathbf{P}_u \right) \quad (3.15)$$

Case 2. – Next teeth ($j > 1$)

The thread profile is shifted from the previous tooth to the current tooth (see Figure 3.3.b):

$$\left\{ \begin{array}{l} \begin{matrix} j \\ n_p \end{matrix} \mathbf{P}_f = \begin{matrix} j-1 \\ n_p \end{matrix} \mathbf{P}_f + \begin{bmatrix} h_p \\ 0 \\ h_p \tan \rho \end{bmatrix} \\ \begin{matrix} j \\ n_p \end{matrix} \mathbf{P}_f = \begin{matrix} j \\ n_p \end{matrix} \mathbf{P}_u \end{array} \right. \begin{array}{l} \xleftarrow{C1} \left\{ \begin{array}{l} \forall k : \mathbf{p}_{sp}(x) < \left(\begin{matrix} j-1 \\ n_p \end{matrix} \mathbf{P}_{f,x}(k) \right) < \mathbf{p}_{sc}(x) \\ \text{or } \mathbf{p}_{ec}(x) < \left(\begin{matrix} j-1 \\ n_p \end{matrix} \mathbf{P}_{f,x}(k) \right) < \mathbf{p}_{ep}(x) \end{array} \right. \\ \xleftarrow{C2} \forall k : \mathbf{p}_{sc}(x) < \left(\begin{matrix} j-1 \\ n_p \end{matrix} \mathbf{P}_{f,x}(k) \right) < \mathbf{p}_{ec}(x) \end{array} \right. \quad (3.16)$$

where h_p is the thread pitch and ρ is the shim angle. $C1$ is the condition for the uncut segments, and $C2$ corresponds to the engaged segments (Figure 3.4.f).

Case 3. – Next passes ($n_p > 1$), single-point insert

The thread profile from the previous pass is transformed from the previous CS to the current CS based on the radial and axial infeed settings (see Figure 3.3.c):

$$\left\{ \begin{array}{l} \begin{matrix} 1 \\ n_p \end{matrix} \mathbf{P}_f = \begin{matrix} 1 \\ n_p-1 \end{matrix} \mathbf{P}_f + \begin{bmatrix} \varepsilon_{fx}(n_p) - \varepsilon_{fx}(n_p - 1) \\ -\Delta a(n_p) \\ [\varepsilon_{fx}(n_p) - \varepsilon_{fx}(n_p - 1)] \tan \rho \end{bmatrix} \\ \begin{matrix} 1 \\ n_p \end{matrix} \mathbf{P}_f = \begin{matrix} 1 \\ n_p \end{matrix} \mathbf{P}_u \end{array} \right. \begin{array}{l} \xleftarrow{C1} \\ \xleftarrow{C2} \end{array} \quad (3.17)$$

where $C1$ and $C2$ are the conditions defined in Eq. (3.16), and Δa and ε_{fx} are the radial and axial infeed settings defined in Section 3.3.

Case 4. – Next passes ($n_p > 1$), first tooth ($j = 1$), multi-point insert

In this case, the thread profile from the previous pass is shifted from the final tooth onto the first tooth and transformed from the previous CS to the current

CS (see Figure 3.3.d):

$$\left\{ \begin{array}{l} {}^1_{n_p} \mathbf{P}_f = {}^{N_t}_{n_p-1} \mathbf{P}_f + \begin{bmatrix} -(N_t - 1)h_p + [\varepsilon_{fx}(n_p) - \varepsilon_{fx}(n_p - 1)] \\ -\Delta a(n_p) \\ (-(N_t - 1)h_p + [\varepsilon_{fx}(n_p) - \varepsilon_{fx}(n_p - 1)]) \tan \rho \end{bmatrix} \leftarrow C1 \\ {}^1_{n_p} \mathbf{P}_f = {}^1_{n_p} \mathbf{P}_u \leftarrow C2 \end{array} \right. \quad (3.18)$$

where N_t is the total number of teeth engaged in the cut during the previous pass, and $C1$ and $C2$ are the conditions defined in Eq. (3.16).

3.4.5 Lower Band in Partial Engagement

In the case of partial engagement, the lower band follows part of the previous thread profile engaged in the current cut (see Figure 3.4.a,f), i.e.

$${}^j_{n_p} \mathbf{P}_l = \mathbf{P}_{fs} \leftarrow \forall k : \mathbf{p}_{sc}(x) < \mathbf{P}_{fs,x}(k) < \mathbf{p}_{ec}(x) \quad (3.19)$$

where \mathbf{P}_{fs} is the shifted previous profile calculated in the first equation (without condition) in Eqs. (3.16), (3.17), and (3.18) corresponding to each case.

It should be noted that the chip evaluation procedure presented in this section can be readily used for the cases where one side of the insert is intersecting with the workpiece surface and the other side is cutting inside the thread profile.

3.5 Systematic Chip Discretization

Figure 3.5.a illustrates the chip flow lines in cutting a buttress profile. It can be seen that around the corners where two edges meet, the flow lines overlap. This is due to chip interference and happens when the material removed by different edges compress into each other. Figure 3.5.b shows a sample case of stress distribution (using AdvantEdge) in cutting a V-profile thread. It can be seen that there is higher stress concentration at the nose due to chip interference.

Remark. The chip flow angle at the corners is also affected by the chip interference. However, since the cutting forces are generated very close to the cutting zone, the change in the chip flow angle due to interference causes less than 1% error in the force modelling, and thus has been ignored in this thesis.

The following sections present a systematic discretization method which forms

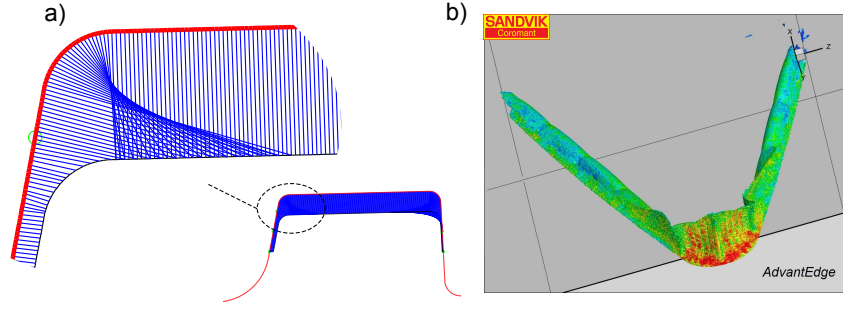


Figure 3.5: a) Overlapping of chip flow lines due to chip interference, b) stress distribution in cutting V60° thread.

the chip elements along the cutting edge taking into account the chip flow direction and chip interference. The proposed method draws the discretization lines by running a search algorithm which pairs proper points on the upper and lower bands. Since the procedure is carried out for each tooth individually, the superscript j (tooth number) and subscript n_p (pass number) are dropped in the following derivations for simplicity.

As illustrated in Figure 3.6, at every point $\mathbf{P}_u(k)$ on the upper band, where $k = 1, 2, \dots, N_u$, the local vector $\mathbf{L}_u(k)$ tangent to the upper band is calculated as:

$$\mathbf{L}_u(k) = \mathbf{P}_u(k+1) - \mathbf{P}_u(k) \quad (3.20)$$

Similarly, at every point $\mathbf{P}_l(i)$ on the lower band, where $i = 1, 2, \dots, N_l$, the local tangent vector is $\mathbf{L}_l(i) = \mathbf{P}_l(i+1) - \mathbf{P}_l(i)$. For a fixed point $\mathbf{P}_u(k)$ on the upper band and for any point $\mathbf{P}_l(i)$ on the lower band, vector $\tilde{\mathbf{h}}(k, i)$ which connects $\mathbf{P}_u(k)$ to $\mathbf{P}_l(i)$ is calculated as (Figure 3.6):

$$\tilde{\mathbf{h}}(k, i) = \mathbf{P}_l(i) - \mathbf{P}_u(k) \quad (3.21)$$

Scalar projection of $\tilde{\mathbf{h}}(k, i)$ on the upper band is obtained using inner product as

$$S_u(k, i) = \bar{\mathbf{L}}_u(k) \cdot \tilde{\mathbf{h}}(k, i) \quad (3.22)$$

where $\bar{\mathbf{L}}_u(k)$ is the unit average tangent vector at $\mathbf{P}_u(k)$:

$$\bar{\mathbf{L}}_u(k) = \frac{\mathbf{L}_u(k-1) + \mathbf{L}_u(k)}{|\mathbf{L}_u(k-1) + \mathbf{L}_u(k)|} = \frac{\mathbf{P}_u(k+1) - \mathbf{P}_u(k-1)}{|\mathbf{P}_u(k+1) - \mathbf{P}_u(k-1)|} \quad (3.23)$$

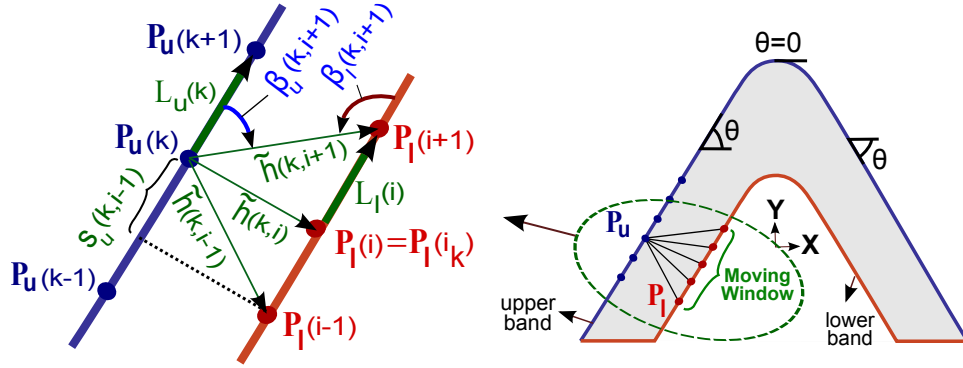


Figure 3.6: Search algorithm and forming the chip discretization lines.

The unit average vector $\bar{L}_l(i)$ tangent to the lower band at $\mathbf{P}_l(i)$ is calculated similar to Eq. (3.23). Projection of $\tilde{\mathbf{h}}(k,i)$ on the lower band is obtained by inner product as $S_l(k,i) = \bar{L}_l(i) \cdot \tilde{\mathbf{h}}(k,i)$. The angles β_u (on the upper band) and β_l (on the lower band) between the discretization line $\tilde{\mathbf{h}}(k,i)$ and the positive direction of $\bar{L}_u(k)$ and $\bar{L}_l(i)$, respectively, are calculated as:

$$\beta_w(k,i) = \cos^{-1} \left(\frac{S_w(k,i)}{|\tilde{\mathbf{h}}(k,i)|} \right), \quad w = u, l \quad \rightarrow \quad \begin{cases} -180^\circ < \beta_u < 0 \\ 0 < \beta_l < 180^\circ \end{cases} \quad (3.24)$$

where β_u lies in the third or fourth quadrants of the trigonometric circle, and β_l lies in the first or second quadrants. In order to have the discretization lines normal to both the cutting edge and lower band, β_u and β_l must be ideally -90° and 90° , respectively. In this case,

$$\beta_s(k,i) = \beta_u(k,i) + \beta_l(k,i) = 0 \quad (3.25)$$

However, due to the varying curvature of the edge profile as well as chip interference in the corners, satisfying the condition in Eq. (3.25) may not be possible. The value of $|\beta_s(k,i)|$ quantifies the deviation of the discretization line from orthogonality, and thus can be used as a pairing criterion; every point $\mathbf{P}_u(k)$ on the upper band is paired with a point $\mathbf{P}_l(i)$ on the lower band which results in the smallest absolute value of $\beta_s(k,i)$.

In order to improve the reliability of the discretization scheme, additional constraints are imposed on the angles β_u and β_l ; the discretization lines are allowed to have maximum deviation of 30° from orthogonality to the upper band and 60° from

orthogonality to the lower band. The pairing criteria can therefore be summarized as:

$$\mathbf{P}_u(k) \rightarrow \mathbf{P}_l(i) : \begin{cases} \min\{|\beta_u(k,i) + \beta_l(k,i)|\} \\ |\beta_u(k,i) + 90| < 30^\circ \\ |\beta_l(k,i) - 90| < 60^\circ \end{cases} \quad (3.26)$$

Since for every point $\mathbf{P}_u(k)$ on the upper band, the proper point $\mathbf{P}_l(i)$ on the lower band is expected to be found at a close vicinity of $\mathbf{P}_u(k)$, the search algorithm is run only over a moving window as illustrated in Figure 3.6. This window extends 5%¹ of the length of the lower band around $\mathbf{P}_l(i_m)$, where i_m is the index of the point which divides the lower band at the same ratio that $\mathbf{P}_u(k)$ divides the upper band, i.e.:

$$\frac{i_m}{N_l} = \frac{k}{N_u} \rightarrow i_m = \frac{N_l}{N_u}k \quad (3.27)$$

where N_u and N_l are the total number of points on the upper and lower bands, respectively. In order to avoid intersection of the discretization lines, the search algorithm skips the points of the lower band which lie before the last paired point $\mathbf{P}_l(i_p)$. The moving window can therefore be described as:

$$\mathbf{P}_u(k) \rightarrow \mathbf{P}_l(i) : \quad \max(i_p, i_m - 0.05N_l) < i < i_m + 0.05N_l \quad (3.28)$$

where i_p is the index of the last paired point on the lower band, and i_m is defined in Eq. (3.27).

The procedure presented above is run for each point $\mathbf{P}_u(k)$ on the upper band, and connects it to a proper point on the lower band. As a result, the number of discretization lines (and thus chip elements) is equal to the number of points on the upper band. Depending on the geometry of the chip and curvature of the thread profile, several discretization lines might be connected to the same point on the lower band, and on the other hand, some points of the lower band might not be connected to any discretization line.

Figure 3.7 shows sample results for the multi-point V-profile and buttress inserts with the discretization length of $du = 10\mu\text{m}$. It can be seen that the chip has been uniformly discretized even at the highly curved segments where chip interference is significant. For verification, the total area calculated as the summation of individual

¹Due to the convex shape of thread profiles, the proper discretization line always lie within the 5% moving window. Hence, further extension of the window does not improve the accuracy.

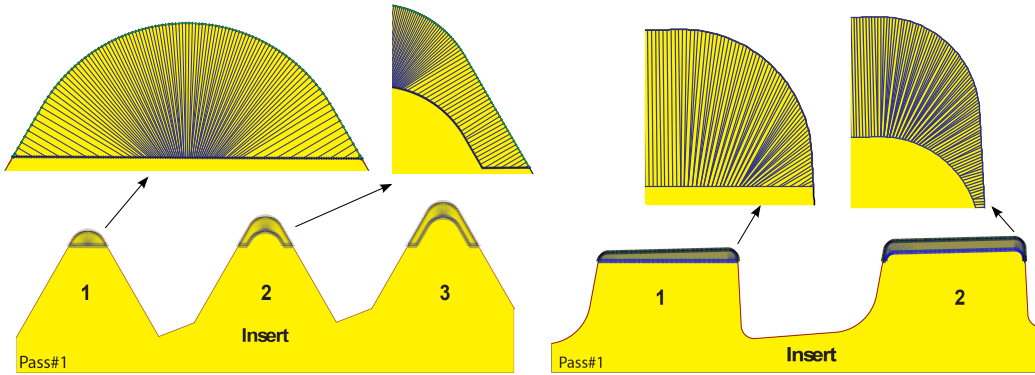


Figure 3.7: Sample chip discretization results ($du = 10\ \mu\text{m}$).

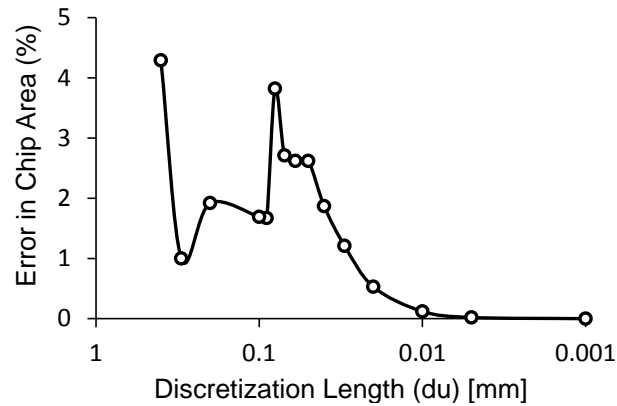


Figure 3.8: Sensitivity of chip modelling to the discretization length (du) (Insert: three-point V-profile, chip thickness per tooth: $0.3\ \text{mm}$).

chip elements (Eq. (3.42)) has been compared against the CAD models in NX (by intersecting the cross sections of the insert and the workpiece). In all cases, the error is below 0.5%. Figure 3.8 shows the sensitivity of the calculated chip area to the discretization length (du) for the three-point V-profile insert shown in Figure 3.7. It can be seen that reducing the discretization length below $10\ \mu\text{m}$ does not affect the accuracy significantly, thus is not practical.

3.6 Cutting Force Calculation

This section presents a systemic methodology to calculate the local and total cutting forces.

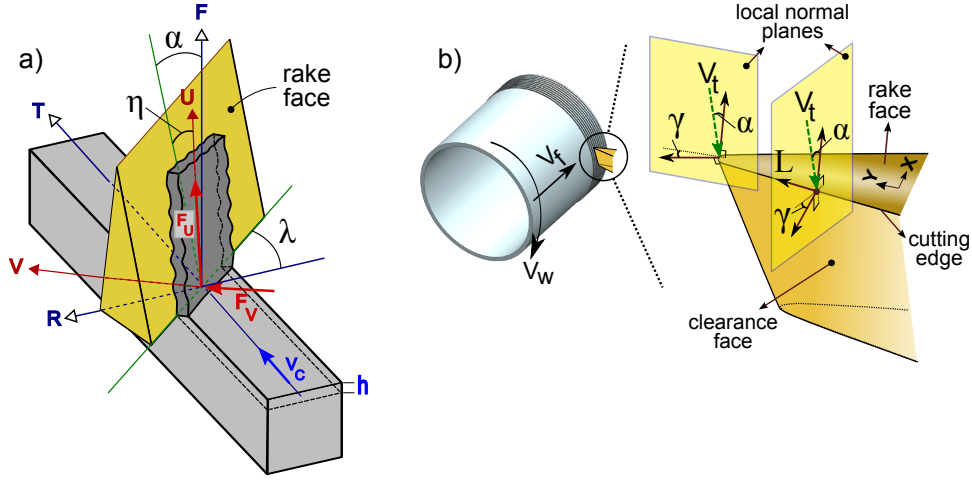


Figure 3.9: a) General definition of oblique cutting parameters, b) local oblique vectors.

3.6.1 Local Oblique Cutting Angles

Mechanics of oblique cutting is illustrated in Figure 3.9.a. The rake angle α is defined as the angle between the rake face and the vector normal to the cut surface. Inclination λ is the relative angle between the cutting edge and the vector normal to the cutting velocity in the plane of cut. Clearance γ is the angle between the clearance face and the cut plane. η is the chip flow angle, which is assumed to be the same as inclination, i.e. $\eta = \lambda$, as suggested by Stabler [75].

As illustrated in Figure 3.9.b, the cutting velocity in thread turning consists of two components corresponding to the rotation of the workpiece (V_w) and axial feedrate of the cutting tool (V_f):

$$\mathbf{V}_t = \mathbf{V}_w + \mathbf{V}_f \quad \leftarrow \begin{cases} \mathbf{V}_w = [0, 0, -(\pi d_w n)/60]^T & \text{(circumferential)} \\ \mathbf{V}_f = [h_p \cdot n/60, 0, 0]^T & \text{(axial)} \end{cases} \quad (3.29)$$

where d_w is the diameter of the workpiece, n [rev/min] is the spindle speed, and h_p is the thread pitch. In most regular turning operations, the axial feed (V_f) is relatively small and can be ignored compared to the circumferential velocity. In thread turning, however, the tool has to travel axially one pitch over each spindle revolution; depending on the workpiece diameter, pitch of the thread, and the spindle speed, the axial feedrate can be considerable in thread turning. Both components are considered in this thesis for generality.

As illustrated in Figure 3.9.b, the angle between the velocity vector \mathbf{V}_t and the cutting planes varies along the threading tooth. In order to calculate the effective oblique angles systematically, three orthogonal unit vectors have been defined locally at each point along the cutting edge: vector $\bar{\mathbf{L}}$ tangent to the cutting edge, vector $\bar{\boldsymbol{\alpha}}$ normal to rake face, and vector $\bar{\boldsymbol{\gamma}}$ normal to the clearance face. At each point $\mathbf{P}_u(k)$ on the cutting edge (Figure 3.6), the unit tangent vector $\bar{\mathbf{L}}(k)$ is obtained as (repeated from Eq. (3.23)):

$$\bar{\mathbf{L}}(k) = \frac{\mathbf{P}_u(k+1) - \mathbf{P}_u(k-1)}{|\mathbf{P}_u(k+1) - \mathbf{P}_u(k-1)|} \quad (3.30)$$

The rake and clearance unit vectors are calculated from their projections on the XY plane and Z axis:

$$\bar{\mathbf{\Gamma}}(k) = \mathbf{T}_{IG} \cdot \bar{\mathbf{\Gamma}}_{IC}(k) = \mathbf{T}_{IG} \cdot \frac{\bar{\mathbf{\Gamma}}_{xy}(k) + \bar{\mathbf{\Gamma}}_z(k)}{|\bar{\mathbf{\Gamma}}_{xy}(k) + \bar{\mathbf{\Gamma}}_z(k)|}, \quad \bar{\mathbf{\Gamma}} = \bar{\boldsymbol{\alpha}}, \bar{\boldsymbol{\gamma}} \quad (3.31)$$

where

$$\begin{cases} \bar{\boldsymbol{\alpha}}_{xy}(k) = (\sin \alpha_0) \left[\cos \theta(k), -\sin \theta(k), 0 \right]^T \\ \bar{\boldsymbol{\alpha}}_z(k) = \left[0, 0, (\cos \alpha_0) \right]^T \end{cases} \quad (3.32)$$

$$\begin{cases} \bar{\boldsymbol{\gamma}}_{xy}(k) = (\cos \gamma_0) \left[-\cos \theta(k), \sin \theta(k), 0 \right]^T \\ \bar{\boldsymbol{\gamma}}_z(k) = \left[0 \quad 0 \quad (-\sin \gamma_0) \right]^T \end{cases} \quad (3.33)$$

where α_0 and γ_0 are the nominal rake and clearance angles of the insert, and \mathbf{T}_{IG} is the insert-to-global coordinate transformation matrix defined in Eq. (3.2). $\theta(k)$ is the local approach angle defined in Figure 3.6.b and calculated as:

$$\theta(k) = \tan^{-1} \left(\frac{\mathbf{P}_{u,y}(k+1) - \mathbf{P}_{u,y}(k)}{\mathbf{P}_{u,x}(k+1) - \mathbf{P}_{u,x}(k)} \right) \quad (3.34)$$

considering the four quadrants of the trigonometric circle. Based on the geometric definitions in Figure 3.9.a, the effective local oblique angles at each point $\mathbf{P}_u(k)$ along the threading tooth are calculated as:

$$\text{rake angle: } \alpha(k) = -\frac{\pi}{2} + \cos^{-1} \left(\bar{\boldsymbol{\alpha}}(k) \cdot \left(\bar{\mathbf{L}}(k) \times \frac{\mathbf{V}_t}{|\mathbf{V}_t|} \right) \right) \quad (3.35)$$

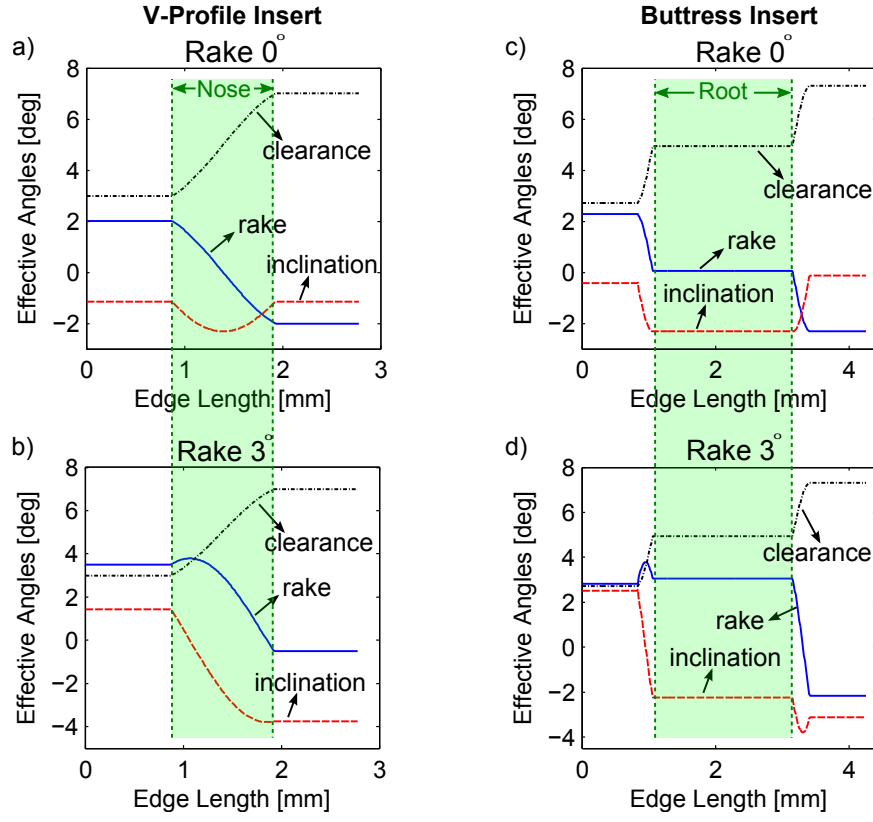


Figure 3.10: Sample effective oblique angles for V-profile and buttress inserts with rake angles of $\alpha_0 = 0^\circ$ and $\alpha_0 = 3^\circ$ (workpiece diameter: 40 mm, thread pitch: 5 mm, clearance angle: 5°)

$$\text{inclination angle:} \quad \lambda(k) = -\frac{\pi}{2} + \cos^{-1} \left(\bar{\mathbf{L}}(k) \cdot \frac{\mathbf{V}_t}{|\mathbf{V}_t|} \right) \quad (3.36)$$

$$\text{clearance angle:} \quad \gamma(k) = \frac{\pi}{2} - \cos^{-1} \left(\bar{\boldsymbol{\gamma}}(k) \cdot \frac{\mathbf{V}_t}{|\mathbf{V}_t|} \right) \quad (3.37)$$

where (\cdot) and (\times) denote inner and cross products, respectively.

Figure 3.10 shows the calculated oblique angles along sample V-profile and buttress inserts (dimensions given in Figure 1.1.c). The diameter of the workpiece and the thread pitch are assumed to be 40 mm and 5 mm, respectively, and the inserts have nominal clearance angle of 5° . The oblique angles have been calculated for two values of rake angle: $\alpha_0 = 0^\circ$ and $\alpha_0 = 3^\circ$. It can be seen that the effective angles vary considerably along the cutting edge.

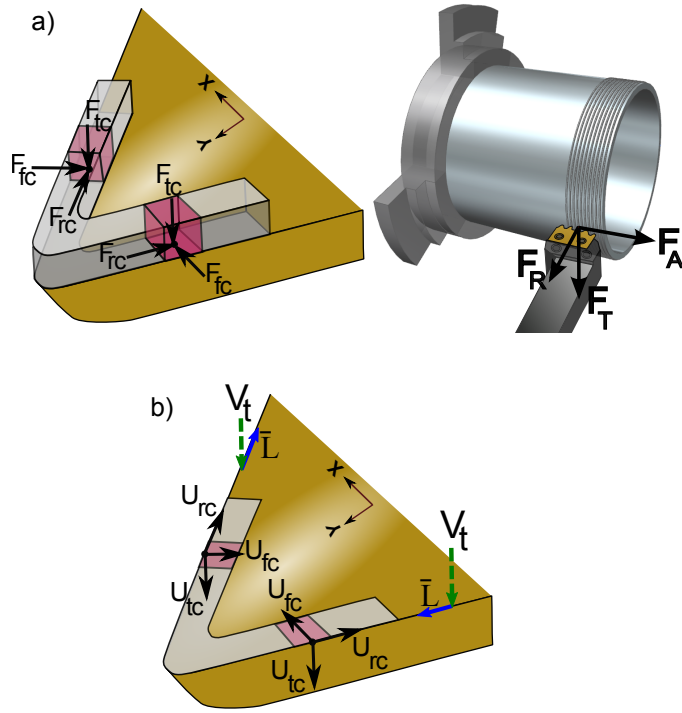


Figure 3.11: a) Local and total forces exerted on the tool, b) unit direction vectors of the local cutting forces.

3.6.2 Local Cutting Force Coefficients

Figure 3.11.a illustrates the local tangential, feed, and radial cutting forces exerted on the tool at two locations along the cutting edge. For each chip element k , the unit vectors defining the direction of the local forces can be calculated as (Figure 3.11.b):

$$U_{tc}(k) = \frac{V_t}{|V_t|} \quad (3.38)$$

$$U_{fc}(k) = \frac{V_t \times \bar{L}(k)}{|V_t \times \bar{L}(k)|} \quad (3.39)$$

$$U_{rc}(k) = (U_{tc}(k) \times U_{fc}(k)) \cdot \text{sgn}(U_{fc,x}(k)) \quad (3.40)$$

where V_t and $\bar{L}(k)$ are the velocity and local edge vectors defined in Eqs. (3.29) and (3.30), respectively. The magnitudes of the local force components are:

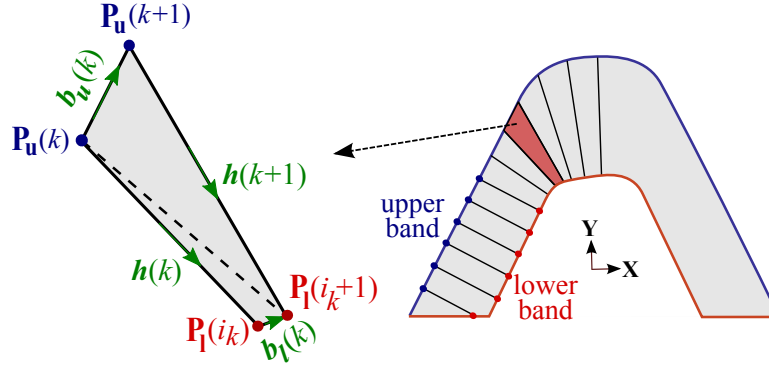


Figure 3.12: Edge vectors defining the chip elements.

$$\begin{Bmatrix} F_{tc}(k) \\ F_{fc}(k) \\ F_{rc}(k) \end{Bmatrix} = \begin{bmatrix} K_{tc}(k) \\ K_{fc}(k) \\ K_{rc}(k) \end{bmatrix} \cdot A_c(k) \quad (3.41)$$

where $A_c(k)$ is the area of the chip element k , and K_{tc} , K_{fc} , and K_{rc} are the local cutting force coefficients. As illustrated in Figure 3.12, the area of the chip element k can be calculated using the cross product of the element's edge vectors:

$$A_c(k) = \frac{1}{2} \{ |\mathbf{h}(k) \times \mathbf{b}_l(k)| + |\mathbf{h}(k+1) \times \mathbf{b}_u(k)| \} \quad (3.42)$$

where $\mathbf{h}(k)$ and $\mathbf{h}(k+1)$ are the thickness vectors, and $\mathbf{b}_l(k)$ and $\mathbf{b}_u(k)$ are the width vectors on the upper and lower bands, respectively. These vectors are calculated as (Figure 3.12):

$$\mathbf{h}(k) = \mathbf{P}_l(i_k) - \mathbf{P}_u(k) \quad (3.43)$$

$$\mathbf{h}(k+1) = \mathbf{P}_l(i_{k+1}) - \mathbf{P}_u(k+1) \quad (3.44)$$

$$\mathbf{b}_u(k) = \mathbf{P}_u(k+1) - \mathbf{P}_u(k) \quad (3.45)$$

$$\mathbf{b}_l(k) = \mathbf{P}_l(i_{k+1}) - \mathbf{P}_l(i_k) \quad (3.46)$$

where i_k is the index of the point (on the lower band) paired with the point $\mathbf{P}_u(k)$ of the upper band (see Section 3.5). As marked in Figure 3.12, the cross products in Eq. (3.42) give the area of the lower and upper triangles, respectively. Using this approach, the area is calculated accurately even in the case of distorted or three edge elements.

For each chip element k , the local cutting force coefficients in Eq. (3.41) are

obtained as:

$$\begin{Bmatrix} K_{tc}(k) \\ K_{fc}(k) \\ K_{rc}(k) \end{Bmatrix} = \mathbf{T}_{ob}(k) \begin{bmatrix} K_u(k) \\ K_v(k) \end{bmatrix} \quad (3.47)$$

where $\mathbf{T}_{ob}(k)$ is the local orthogonal-to-oblique transformation, and K_u and K_v are the friction and normal cutting force coefficients, respectively ([76]). $\mathbf{T}_{ob}(k)$ maps the parameters from the UV to TFR coordinates shown in Figure 3.9. Due to the variation of oblique angles along the cutting edge, this transformation must be calculated locally for each chip element k as:

$$\begin{aligned} \mathbf{T}_{ob}(k) &= \begin{bmatrix} \cos \lambda(k) & \sin \lambda(k) & 0 \\ -\sin \lambda(k) & \cos \lambda(k) & 0 \\ 0 & 0 & 1 \end{bmatrix} \begin{bmatrix} \cos \alpha(k) & 0 & \sin \alpha(k) \\ 0 & 1 & 0 \\ -\sin \alpha(k) & 0 & \cos \alpha(k) \end{bmatrix} \begin{bmatrix} 0 & 1 \\ \sin \eta(k) & 0 \\ \cos \eta(k) & 0 \end{bmatrix} \\ &= \begin{bmatrix} \sin \lambda(k) \sin \eta(k) + \cos \lambda(k) \sin \alpha(k) \cos \eta(k) & \cos \lambda(k) \cos \alpha(k) \\ \cos \alpha(k) \cos \eta(k) & -\sin \alpha(k) \\ -\cos \lambda(k) \sin \eta(k) + \sin \lambda(k) \sin \alpha(k) \cos \eta(k) & \sin \lambda(k) \cos \alpha(k) \end{bmatrix} \end{aligned} \quad (3.48)$$

where $\alpha(k)$ and $\lambda(k)$ are the local effective rake and inclination angles calculated in Eqs. (3.35) and (3.36), respectively; $\eta(k)$ is the local chip flow angle, which is assumed equal to the inclination angle, i.e. $\eta(k) = \lambda(k)$ [75].

Figure 3.13 illustrates the cutting edge and the chip removal mechanism. Typical threading inserts have edge radius of around $50 \mu\text{m}$ ². During the cutting process, some of the material is compressed under the round section of the cutting edge, resulting in higher friction and normal forces. The effect of ploughing becomes more significant when the chip thickness is equal to or smaller than the edge radius. In threading buttress profile, the chip thickness on the sides is typically few microns while the chip load at the root can be as large as 0.5 mm. Therefore, linearization of cutting force coefficients is not a realistic assumption. This thesis uses nonlinear Kienzle force model [77]; the friction (K_u) and normal (K_v) cutting coefficients are modelled as (see Figure 3.15):

$$K_i = k_{c1,i}(\bar{h})^{-m_{c,i}}, \quad i = u, v \quad (3.49)$$

²Measured by the author for several inserts during his industrial internship at Sandvik Coromant, Sweden, 2014.

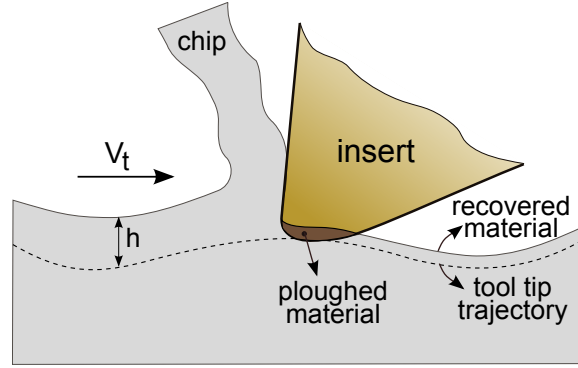


Figure 3.13: Ploughing and the effect of edge radius.

where k_{c1} and m_c are the Kienzle coefficients, and \bar{h} is the average chip thickness calculated for each element k as:

$$\bar{h}(k) = \frac{1}{2} (|\mathbf{h}(k)| + |\mathbf{h}(k+1)|) \quad (3.50)$$

where $\mathbf{h}(k)$ and $\mathbf{h}(k+1)$ are defined in Eqs. (3.43) and (3.44), respectively. The cutting coefficients K_u and K_v in Eq. (3.49) depend on the workpiece material, insert coating, edge radius, chip thickness, cutting speed, and other tool-workpiece characteristics. Finite element modelling can be used to predict these coefficients semi-analytically using slip line field [78]. In this thesis, however, in order to minimize the errors originating from the cutting coefficients, K_u and K_v have been identified experimentally as presented in Section 3.7.1.

3.6.3 Total Cutting Forces

The local static cutting forces for each chip element k are obtained from Eqs. (3.41) and (3.47):

$$\mathbf{F}_{s,L}(k) = \begin{Bmatrix} F_{tc}(k) \\ F_{fc}(k) \\ F_{rc}(k) \end{Bmatrix} = \mathbf{T}_{ob}(k) \begin{bmatrix} K_u(k) \\ K_v(k) \end{bmatrix} \cdot A_c(k) \quad (3.51)$$

where $A_c(k)$ and $[\mathbf{T}_{ob}(k)]_{3 \times 2}$ are defined in Eqs. (3.42) and (3.48), respectively. The local forces are projected in the global coordinates as:

$$\mathbf{F}_s(k) = \begin{Bmatrix} F_{s,x}(k) \\ F_{s,y}(k) \\ F_{s,z}(k) \end{Bmatrix} = \mathbf{T}_{LG}(k) \begin{Bmatrix} F_{tc}(k) \\ F_{fc}(k) \\ F_{rc}(k) \end{Bmatrix} \quad (3.52)$$

where $[\mathbf{T}_{LG}(k)]_{3 \times 3}$ is the local-to-global transformation at the location of element k :

$$\mathbf{T}_{LG}(k) = [\{\mathbf{U}_{tc}(k)\}, \{\mathbf{U}_{fc}(k)\}, \{\mathbf{U}_{rc}(k)\}] \quad (3.53)$$

where \mathbf{U}_{ic} , $i = t, f, r$, are the local unit direction vectors (Figure 3.11.b) defined in Eqs. (3.38)-(3.40). The resultant cutting force vector on each tooth j is calculated by summing all the elemental forces on the tooth, i.e:

$${}^j\mathbf{F}_s = \begin{Bmatrix} {}^jF_{s,x} \\ {}^jF_{s,y} \\ {}^jF_{s,z} \end{Bmatrix} = \sum_{k=1}^{jN_e} {}^j\mathbf{F}_s(k) = \sum_{k=1}^{jN_e} \{F_{tc}(k)\mathbf{U}_{tc}(k) + F_{fc}(k)\mathbf{U}_{fc}(k) + F_{rc}(k)\mathbf{U}_{rc}(k)\}_j \quad (3.54)$$

where ${}^jN_e = {}^jN_u$ is the number of chip elements (points on the upper band) on tooth j . Finally, the total cutting forces exerted on the insert are obtained as:

$$\mathbf{F}_s = \sum_{j=1}^{N_t} ({}^j\mathbf{F}_s) \quad (3.55)$$

where N_t is the total number of teeth engaged in the cut.

3.7 Experimental Validation of Mechanics Model

In order to validate the proposed force prediction model, numerous sets of threading experiments have been conducted using different inserts and infeed plans. Sample results are presented in this section. ³

³All experiments in this section were carried out at Sandvik Coromant in Sweden during the author's industrial internship in 2014.

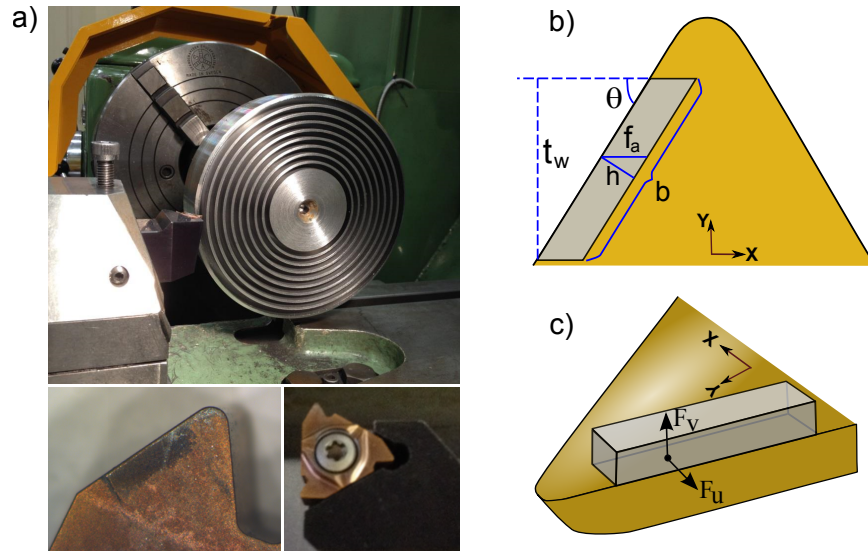


Figure 3.14: Semi-orthogonal tests, a) experimental setup (insert: Sandvik Coromant), b) chip geometry, c) friction and normal forces.

3.7.1 Semi-Orthogonal Identification Tests

In order to identify the cutting force coefficients, a set of semi-orthogonal cutting tests have been performed using a V-profile threading insert. As shown in Figure 3.14.a, a workpiece with concentric tubes of 1.95 mm wall thickness has been prepared by opening circular slots on the face of a solid cylinder. The workpiece material is AISI 1045, and the insert is Sandvik Coromant 22V401A0503E V-profile (60°). The cutting tool has been positioned such that only one straight edge of the insert cuts the workpiece, and the round nose is out of cut. Each tube has been cut at different values of axial feedrate f_a in the range of 0.056-0.615 mm/rev. Cutting speed in all experiments is 150 m/min.

As illustrated in Figure 3.14.b, the width (b) and thickness (h) of the chip in each test is calculated as:

$$h = f_a \sin \theta \quad , \quad b = t_w / \sin \theta \quad (3.56)$$

where $t_w = 1.95$ mm is the wall thickness and $\theta = 60^\circ$ is the approach angle⁴. The forces have been measured using a 3-axis Kistler 9121 turning dynamometer, and data acquisition has been implemented in CUTPRO[®] MALDAQ software [79].

⁴Due to the fixed orientation of the tool and dynamometer, positioning the cutting edge normal to the feed direction was not possible

Table 3.1: Parameters and measured forces in the semi-orthogonal identification tests (material: AISI 1045, cutting speed: 150 m/min, insert: Sandvik Coromant V-profile).

f_a [mm/rev]	h [mm]	b [mm]	F_x [N]	F_y [N]	F_z [N]	F_u [N]	F_v [N]
0.056	0.048	2.252	274	161	383	318	383
0.063	0.055	2.252	297	173	417	343	417
0.080	0.069	2.252	356	208	509	412	509
0.098	0.085	2.252	396	233	582	460	582
0.126	0.109	2.252	453	268	708	527	708
0.154	0.133	2.252	502	302	826	585	826
0.196	0.170	2.252	528	322	970	618	970
0.252	0.218	2.252	586	367	1184	691	1184
0.308	0.267	2.252	754	458	1465	882	1465
0.392	0.339	2.252	782	495	1776	925	1776
0.615	0.533	2.252	954	617	2562	1135	2562

The axes of the dynamometer are aligned with the global coordinates, i.e. XYZ in the axial, radial, and tangential directions, respectively. The normal force (F_v) and friction force (F_u) (Figure 3.14.c) are determined as:

$$F_u = F_x \sin \theta + F_y \cos \theta \quad , \quad F_v = F_z \quad (3.57)$$

Table 3.1 provides the settings and the measured forces.

For each test, cutting force coefficients K_u and K_v are obtained by dividing the corresponding forces by the chip area, i.e. $K_i = F_i/(bh)$, $i = u, v$. Figure 3.15 shows the cutting force coefficients plotted as a function of chip thickness. It can be seen that the trend is highly nonlinear due to the effect of ploughing (Figure 3.13) especially below $50 \mu\text{m}$. Least square method has been used to fit a nonlinear Kienzle model (Eq. 3.49) to this data, resulting in:

$$\begin{aligned} k_{c1,u} &= 1204.3 \text{ MPa} \quad , \quad m_{c,u} = 0.384 \\ k_{c1,v} &= 691.6 \text{ MPa} \quad , \quad m_{c,v} = 0.534 \end{aligned} \quad (3.58)$$

These coefficients are used in all the threading experiments presented in the next section.

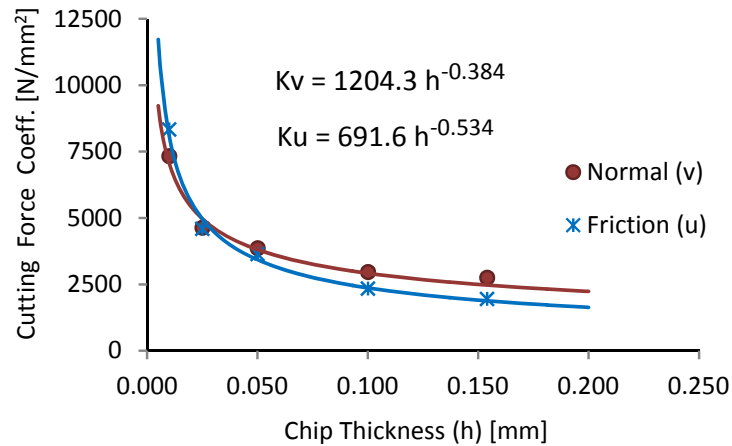


Figure 3.15: Experimentally identified cutting force coefficients (material: AISI 1045, cutting speed: 150 m/min).

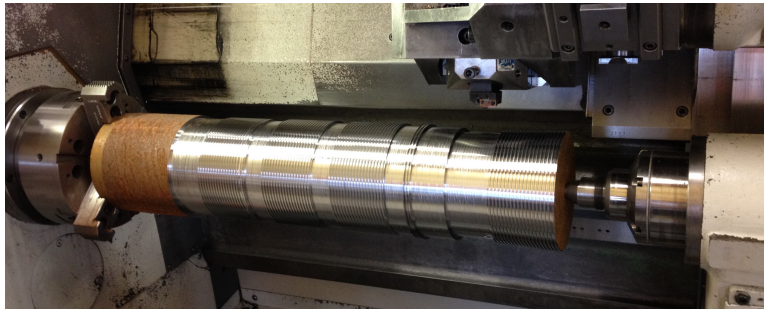


Figure 3.16: Setup for the threading experiments. Workpiece material: AISI 1045, diameter: 176 mm, cutting speed: 150 m/min.

3.7.2 Validation of Threading Force Prediction

Figure 3.16 shows the setup used for the threading tests. The workpiece is AISI 1045 solid cylinder with diameter of 176 mm; it has been restricted by a tailstock at the end to avoid deflections and chatter vibrations. The cutting speed and thread pitch in all experiments are 150 m/min and 5 mm⁵, respectively. The forces have been measured using a 3-axis Kistler turning dynamometer with the load capacity of 25 KN, and data acquisition has been implemented in CUTPRO[®] MALDAQ software [79].

⁵More accurately, the pitch is 5 TPI (thread per inch), i.e. 25.4/5=5.08 mm (API Standard [5]).

V-Profile

For this set of experiments, Sandvik Coromant 266RG-22V401A0503E V-profile insert with nose angle of 60° and nose radius of 0.5 mm has been used. Figure 3.17.a compares the predicted and measured cutting forces in the tangential, radial, and axial directions for 14 passes of 0.15 mm/pass radial infeed. The chip thickness at the nose is equal to the infeed, i.e. 0.15 mm, and the chip load on the sides is $0.15 \sin(30^\circ) = 0.075$ mm. The axial forces are relatively small due to the symmetry of the insert profile. It can be seen that all the predicted forces agree with the measurements within 95% accuracy. Figure 3.17.b shows the results for the same operation but using 6 passes of 0.3 mm/pass. The accuracy of predictions in this case lies within 80% for all passes. The details are provided in Tables 3.2 and 3.3.

It can be observed that in both Figures 3.17.a and b, the discrepancies between the predicted and measured forces grow as the insert penetrates deeper into the thread. This is caused by two main reasons:

1. At deeper passes, a longer part of the tooth is engaged in the cut resulting in wider chip and more severe chip interference.
2. Due to severe ploughing of material under the cutting edge in the preceding passes, surface hardness increases incrementally as a result of strain hardening, which has not been modelled in this thesis. Chip thickness (infeed) is particularly smaller in deeper passes (to limit the forces), leading to severer ploughing in deeper passes. The strain hardening effect can be included by updating the cutting force coefficients over each pass based on the new characteristics of the cut surface. This can be done by predicting the surface hardness using finite element simulations. Alternatively, the cutting force coefficients subject to strain hardening can be identified experimentally by repeated orthogonal cutting tests on the same surface.

The accuracy of the proposed mechanics model can be improved by modelling the effect of stain hardening.

Figure 3.17.c compares the simulated and measured forces for the same insert with flank infeed of 0.15 mm/pass. The resultant chip load is 0.15 mm on one side of the insert and zero on the other side. The detailed infeed parameters and forces

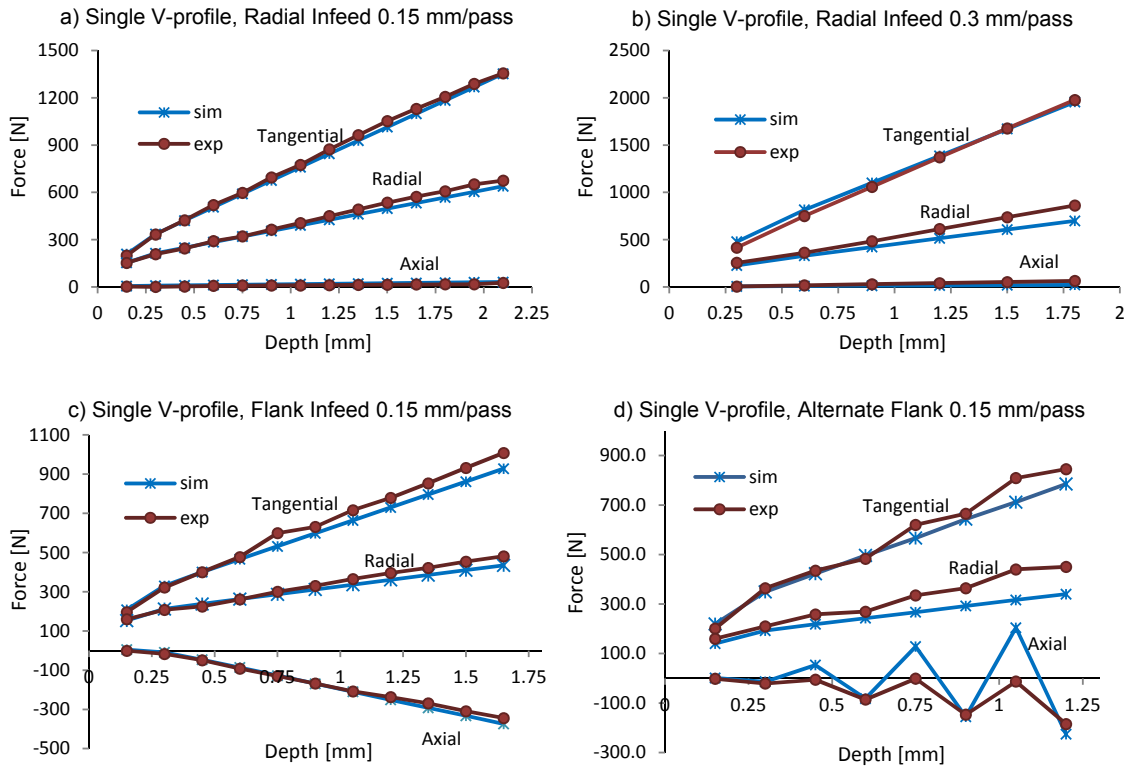


Figure 3.17: Simulated and measured cutting forces for threading with single V-profile insert (Sandvik Coromant 22V401A0503E, workpiece material: AISI 1045, diameter: 176 mm, thread pitch: 5 mm, cutting speed: 150 m/min)

are provided in Table 3.4. Even though the simulation and experiment still agree within 90%, the discrepancy is slightly larger compared to the same operation with radial infeed (Figure 3.17.a). This is due to the fact that in flank infeed plan, one side of the insert is constantly rubbing on the thread surface, resulting in higher forces.

Figure 3.17.d shows the simulated and measured forces for the case of alternate flank infeed with 0.15 mm/pass. The details are provided in Table 3.5. The axial offset has been set in the same direction as the feed for even pass numbers, and opposite to feed for odd passes (see Figures 1.2.a and 3.3.c). It can be seen that there is a close agreement over even passes; for odd pass numbers, however, the simulation predicts relatively large axial forces (due to single-edge cutting) while the measured axial forces are almost zero. This means that the free side of the insert, which is supposed to be sliding freely on the thread surface, is in fact experiencing

Table 3.2: Simulated and measured forces in threading with V-profile insert; radial infeed plan at 0.15 mm/pass (Figure 3.17.a).

Pass	Infeed Δa [mm]	Depth a [mm]	Simulation			Experiment		
			F_x [N]	F_y [N]	F_z [N]	F_x [N]	F_y [N]	F_z [N]
1	0.15	0.15	5	153	208	-2	153	199
2	0.15	0.30	8	213	335	0	208	333
3	0.15	0.45	10	249	421	3	245	423
4	0.15	0.60	12	284	506	7	291	520
5	0.15	0.75	14	320	591	9	321	597
6	0.15	0.90	16	355	675	9	364	695
7	0.15	1.05	18	391	760	10	405	774
8	0.15	1.20	20	426	845	11	450	873
9	0.15	1.35	21	461	929	13	492	963
10	0.15	1.50	23	497	1014	14	535	1052
11	0.15	1.65	25	533	1099	16	572	1130
12	0.15	1.80	27	568	1183	17	607	1206
13	0.15	1.95	29	603	1268	17	651	1289
14	0.15	2.10	31	640	1353	26	675	1355

Table 3.3: Simulated and measured forces in threading with V-profile insert; radial infeed plan at 0.3 mm/pass (Figure 3.17.b).

Pass	Infeed Δa [mm]	Depth a [mm]	Simulation			Experiment		
			F_x [N]	F_y [N]	F_z [N]	F_x [N]	F_y [N]	F_z [N]
1	0.3	0.3	5	227	478	5	255	416
2	0.3	0.6	9	330	816	17	362	750
3	0.3	0.9	12	422	1101	29	483	1059
4	0.3	1.2	15	514	1386	40	612	1370
5	0.3	1.5	18	606	1671	51	738	1676
6	0.3	1.8	22	699	1955	63	861	1977

Table 3.4: Simulated and measured forces in threading with V-profile insert; flank infeed plan at 0.15 mm/pass (Figure 3.17.c).

Pass	Infeed Δa [mm]	Depth a [mm]	Simulation			Experiment		
			F_x [N]	F_y [N]	F_z [N]	F_x [N]	F_y [N]	F_z [N]
1	0.15	0.15	5	153	208	-1	160	196
2	0.15	0.30	-9	213	330	-17	208	322
3	0.15	0.45	-46	238	400	-49	225	400
4	0.15	0.60	-86	263	466	-92	261	477
5	0.15	0.75	-128	287	532	-130	300	599
6	0.15	0.90	-169	312	598	-168	330	631
7	0.15	1.05	-209	336	664	-208	365	716
8	0.15	1.20	-251	361	730	-237	396	779
9	0.15	1.35	-292	385	796	-269	422	853
10	0.15	1.50	-333	410	862	-309	454	932
11	0.15	1.65	-374	435	928	-344	481	1008

Table 3.5: Simulated and measured forces in threading with V-profile insert; alternate flank infeed at 0.15 mm/pass (Figure 3.17.d).

Pass	Infeed Δa [mm]	Depth a [mm]	Simulation			Experiment		
			F_x [N]	F_y [N]	F_z [N]	F_x [N]	F_y [N]	F_z [N]
1	0.15	0.15	1	140	219	-2	160	201
2	0.15	0.30	-14	193	349	-21	210	364
3	0.15	0.45	53	218	423	-6	258	435
4	0.15	0.60	-82	243	496	-86	269	483
5	0.15	0.75	128	267	567	-2	335	620
6	0.15	0.90	-155	292	643	-147	364	665
7	0.15	1.05	204	316	712	-13	440	809
8	0.15	1.20	-226	340	785	-185	450	845

severe rubbing. The rubbing force counteract the cutting forces of the engaged side, resulting in smaller total axial force. The friction and normal rubbing forces cause an increase in the tangential and radial forces as well. Flank rubbing must be reduced through insert design and has not been modelled in this thesis. The agreement between the simulation and experiment over even pass numbers still prove that the model can predict the cutting forces accurately if rubbing is avoided.

Single Buttress Insert

In the second set of threading experiments, Sandvik Coromant single buttress insert (266RG-22BU01A050E) has been used to cut 17 passes at radial infeed of 0.075 mm/pass. The resultant chip thickness on the left and right sides of the tooth are 13 μm and 4 μm , respectively (see Figure 1.1.c). Figure 3.18.a compares the simulated and measured forces, and Table 3.6 provides the detailed data. While there is a close agreement over the first half of passes, the deviation grows towards the end. The insert was examined after the experiment, and large shiny patches were found on the side flank faces. These shiny areas are caused due to the severe grinding between the flank face and the thread surface, which result in additional forces. Rubbing must be reduced through insert design and is not modelled here.

Twin Buttress Insert

In the final set, a Sandvik Coromant Tmax Twin-Lock two-point API buttress insert (R166.39G-24BU12-050) has been used to cut the same buttress profile but using two teeth. The radial depth of the second tooth with respect to the first tooth is 0.26 mm, and the infeed values over the first, second, and third passes are 0.46 mm, 0.44 mm, and 0.40 mm, respectively. Based on the insert design, the first tooth mainly performs rough cutting of the root, and the second tooth performs finishing of the thread profile (see Figure 3.4.a). Figure 3.18.b compares the simulated and measured forces, and Table 3.7 provides the detailed data. It can be seen that the

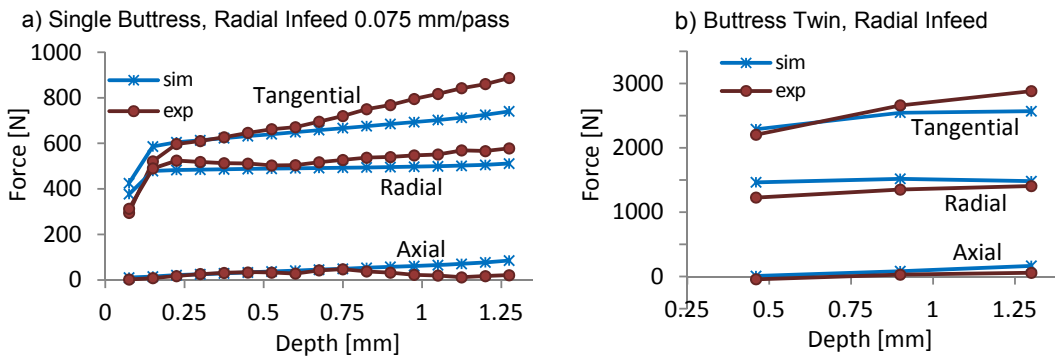


Figure 3.18: Simulated and measured cutting forces for threading with single and two-point API buttress inserts (Sandvik Coromant API Buttress Full Form and Twin, material AISI 1045, cutting speed: 150 m/min, workpiece diameter: 176 mm, thread pitch: 5 mm)

Table 3.6: Simulated and measured forces in threading with single buttress insert; radial infeed at 0.075 mm/pass (Figure 3.18.a).

Pass	Infeed Δa [mm]	Depth a [mm]	Simulation			Experiment		
			F_x [N]	F_y [N]	F_z [N]	F_x [N]	F_y [N]	F_z [N]
1	0.075	0.075	8	326	374	2	313	295
2	0.075	0.150	13	436	569	8	490	521
3	0.075	0.225	18	441	588	17	524	597
4	0.075	0.300	21	442	596	27	518	610
5	0.075	0.375	23	443	602	31	513	627
6	0.075	0.450	26	444	608	33	511	646
7	0.075	0.525	29	446	614	33	503	662
8	0.075	0.600	32	447	620	28	504	671
9	0.075	0.675	35	448	626	42	517	695
10	0.075	0.750	37	449	632	47	527	720
11	0.075	0.825	40	450	638	38	537	750
12	0.075	0.900	43	451	645	32	540	768
13	0.075	0.975	46	452	651	23	547	795
14	0.075	1.050	48	453	657	20	551	817
15	0.075	1.125	51	454	663	12	569	842
16	0.075	1.200	54	456	669	17	566	860
17	0.075	1.275	57	457	675	21	578	887

Table 3.7: Simulated and measured forces in threading with twin buttress insert (Figure 3.18.b).

Pass	Infeed Δa [mm]	Depth a [mm]	Simulation			Experiment		
			F_x [N]	F_y [N]	F_z [N]	F_x [N]	F_y [N]	F_z [N]
1	0.46	0.46	7	1463	2289	-45	1226	2204
2	0.44	0.90	81	1517	2546	27	1350	2660
3	0.40	1.30	164	1480	2569	57	1405	2881

simulation and experiment agree within 85% accuracy for all passes.

3.8 Summary

This chapter presents a generalized and semi-analytical approach to model the chip geometry and predict the cutting forces in thread turning with custom multi-point inserts. The boundaries of the chip are determined based on the insert geometry, infeed settings, and kinematics of the process. A systematic search algorithm has

been proposed to discretize the chip area along the cutting edge considering the local chip flow direction and the effect of chip interference. Cutting force coefficients are evaluated locally for each chip element, and the total cutting forces are determined by summation of the element forces. The proposed mechanics model has been verified experimentally for V-profile, single buttress, and twin buttress inserts with different infeed plans; the methodology and results have been published in [1].

Chapter 4

Dynamics of Multi-Point Threading

4.1 Overview

This chapter investigates the general dynamics of multi-point thread turning operations. Section 4.2 studies the chip regeneration mechanism, followed by modelling the dynamic forces in Section 4.3 to 4.5. Equations of motion in frequency and time domain (modal space) are derived in Sections 4.6 and 4.7, respectively. A time-marching numerical simulation method based on semi-discretization and Simpson's integration rule is presented in Section 4.8, followed by sample results in Section 4.9. The proposed mechanics and dynamics models are used to develop a process optimization algorithm in Section 4.11, and the chapter is concluded in Section 4.12.

4.2 Chip Regeneration Mechanism

The static cutting force vector F_s in Chapter 3 has been derived based on the nominal (planned) infeed settings. Relative vibrations between the tool and workpiece result in two additional components: 1) dynamic cutting force F_d due to chip thickness variation, 2) process damping force F_p due to dynamic indentation of the flank face into the cut surface. The total force vector exerted on the tool at time t is:

$$\{F_c(t)\}_{3 \times 1} = F_s(t) + F_d(t) + F_p(t) \quad (4.1)$$

where the static force $F_s(t)$ has been written as a time-dependent variable to account for the transient condition at the start of the operation (see Section 4.5 for details).

Assume that the deflection of the tool and workpiece at the cutting point due to the structural flexibilities are represented in the three-dimensional coordinates as $\{\mathbf{q}_t(t)\}_{3 \times 1}$ and $\{\mathbf{q}_w(t)\}_{3 \times 1}$, respectively. Relative vibration between the tool and workpiece is obtained as:

$$\mathbf{q}(t) = \mathbf{q}_t(t) - \mathbf{q}_w(t) = \begin{Bmatrix} q_{t,x}(t) - q_{w,x}(t) \\ q_{t,y}(t) - q_{w,y}(t) \\ q_{t,z}(t) - q_{w,z}(t) \end{Bmatrix} = \begin{Bmatrix} q_x(t) \\ q_y(t) \\ q_z(t) \end{Bmatrix} \quad (4.2)$$

It is assumed that the width of the insert is considerably smaller than the length of the workpiece, hence $\mathbf{q}(t)$ is the same for all teeth. The vibration vector at one spindle revolution before is represented as $\mathbf{q}(t - T)$, or in Laplace domain as $\mathbf{q}(s)e^{-Ts}$, where T is the spindle period.

Figure 4.1.a illustrates the effect of current and previous vibrations on the chip thickness. Regeneration mechanism in multi-point threading is different than regular turning in that the vibration marks left by each tooth affect the chip thickness on a different tooth. It involves additional complexities due to the fact that the teeth may have different profiles (see Chapter 3). The closed loop dynamics of chip regeneration in each pass is illustrated in Figure 4.1.b. Δa and ε_{fx} are the infeed settings for the pass, $\mathbf{q}(s)$ is the relative vibration vector in Laplace domain, and $\mathbf{G}(s)$ represents the structural dynamics of the tool-workpiece setup.

Dynamic chip thickness and the resultant dynamic forces are derived in the following section.

4.3 Calculation of Dynamic Cutting Forces

Figure 4.2 illustrates a sample threading chip and the effect of current and previous vibrations. At each point along the cutting edge, only the vibration component in the local feed direction affects the chip thickness. A systematic methodology is proposed in this section to calculate the dynamic forces along the threading insert.

4.3.1 Dynamic Chip on The Upper Band

As illustrated in Figure 4.2, the upper band of the chip corresponds to the current tooth-workpiece engagement. For each chip element k along the cutting edge, the

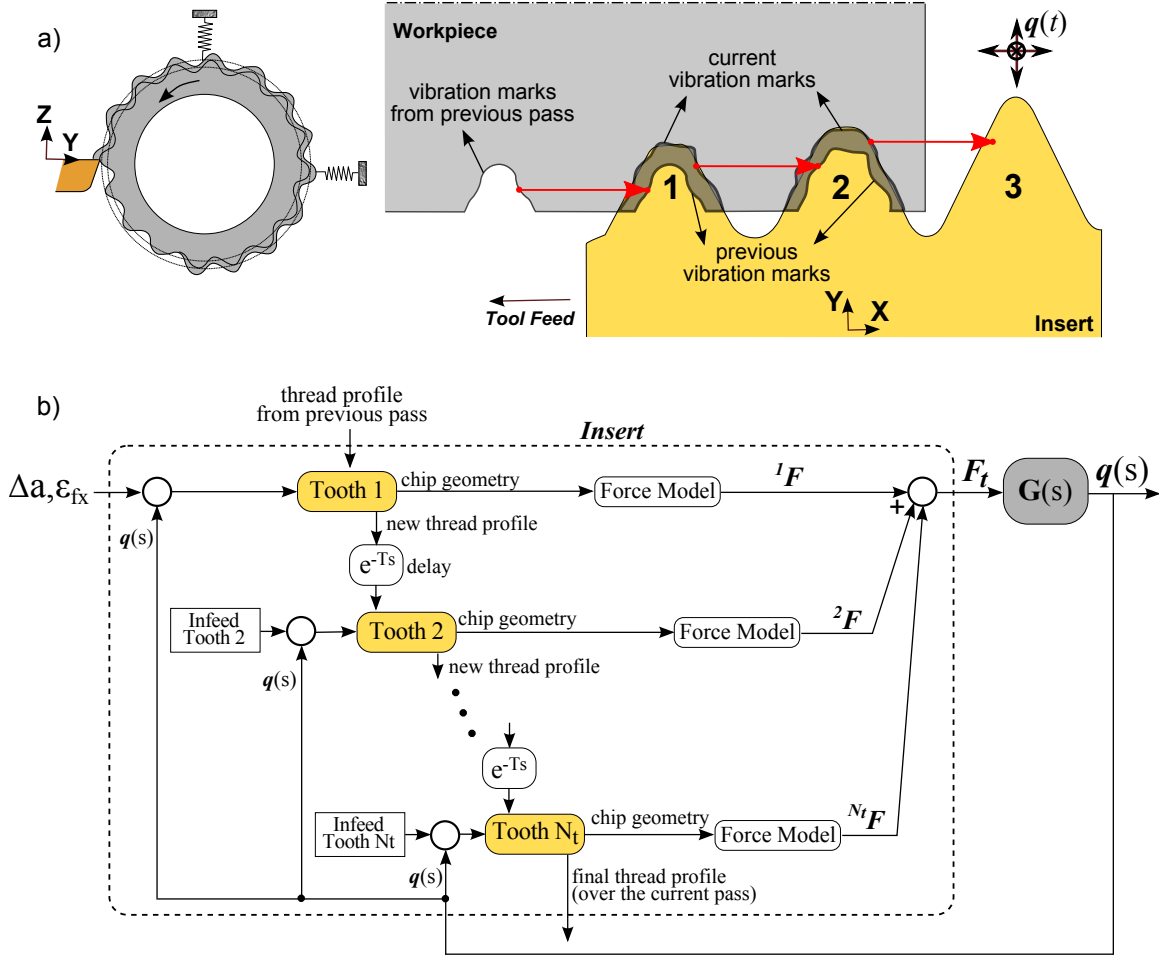


Figure 4.1: Chip regeneration mechanism in multi-point thread turning.

unit vector in the local feed (chip thickness) direction can be obtained as:

$$\mathbf{U}_{fu}(k) = \frac{\mathbf{b}_u(k) \times \mathbf{V}_t}{|\mathbf{b}_u(k) \times \mathbf{V}_t|} \quad (4.3)$$

where \times denotes cross product, $\mathbf{b}_u(k)$ is the element's edge vector on the upper band (Eq. (3.45)), and \mathbf{V}_t is the total velocity vector calculated in Eq. (3.29). The local dynamic chip thickness on the upper band, i.e. $h_{du}(k, t)$, is obtained by projecting the relative vibration vector in the direction of local chip thickness:

$$h_{du}(k, t) = \mathbf{q}(t) \cdot \mathbf{U}_{fu}(k) = U_{fu,x}(k) q_x(t) + U_{fu,y}(k) q_y(t) + U_{fu,z}(k) q_z(t) \quad (4.4)$$

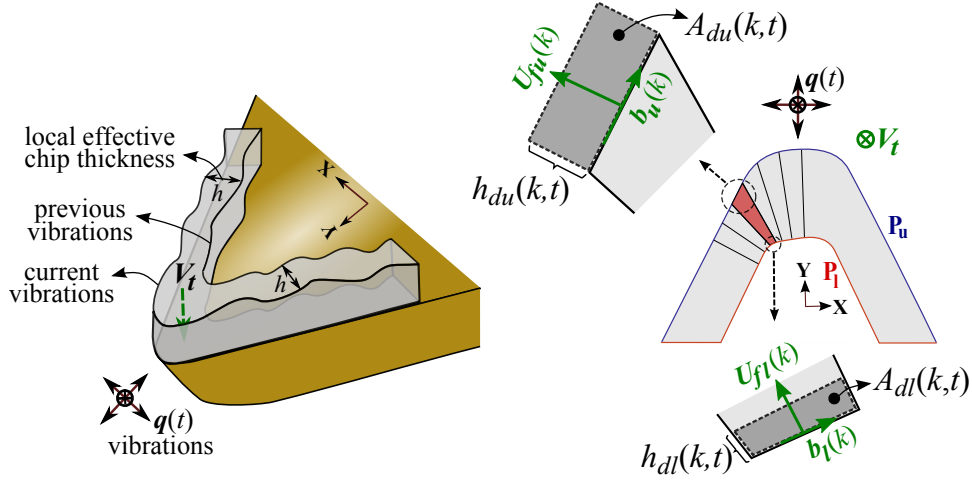


Figure 4.2: Dynamic chip area due to the current and previous vibrations.

or in matrix form:

$$h_{du}(k,t) = \{\mathbf{U}_{fu}(k)\}^T \mathbf{q}(t) \quad (4.5)$$

Note that $h_{du}(k,t)$ can take negative values when the tool and workpiece deflect away from each other. The dynamic chip area on the upper band (Figure 4.2) can be calculated as:

$$A_{du}(k,t) = |\mathbf{b}_u(k)| h_{du}(k,t) = |\mathbf{b}_u(k)| \{\mathbf{U}_{fu}(k)\}^T \mathbf{q}(t) \quad (4.6)$$

where $\mathbf{b}_u(k)$ is the width vector on the upper band (Eq. (3.45)). Negative dynamic chip thickness results in negative dynamic chip area until the cutter disengages from the workpiece due to large vibrations (see Section 4.8.1). Using Eq. (3.51), the dynamic cutting force vector on chip element k due to the current vibrations is obtained as:

$$\mathbf{F}_{du}(k,t) = [\mathbf{T}_{ob}(k)]_{3 \times 2} \begin{bmatrix} K_u(k) \\ K_v(k) \end{bmatrix} \cdot A_{du}(k,t) \quad (4.7)$$

where $\mathbf{T}_{ob}(k)$ is the local orthogonal-to-oblique transformation (Eq. (3.48)), and $K_u(k)$ and $K_v(k)$ are the local friction and normal cutting force coefficients (Eq. (3.49)), respectively.

Remark: Based on Kienzle model (Eq. (3.49)), K_u and K_v are functions of instantaneous chip thickness. This means that vibrations affect not only the chip area but also the cutting force coefficients. As a result, K_u and K_v in Eq. (4.7)

are time dependent. In order to reduce the numerical computation, it is assumed in this thesis that vibrations are sufficiently smaller than the static (nominal) chip thickness. Hence, the dependency of cutting force coefficients on dynamic chip thickness is neglected.

4.3.2 Dynamic Chip on The Lower Band

As illustrated in Figures 4.1 and 4.2, the effect of previous vibrations appear as dynamic chip on the lower band. Since these vibration marks are generated by the profile of the previous tooth, $\mathbf{q}(t - T)$ must be projected in the local feed direction at each point along the previous tooth. Since the lower band on the current tooth matches the cutting edge of the previous tooth, the dynamic chip thickness due to previous vibrations can be calculated as (Figure 4.2):

$$\begin{aligned} h_{dl}(k, t) &= -\{\mathbf{U}_{fl}(k)\}^T \mathbf{q}(t - T) \\ &= -[U_{fl,x}(k)q_x(t - T) + U_{fl,y}(k)q_y(t - T) + U_{fl,z}(k)q_z(t - T)] \end{aligned} \quad (4.8)$$

where the minus sign is to account for the fact that positive vibrations over the previous cut (overcutting) result in reduction in the chip thickness on the current tooth. $\mathbf{U}_{fl}(k)$ in Eq. (4.8) is the unit vector in the local feed direction on the lower band:

$$\mathbf{U}_{fl}(k) = \frac{\mathbf{b}_l(k) \times \mathbf{V}_t}{|\mathbf{b}_l(k) \times \mathbf{V}_t|} \quad (4.9)$$

where \mathbf{b}_l is the width vector defined in Eq. (3.46). For each chip element k along the cutting edge, the dynamic chip area due to the previous vibration marks (Figure 4.2) can be calculated as:

$$A_{dl}(k, t) = |\mathbf{b}_l(k)| h_{dl}(k, t) = -|\mathbf{b}_l(k)| \{\mathbf{U}_{fl}(k)\}^T \mathbf{q}(t - T) \quad (4.10)$$

and the corresponding dynamic cutting force vector on the lower band is:

$$\mathbf{F}_{dl}(k, t) = [\mathbf{T}_{ob}(k)]_{3 \times 2} \begin{bmatrix} K_u(k) \\ K_v(k) \end{bmatrix} \cdot A_{dl}(k, t) \quad (4.11)$$

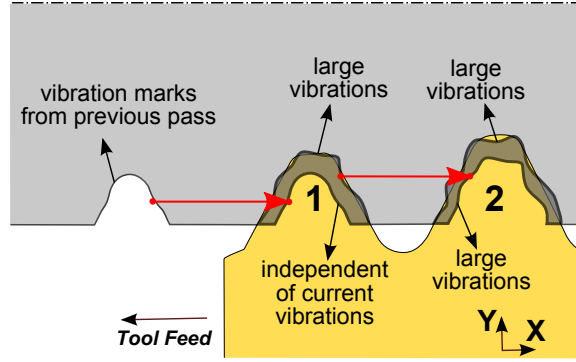


Figure 4.3: Chip regeneration on the first tooth.

4.3.3 Dynamic Chip on The First Tooth

The first tooth has a different chip regeneration mechanism. Assume that the previous pass was stable with relatively small vibrations. As illustrated in Figure 4.3, if the current pass causes large vibrations, the resultant marks appear on both the lower and upper bands of all teeth except the first tooth. Vibration marks from the previous pass act as disturbance on the first tooth (Figure 4.1.b), but they do not contribute to the closed loop chip regeneration in the current pass.

In this thesis, the dynamics and stability is analyzed based on the assumption that the previous pass has been stable with small vibrations. As a result, the dynamic chip on the first tooth is generated by only the current vibrations (upper band), as presented in Section 4.3.1.

Remark: Note that since all teeth are rigidly connected to each other, the chip on the first tooth is still indirectly affected by the chip regeneration on the other teeth. Large dynamic forces on even one tooth can lead to large vibrations on all teeth.

4.3.4 Total Dynamic Cutting Forces

The local dynamic cutting force vector is calculated for each element k by adding the components of the upper and lower bands derived in Eqs (4.7) and (4.11), respectively:

$$\mathbf{F}_d(k,t) = [\mathbf{T}_{ob}(k)]_{3 \times 2} \begin{bmatrix} K_u(k) \\ K_v(k) \end{bmatrix} \cdot (A_{du}(k,t) + A_{dl}(k,t)) \quad (4.12)$$

The local force vectors are projected in the global coordinates and summed up over each tooth j :

$$\begin{aligned} {}^j \mathbf{F}_d(t) &= \sum_{k=1}^{jN_e} \{ \mathbf{T}_{LG}(k) \mathbf{F}_d(k,t) \} \\ &= \sum_{k=1}^{jN_e} \{ \mathbf{T}_{LG}(k) \mathbf{T}_{ob}(k) \mathbf{K}_{uv}(k) [|\mathbf{b}_u(k)| h_{du}(k,t) + |\mathbf{b}_l(k)| h_{dl}(k,t)] \} \end{aligned} \quad (4.13)$$

where $\mathbf{K}_{uv} = [K_u, K_v]^T$, and transformation matrix \mathbf{T}_{LG} is defined in Eq. (3.53). Using Eqs. (4.5) and (4.8), the dynamic force vector can be written in terms of the current and previous vibrations as:

$${}^j \mathbf{F}_d(t) = [{}^j \mathbf{K}_{dc}(t)]_{3 \times 3} \{ \mathbf{q}(t) \}_{3 \times 1} - [{}^j \mathbf{K}_{dd}(t)]_{3 \times 3} \{ \mathbf{q}(t-T) \}_{3 \times 1} \quad (4.14)$$

where ${}^j \mathbf{K}_{dc}(t)$ and ${}^j \mathbf{K}_{dd}(t)$ are the equivalent current and delayed dynamic force coefficients:

$$\begin{aligned} [{}^j \mathbf{K}_{dc}(t)]_{3 \times 3} &= \sum_{k=1}^{jN_e} [\mathbf{T}_{LG}(k) \mathbf{T}_{ob}(k) \mathbf{K}_{uv}(k) |\mathbf{b}_u(k)| \mathbf{U}_{fu}(k)] \\ [{}^j \mathbf{K}_{dd}(t)]_{3 \times 3} &= \begin{cases} [\mathbf{0}]_{3 \times 3} & \text{if } j = 1 \\ \sum_{k=1}^{jN_e} [\mathbf{T}_{LG}(k) \mathbf{T}_{ob}(k) \mathbf{K}_{uv}(k) |\mathbf{b}_l(k)| \mathbf{U}_{fl}(k)] & \text{if } j > 1 \end{cases} \end{aligned} \quad (4.15)$$

and ${}^j N_e$ is the number of chip elements on tooth j . Note that the first tooth has been excluded from the delayed term.

4.4 Calculation of Process Damping Forces

As illustrated in Figure 4.4.a, process damping forces are generated due to the indentation of the flank face of the tool in the undulated cut surface when the tool is vibrating in the direction of chip thickness. As modelled by Shaw and DeSalvo [51], the component in the feed direction, F_{pf} , is proportional to the volume of the compressed material (V_{cm}) under the flank face of the tool:

$$F_{pf} = K_{sp} V_{cm} \quad (4.16)$$

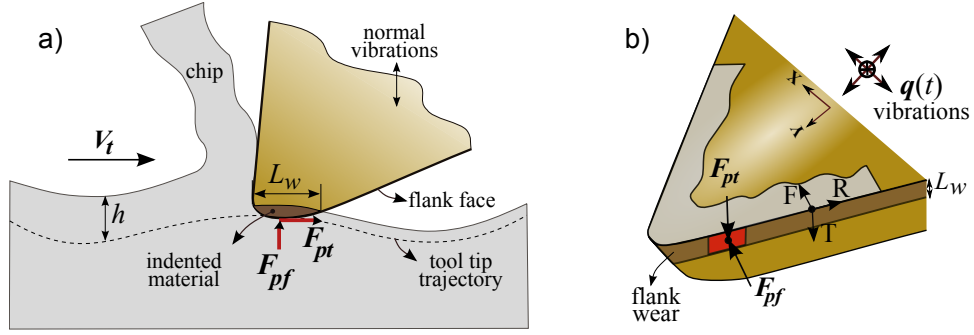


Figure 4.4: Local process damping forces in threading.

where K_{sp} is the material-dependent indentation force coefficient obtained experimentally. The normal force, F_{pf} , induces a dynamic friction force in the tangential direction:

$$F_{pt} = \mu F_{pf} \quad (4.17)$$

where μ is the Coulomb friction between the tool and work material, which is assumed as 0.3 for typical metal cutting operations.

Figure 4.4.b illustrates the local process damping forces on a threading tooth. Similar to the static and dynamic cutting forces, the direction and magnitude of process damping components vary along the cutting edge. As proposed by Chiou and Liang [52], the volume of the compressed material is proportional to the vibration velocity in the direction of chip thickness (feed). The relative vibration velocity between the tool and workpiece is obtained from Eq. (4.2) as:

$$\dot{\mathbf{q}}(t) = \frac{d\mathbf{q}(t)}{dt} = \dot{\mathbf{q}}_t(t) - \dot{\mathbf{q}}_w(t) \quad (4.18)$$

For each element k along the cutting edge, $\dot{\mathbf{q}}(t)$ is projected in the direction of local chip thickness as:

$$\{\mathbf{U}_{fu}(k)\}^T \{\dot{\mathbf{q}}(t)\} = U_{fu,x}\dot{q}_x + U_{fu,y}\dot{q}_y + U_{fu,z}\dot{q}_z \quad (4.19)$$

where $\mathbf{U}_{fu}(k)$ is calculated in Eq. (4.3). The cross section of the indented material at the location of element k is obtained using the projected vibration velocity ([52]):

$$A_{cm}(k) = \frac{L_w^2(k)}{2|\mathbf{V}_t|} \mathbf{U}_{fu}(k)^T \dot{\mathbf{q}}(t) \quad (4.20)$$

where \mathbf{V}_t is the total cutting velocity vector, and $L_w(k)$ is the local width of the wear land on the flank face (Figure 4.4.b). The process damping model is sensitive to L_w , therefore L_w is normally measured with a microscope before and after the experiments. L_w is around $100\mu\text{m}$ in typical inserts. The local volume of the indented material is calculated as:

$$V_{cm} = |\mathbf{b}_u(k)|A_{cm}(k) \quad (4.21)$$

where $\mathbf{b}_u(k)$ is the width of the element on the cutting edge (Eq. (3.45)). Hence, the local process damping forces in the feed and tangential directions are:

$$\begin{aligned} F_{pf}(k) &= K_{sp}|\mathbf{b}_u(k)|\frac{L_w^2(k)}{2|\mathbf{V}_t|}\mathbf{U}_{fu}(k)^T\dot{\mathbf{q}}(t) \\ F_{pt}(k) &= \mu F_{pf}(k) \end{aligned} \quad (4.22)$$

where K_{sp} and μ are the indentation and Coulomb friction coefficients, respectively. Considering the directions of these two components (Figure 4.4.b), the process damping force vector represented in the local TFR coordinate system can be written as:

$$\mathbf{F}_{p,L}(k) = \begin{Bmatrix} F_{pt}(k) \\ F_{pf}(k) \\ 0 \end{Bmatrix}_{TFR} = \begin{Bmatrix} \mu \\ 1 \\ 0 \end{Bmatrix} F_{pf}(k) \quad (4.23)$$

$\mathbf{F}_{p,L}(k)$ is projected to the global coordinates using $\mathbf{T}_{LG}(k)$ transformation matrix (Eq. (3.53)). The total process damping force vector on tooth j is then obtained by summation of the element forces:

$${}^j\mathbf{F}_p(t) = \begin{Bmatrix} {}^jF_{p,x} \\ {}^jF_{p,y} \\ {}^jF_{p,z} \end{Bmatrix} = \sum_{k=1}^{jN_e} ([\mathbf{T}_{LG}(k)]_{3 \times 3} \mathbf{F}_{p,L}(k)) = [{}^j\mathbf{C}_p]_{3 \times 3} \{\dot{\mathbf{q}}(t)\}_{3 \times 1} \quad (4.24)$$

where ${}^j\mathbf{C}_p$ is the equivalent process damping coefficient matrix for tooth j :

$$[{}^j\mathbf{C}_p]_{3 \times 3} = \sum_{k=1}^{jN_e} \left(K_{sp}|\mathbf{b}_u(k)|\frac{L_w^2(k)}{2|\mathbf{V}_t|}\mathbf{T}_{LG} \begin{Bmatrix} \mu \\ 1 \\ 0 \end{Bmatrix} \mathbf{U}_{fu}(k)^T \right) \quad (4.25)$$

4.5 Total Forces on The Insert

In order to model the transient condition at the start of the operation when the teeth arrive in the cut one by one, a boolean (unit step) function g_j is defined for each tooth j as:

$$g_j(t) = \mathbf{1}(t - (j-1)T) = \begin{cases} 1 & \text{if } t \geq (j-1)T \\ 0 & \text{otherwise} \end{cases} \quad (4.26)$$

where T is the spindle period. Reference time $t = 0$ is when the first tooth engages in the workpiece, after which a new tooth comes into the cut upon each spindle revolution. Since most machines perform a rapid retract at the end of the threading cycle, the transient condition at the exit has not been considered in this thesis.

Assuming that the width of the threading insert is considerably smaller than the length of the workpiece, the total forces on the tool can be calculated by lump summation of the static, dynamic, and process damping forces on all teeth $j = 1, 2, \dots, N_t$:

$$\{\mathbf{F}_c(t)\}_{3 \times 1} = \sum_{j=1}^{N_t} \{g_j(t) [{}^j\mathbf{F}_s + {}^j\mathbf{F}_d(t) + {}^j\mathbf{F}_p(t)]\} \quad (4.27)$$

Using the expressions obtained for these components in Eqs. (3.54), (4.14), and (4.24), the total force vector can be summarized and re-written in terms of vibration vector $\mathbf{q}(t)$ as:

$$\mathbf{F}_c(t) = \mathbf{F}_s(t) + [\mathbf{K}_{dc}(t)] \mathbf{q}(t) - [\mathbf{K}_{dd}(t)] \mathbf{q}(t - T) + [\mathbf{C}_p(t)] \dot{\mathbf{q}}(t) \quad (4.28)$$

where

$$\mathbf{F}_s(t) = \sum_{j=1}^{N_t} \left\{ g_j(t) \cdot \sum_{k=1}^{jN_e} \left(\underbrace{[\mathbf{T}_{LG}(k)]_{3 \times 3} [\mathbf{T}_{ob}(k)]_{3 \times 2} \begin{Bmatrix} k_{c1u} \bar{h}(k)^{-m_{cu}} \\ k_{c1v} \bar{h}(k)^{-m_{cv}} \end{Bmatrix}}_{\mathbf{K}_e(k)} A_s(k) \right) \right\} \quad (4.29)$$

$$[\mathbf{K}_{dc}(t)]_{3 \times 3} = \sum_{j=1}^{N_t} \left(g_j(t) \sum_{k=1}^{jN_e} \left(\mathbf{K}_e(k) |b_u(k)| \mathbf{U}_{fu}(k)^T \right) \right) \quad (4.30)$$

$$[\mathbf{K}_{dd}(t)]_{3 \times 3} = \sum_{j=2}^{N_t} \left(g_j(t) \sum_{k=1}^{jN_e} \left(\mathbf{K}_e(k) |\mathbf{b}_l(k)| \mathbf{U}_{fl}(k)^T \right) \right) \quad (4.31)$$

$$[\mathbf{C}_p(t)]_{3 \times 3} = \sum_{j=1}^{N_t} \left(g_j(t) \cdot \sum_{k=1}^{jN_e} \left(K_{sp} |\mathbf{b}_u(k)| \frac{L_w^2(k)}{2|\mathbf{V}_l|} \mathbf{T}_{LG} \begin{Bmatrix} \mu \\ 1 \\ 0 \end{Bmatrix} \mathbf{U}_{fu}(k)^T \right) \right) \quad (4.32)$$

where \mathbf{K}_{dc} , \mathbf{K}_{dd} , and \mathbf{C}_p are the equivalent dynamic coefficient matrices corresponding to the current, delayed, and process damping forces on the whole insert.

4.6 Stability Analysis in Frequency Domain

Assume the three-dimensional frequency response functions (FRF) of the tool (\mathbf{G}_t) and workpiece (\mathbf{G}_w) at the cutting location are expressed in Laplace domain as:

$$\mathbf{G}_i(s) = \begin{bmatrix} G_{xx,i}(s) & G_{xy,i}(s) & G_{xz,i}(s) \\ G_{yx,i}(s) & G_{yy,i}(s) & G_{yz,i}(s) \\ G_{zx,i}(s) & G_{zy,i}(s) & G_{zz,i}(s) \end{bmatrix}_{3 \times 3}, \quad i = t, w \quad (4.33)$$

where the terms on the main diagonal correspond to the direct FRFs, and the off-diagonal terms account for the cross couplings. All the FRFs are obtained either by FE modal analysis or experimental hammer tests (see Section 5.5). Critical stability of the process is analyzed based on the most severe loading, which happens when all teeth are engaged in the cut. In this case, $g_j(t) = 1$ for all teeth, and the coefficient matrices in Eqs. (4.30)-(4.32) become constants. Hence, the total force vector calculated in Eq. (4.28) can be represented in Laplace domain as:

$$\mathbf{F}_c(s) = \mathbf{F}_s/s + [\mathbf{K}_{dc}] \mathbf{q}(s) - [\mathbf{K}_{dd}] e^{-Ts} \mathbf{q}(s) + [\mathbf{C}_p] s \mathbf{q}(s) \quad (4.34)$$

where T is the spindle period. Force \mathbf{F}_c exerted on the tool and the reaction force $-\mathbf{F}_c$ exerted on the workpiece result in the three-dimensional vibrations of the tool and workpiece:

$$\mathbf{q}_t(s) = [\mathbf{G}_t(s)]_{3 \times 3} \{\mathbf{F}_c(s)\}_{3 \times 1} \quad (4.35)$$

$$\mathbf{q}_w(s) = [\mathbf{G}_w(s)]_{3 \times 3} \{-\mathbf{F}_c(s)\}_{3 \times 1} \quad (4.36)$$

Relative vibration vector is calculated as (Eq. 4.2):

$$\mathbf{q}(s) = \mathbf{q}_t(s) - \mathbf{q}_w(s) = [\mathbf{G}(s)]_{3 \times 3} \mathbf{F}_c(s) \quad (4.37)$$

where \mathbf{G} is the relative structural dynamics between the tool and workpiece:

$$\mathbf{G}(s) = \mathbf{G}_t(s) + \mathbf{G}_w(s) \quad (4.38)$$

The closed loop equation of chip regeneration is obtained by substituting $\mathbf{F}_c(s)$ from Eq. (4.34) into Eq. (4.37):

$$\mathbf{q}(s) = \mathbf{G}(s) ([\mathbf{K}_{dc}] - [\mathbf{K}_{dd}] e^{-Ts} + [\mathbf{C}_p] s) \mathbf{q}(s) \quad (4.39)$$

where the static force \mathbf{F}_s has been dropped as it does not contribute to chip regeneration (perturbation theory). The characteristic equation of the process is therefore:

$$[\mathbf{I}_{3 \times 3} - \mathbf{G}(s) ([\mathbf{K}_{dc}] - [\mathbf{K}_{dd}] e^{-Ts} + [\mathbf{C}_p] s)]_{s=j\omega} = 0 \quad (4.40)$$

where $\mathbf{I}_{3 \times 3}$ is the identity matrix and j is the unit imaginary number. Stability of the process is analyzed in frequency domain using Nyquist criterion; for a given tool-workpiece setup, pass number, infeed settings, and spindle speed, the coefficient matrices are calculated from Eqs (4.30)-(4.32). The value of the characteristic function $\Lambda(j\omega)$,

$$\Lambda(j\omega) = \mathbf{I}_{3 \times 3} - \mathbf{G}(j\omega) ([\mathbf{K}_{dc}] - [\mathbf{K}_{dd}] e^{-Tj\omega} + [\mathbf{C}_p] j\omega) \quad (4.41)$$

is then calculated for different frequencies (ω) and plotted on the Real-Imaginary plane. Stability is determined based on the encirclement of the origin (Nyquist criterion). Sample results and numerical discussions are presented in Section 4.9.

Remarks

1. If the structural dynamics of the workpiece ($\mathbf{G}(s)$) varies along the axial direction, critical stability must be analyzed based on the most dynamically flexible point.
2. Stability analysis is performed for each pass individually; if the structural

dynamics of the workpiece changes due to material removal, the updated FRFs can be used for the next passes.

4.7 Dynamic Equation of Motion in Time Domain

In order to simulate the response of the system during the entire operation, this section sets up the dynamic model in time domain. The equations are derived in modal space since the resultant matrices are decoupled and sparse. In order to decrease the computation load, the structural dynamics of the tool and workpiece are approximated using m_t and m_w number of dominant modes, respectively. The reduced transfer functions (FRFs) of the tool and workpiece can be constructed in Laplace domain as [44]

$$\mathbf{G}_i(s) = \hat{\mathbf{U}}_i (\mathbf{I}s^2 + 2\zeta_i \omega_{n,i} s + \omega_{n,i}^2)^{-1} \hat{\mathbf{U}}_i^T, \quad i = t, w \quad (4.42)$$

where $\mathbf{I}_{[m_i \times m_i]}$ ($i = t, w$) is the identity matrix, and ζ_i and $\omega_{n,i}$ are the diagonal damping ratio and natural frequency matrices, respectively. $\hat{\mathbf{U}}_i$ ($i = t, w$) is the mass-normalized mode shape matrix of the tool and workpiece at the cutting location:

$$\hat{\mathbf{U}}_i = \left[\begin{array}{c} \left\{ \begin{array}{c} u_{x,1,i} \\ u_{y,1,i} \\ u_{z,1,i} \end{array} \right\} \quad \left\{ \begin{array}{c} u_{x,2,i} \\ u_{y,2,i} \\ u_{z,2,i} \end{array} \right\} \quad \cdots \quad \left\{ \begin{array}{c} u_{x,m_i,i} \\ u_{y,m_i,i} \\ u_{z,m_i,i} \end{array} \right\} \end{array} \right]_{3 \times m_i}, \quad i = t, w \quad (4.43)$$

where each column is a mode shape vector showing the relative displacements of the cutting point in the three directions (global XYZ) when the system vibrates in that mode. Vibrations of the tool and workpiece can be transformed to the modal space as:

$$\{\mathbf{q}_i(t)\}_{[3 \times 1]} = \{\hat{\mathbf{U}}_i\}_{[3 \times m_i]} \{\boldsymbol{\Psi}_i(t)\}_{[m_i \times 1]}, \quad i = t, w \quad (4.44)$$

where \mathbf{q}_i and $\boldsymbol{\Psi}_i$ are the displacement vectors in the physical and modal spaces, respectively. The relative vibration vector between the tool and workpiece (Eq. (4.2)) is:

$$\mathbf{q}(t) = \mathbf{q}_t(t) - \mathbf{q}_w(t) = \hat{\mathbf{U}}_t \boldsymbol{\Psi}_t(t) - \hat{\mathbf{U}}_w \boldsymbol{\Psi}_w(t) \quad (4.45)$$

Using Eq. (4.28), the total force vector is written in terms of modal displacements:

$$\begin{aligned} \mathbf{F}_c(t) = \mathbf{F}_s(t) + [\mathbf{K}_{dc}(t)] (\hat{\mathbf{U}}_t \boldsymbol{\Psi}_t(t) - \hat{\mathbf{U}}_w \boldsymbol{\Psi}_w(t)) - [\mathbf{K}_{dd}(t)] (\hat{\mathbf{U}}_t \boldsymbol{\Psi}_t(t-T) - \hat{\mathbf{U}}_w \boldsymbol{\Psi}_w(t-T)) \\ + [\mathbf{C}_p(t)] (\hat{\mathbf{U}}_t \dot{\boldsymbol{\Psi}}_t(t) - \hat{\mathbf{U}}_w \dot{\boldsymbol{\Psi}}_w(t)) \end{aligned} \quad (4.46)$$

Dynamic equations of motion for the tool and workpiece (in Laplace domain) are obtained by combining Eqs. (4.35), (4.36), (4.42), and (4.44):

$$\begin{cases} (\mathbf{I}s^2 + 2\zeta_t \omega_{n,t} s + \omega_{n,t}^2) \boldsymbol{\Psi}_t(s) = \hat{\mathbf{U}}_t^T \mathbf{F}_c(s) \\ (\mathbf{I}s^2 + 2\zeta_w \omega_{n,w} s + \omega_{n,w}^2) \boldsymbol{\Psi}_w(s) = -\hat{\mathbf{U}}_w^T \mathbf{F}_c(s) \end{cases} \quad (4.47)$$

The modal displacement vectors of the tool and workpiece are put together in a single vector

$$\boldsymbol{\Gamma}(t) = \left\{ \begin{array}{c} \boldsymbol{\Psi}_t(t) \\ \boldsymbol{\Psi}_w(t) \end{array} \right\}_{m_t+m_w}, \quad (4.48)$$

and the force expression from Eq. (4.46) is substituted into Eq. (4.47). The combined modal dynamic equation of the tool and workpiece in the time domain and in matrix form is:

$$\ddot{\boldsymbol{\Gamma}}(t) + (\mathbf{C}_{m,1} + \mathbf{C}_{m,2}(t)) \dot{\boldsymbol{\Gamma}}(t) + (\mathbf{K}_{mc,1} + \mathbf{K}_{mc,2}(t)) \boldsymbol{\Gamma}(t) + \mathbf{K}_{md}(t) \boldsymbol{\Gamma}(t-T) = \mathbf{F}_{sm}(t) \quad (4.49)$$

where

$$\begin{aligned} \mathbf{C}_{m,1} &= \begin{bmatrix} 2\zeta_t \omega_{n,t} & \mathbf{0}_{[m_t \times m_w]} \\ \mathbf{0}_{[m_w \times m_t]} & 2\zeta_w \omega_{n,w} \end{bmatrix}, & \mathbf{C}_{m,2}(t) &= - \begin{bmatrix} \hat{\mathbf{U}}_t^T \\ -\hat{\mathbf{U}}_w^T \end{bmatrix} [\mathbf{C}_p(t)] \begin{bmatrix} \hat{\mathbf{U}}_t & -\hat{\mathbf{U}}_w \end{bmatrix} \\ \mathbf{K}_{mc,1} &= \begin{bmatrix} \omega_{n,t}^2 & \mathbf{0}_{[m_t \times m_w]} \\ \mathbf{0}_{[m_w \times m_t]} & \omega_{n,w}^2 \end{bmatrix}, & \mathbf{K}_{mc,2}(t) &= - \begin{bmatrix} \hat{\mathbf{U}}_t^T \\ -\hat{\mathbf{U}}_w^T \end{bmatrix} [\mathbf{K}_{dc}(t)] \begin{bmatrix} \hat{\mathbf{U}}_t & -\hat{\mathbf{U}}_w \end{bmatrix} \\ \mathbf{K}_{md}(t) &= \begin{bmatrix} \hat{\mathbf{U}}_t^T \\ -\hat{\mathbf{U}}_w^T \end{bmatrix} [\mathbf{K}_{dd}(t)] \begin{bmatrix} \hat{\mathbf{U}}_t & -\hat{\mathbf{U}}_w \end{bmatrix} \\ \mathbf{F}_{sm}(t) &= \begin{bmatrix} \hat{\mathbf{U}}_t^T \\ -\hat{\mathbf{U}}_w^T \end{bmatrix} \mathbf{F}_s(t) \end{aligned} \quad (4.50)$$

$\mathbf{C}_{m,i}$, $\mathbf{K}_{mc,i}$ ($i=1,2$), and \mathbf{K}_{md} are square matrices of size $(m_t + m_w) \times (m_t + m_w)$, and \mathbf{C}_p , \mathbf{K}_{dc} , and \mathbf{K}_{dd} have 3×3 dimensions; mode shape matrices $\hat{\mathbf{U}}_i$, ($i = t, w$) are of size $3 \times m_i$, and $\mathbf{F}_{sm}(t)$ and $\mathbf{F}_s(t)$ are column vectors of size $(m_t + m_w) \times 1$ and 3×1 , respectively.

It is numerically more efficient to solve the equation of motion in state space. If the state vector is defined as:

$$\boldsymbol{\Omega}(t) = \left\{ \begin{array}{c} \mathbf{F}(t) \\ \dot{\mathbf{F}}(t) \end{array} \right\}_{2(m_t+m_w) \times 1}, \quad (4.51)$$

Eq. (4.49) can be transformed to state space as:

$$\dot{\boldsymbol{\Omega}}(t) = \mathbf{A}_0 \boldsymbol{\Omega}(t) + \mathbf{B}_c(t) \boldsymbol{\Omega}(t) + \mathbf{B}_d(t) \boldsymbol{\Omega}(t - T) + \mathbf{S}(t) \quad (4.52)$$

where \mathbf{A}_0 , $\mathbf{B}_c(t)$, and $\mathbf{B}_d(t)$ are the constant, current, and delayed state matrices (each of size $2(m_t + m_w) \times 2(m_t + m_w)$), respectively, and column vector $\mathbf{S}(t)$ is the piecewise¹ static forcing function (length $2(m_t + m_w)$):

$$\begin{aligned} \mathbf{A}_0 &= \begin{bmatrix} \mathbf{0} & \mathbf{I} \\ -\mathbf{K}_{mc,1} & -\mathbf{C}_{m,1} \end{bmatrix}, & \mathbf{B}_c(t) &= \begin{bmatrix} \mathbf{0} & \mathbf{0} \\ -\mathbf{K}_{mc,2}(t) & -\mathbf{C}_{m,2}(t) \end{bmatrix} \\ \mathbf{B}_d(t) &= \begin{bmatrix} \mathbf{0} & \mathbf{0} \\ -\mathbf{K}_{md}(t) & \mathbf{0} \end{bmatrix}, & \mathbf{S}_t(t) &= \begin{bmatrix} \{\mathbf{0}\}_{[(m_t+m_w) \times 1]} \\ \{\mathbf{F}_{sm}(t)\}_{[(m_t+m_w) \times 1]} \end{bmatrix} \end{aligned} \quad (4.53)$$

where all the $\mathbf{0}$ and \mathbf{I} entries are of size $(m_t + m_w) \times (m_t + m_w)$, and the other entries are defined in Eq. (4.50). Since the static force ($\mathbf{S}(t)$) has been included, the solution of Eq. (4.52) consists of the vibrations as well as the static deflections of the tool and workpiece. Hence, the time domain solution allows us to predict not only the stability of the process but also the accuracy and surface location errors in the machined threads.

4.8 Time-Marching Numerical Simulation

In order to simulate the full time history of the process, this section presents a time-marching numerical method to solve Eq. (4.52) consecutively at each time step. Semi-discretization technique proposed by Insperger and Stepan [20] is combined

¹Due to the transient condition at the beginning of the process.

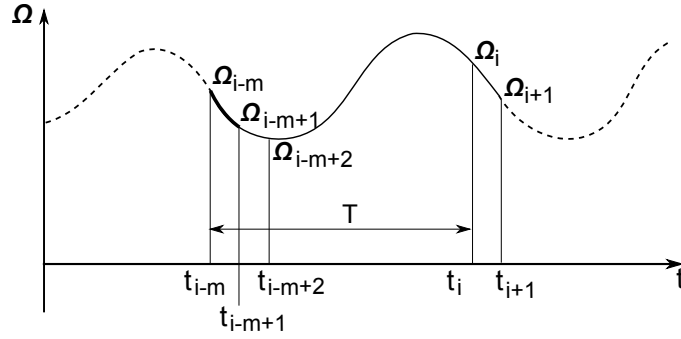


Figure 4.5: Semi-discretization of delay differential equations [20].

with the Simpson's three-point integration rule to numerically evolve the solution over time. As demonstrated in Figure 4.5, each spindle revolution (period T) is divided into m intervals of $\Delta t = T/m$. In each time interval $t_0 < t < t_0 + \Delta t$, the last three terms in Eq. (4.52) are approximated by their values at $t = t_0$. The delay differential equation (DDE) then turns into an ordinary differential equation (ODE) over the interval, the solution of which can be obtained analytically. Since \mathbf{A}_0 is a time-invariant matrix, the solution to the ODE in the current interval can be written as [40]:

$$\begin{aligned}\boldsymbol{\Omega}(t) &= e^{\mathbf{A}_0(t-t_0)} \boldsymbol{\Omega}(t_0) + \int_{t_0}^t e^{\mathbf{A}_0(t-\tau)} \mathbf{H}(\tau) d\tau \\ \mathbf{H}(\tau) &= \mathbf{B}_c(\tau) \boldsymbol{\Omega}(\tau) + \mathbf{B}_d(\tau) \boldsymbol{\Omega}(\tau - T) + \mathbf{S}(\tau)\end{aligned}\quad (4.54)$$

where $\boldsymbol{\Omega}(t_0)$ is the state value at initial time t_0 . The integral in Eq. (4.54) is approximated using Simpson's integration rule; at each time step $t_i = t_0 + (i-1)\Delta t$, ($i = 2, 3, \dots$), the state value $\boldsymbol{\Omega}(t_i)$ is obtained from the available function values \mathbf{H} at three integration points (t_{i-2}, t_{i-1}, t_i):

$$\begin{aligned}\boldsymbol{\Omega}(t_i) &= e^{\mathbf{A}_0(t_i-t_{i-2})} \boldsymbol{\Omega}(t_{i-2}) + \int_{t_{i-2}}^{t_i} e^{\mathbf{A}_0(t_i-\tau)} \mathbf{H}(\tau) d\tau \\ &= e^{2\mathbf{A}_0\Delta t} \boldsymbol{\Omega}(t_{i-2}) + \frac{(2\Delta t)}{6} \left\{ e^{2\mathbf{A}_0\Delta t} \mathbf{H}(t_{i-2}) + 4e^{\mathbf{A}_0\Delta t} \mathbf{H}(t_{i-1}) + \mathbf{H}(t_i) \right\}\end{aligned}\quad (4.55)$$

Equation (4.55) is an implicit relation since $\mathbf{H}(t_i)$ requires the value $\boldsymbol{\Omega}(t_i)$ (Eq. 4.54). If all the \mathbf{H} functions in Eq. (4.55) are expanded using Eq. (4.54), $\boldsymbol{\Omega}(t_i)$ can be

obtained explicitly as:

$$\begin{aligned}
 \boldsymbol{\Omega}(t_i) = & \left(\mathbf{I} - \frac{\Delta t}{3} \mathbf{B}_c(t_i) \right)^{-1} \left[e^{2\mathbf{A}_0\Delta t} \boldsymbol{\Omega}(t_{i-2}) \right. \\
 & + \frac{\Delta t}{3} e^{2\mathbf{A}_0\Delta t} \{ \mathbf{B}_c(t_{i-2}) \boldsymbol{\Omega}(t_{i-2}) + \mathbf{B}_d(t_{i-2}) \boldsymbol{\Omega}(t_{i-2-m}) + \mathbf{S}(t_{i-2}) \} \\
 & + \frac{4\Delta t}{3} e^{\mathbf{A}_0\Delta t} \{ \mathbf{B}_c(t_{i-1}) \boldsymbol{\Omega}(t_{i-1}) + \mathbf{B}_d(t_{i-1}) \boldsymbol{\Omega}(t_{i-1-m}) + \mathbf{S}(t_{i-1}) \} \\
 & \left. + \frac{\Delta t}{3} \{ \mathbf{B}_d(t_i) \boldsymbol{\Omega}(t_{i-m}) + \mathbf{S}(t_i) \} \right] \quad (4.56)
 \end{aligned}$$

where $m = T/\Delta t$ is the number of time steps in one spindle revolution, and \mathbf{I} is the identity matrix of size $2(m_t + m_w) \times 2(m_t + m_w)$. For simulation of the first spindle revolution, all the delay states (initial conditions) are assumed to be zero, i.e.

$$\forall i, 0 \leq i \leq m-1 : \quad \boldsymbol{\Omega}(t_{i-m}) = \{\mathbf{0}\}_{[2(m_t+m_w) \times 1]} \quad (4.57)$$

Equation (4.56) cannot be used for calculation of $\boldsymbol{\Omega}(t_1)$ since coefficient matrices are not defined at $t < 0$. The time-marching simulation is initialized by calculating a dummy state $\boldsymbol{\Omega}(t_0 + \Delta t/2)$ using two-point trapezoidal integration:

$$\boldsymbol{\Omega}(t_0 + \frac{\Delta t}{2}) = e^{\mathbf{A}_0\Delta t/2} \boldsymbol{\Omega}(t_0) + \frac{(\Delta t/2)}{2} \left\{ e^{\mathbf{A}_0\Delta t/2} \mathbf{H}(t_0) + \mathbf{H}(t_0 + \frac{\Delta t}{2}) \right\}, \quad (4.58)$$

which along with Eq. (4.57) leads to the following explicit expression:

$$\begin{aligned}
 \boldsymbol{\Omega}(t_0 + \frac{\Delta t}{2}) = & \left(\mathbf{I} - \frac{\Delta t}{4} \mathbf{B}_c(t_0 + \frac{\Delta t}{2}) \right)^{-1} \left[e^{\mathbf{A}_0\Delta t/2} \boldsymbol{\Omega}(t_0) \right. \\
 & \left. + \frac{\Delta t}{4} e^{\mathbf{A}_0\Delta t/2} \{ \mathbf{B}_c(t_0) \boldsymbol{\Omega}(t_0) + \mathbf{S}(t_0) \} + \frac{\Delta t}{4} \left\{ \mathbf{S}(t_0 + \frac{\Delta t}{2}) \right\} \right] \quad (4.59)
 \end{aligned}$$

$\boldsymbol{\Omega}(t_1)$ is then calculated by three-point Simpsons rule using the function values at times t_0 , $t_0 + \Delta t/2$, and t_1 :

$$\boldsymbol{\Omega}(t_1) = e^{\mathbf{A}_0\Delta t} \boldsymbol{\Omega}(t_0) + \frac{\Delta t}{6} \{ e^{\mathbf{A}_0\Delta t} \mathbf{H}(t_0) + 4e^{\mathbf{A}_0\Delta t/2} \mathbf{H}(t_0 + \frac{\Delta t}{2}) + \mathbf{H}(t_1) \} \quad (4.60)$$

or in explicit form:

$$\begin{aligned} \boldsymbol{\Omega}(t_1) = & \left(\mathbf{I} - \frac{\Delta t}{6} \mathbf{B}_c(t_1) \right)^{-1} \left[e^{\mathbf{A}_0 \Delta t} \boldsymbol{\Omega}(t_0) + \frac{\Delta t}{6} e^{\mathbf{A}_0 \Delta t} \{ \mathbf{B}_c(t_0) \boldsymbol{\Omega}(t_0) + \mathbf{S}(t_0) \} \right. \\ & \left. + \frac{4\Delta t}{6} e^{\mathbf{A}_0 \Delta t / 2} \left\{ \mathbf{B}_c(t_0 + \frac{\Delta t}{2}) \boldsymbol{\Omega}(t_0 + \frac{\Delta t}{2}) + \mathbf{S}(t_0 + \frac{\Delta t}{2}) \right\} + \frac{\Delta t}{6} \{ \mathbf{S}(t_1) \} \right] \end{aligned} \quad (4.61)$$

Once the state vector $\boldsymbol{\Omega}(t_i)$ is calculated, the vibration vector of the tool and work-piece can be extracted from Eqs. (4.44), (4.48), and (4.51). The resultant forces at each time step are simulated using Eq. (4.28).

Remark. The time domain solution can be used to determine the stability of the process by simulating the vibrations. It is important to ensure that instability of the predicted vibrations is due to the instability of the process and not the numerical method. In this thesis, the minimum required time discretization for numerical stability has been found by trial and error, but the stability region can be found analytically using advanced theories of numerical methods.

Comparison With Euler Solution

In order to examine the efficiency and stability of the presented numerical method, the equation of motion (Eq. (4.49)) has been solved using Euler numerical method as well. If the derivative terms are approximated as:

$$\ddot{\boldsymbol{\Gamma}}(t_i) = \frac{\boldsymbol{\Gamma}(t_{i+2}) - 2\boldsymbol{\Gamma}(t_{i+1}) + \boldsymbol{\Gamma}(t_i)}{\Delta t^2} \quad (4.62)$$

$$\dot{\boldsymbol{\Gamma}}(t_i) = \frac{\boldsymbol{\Gamma}(t_{i+1}) - \boldsymbol{\Gamma}(t_i)}{\Delta t}, \quad (4.63)$$

and substituted in Eq. (4.49), the explicit time-marching expression for the state vector is obtained as:

$$\boldsymbol{\Gamma}(t_{i+2}) = \mathbf{E}_3 \boldsymbol{\Gamma}(t_{i+1}) + \mathbf{E}_2 \boldsymbol{\Gamma}(t_i) + \mathbf{E}_1 \boldsymbol{\Gamma}(t_{i-m}) + \mathbf{E}_0 \quad (4.64)$$

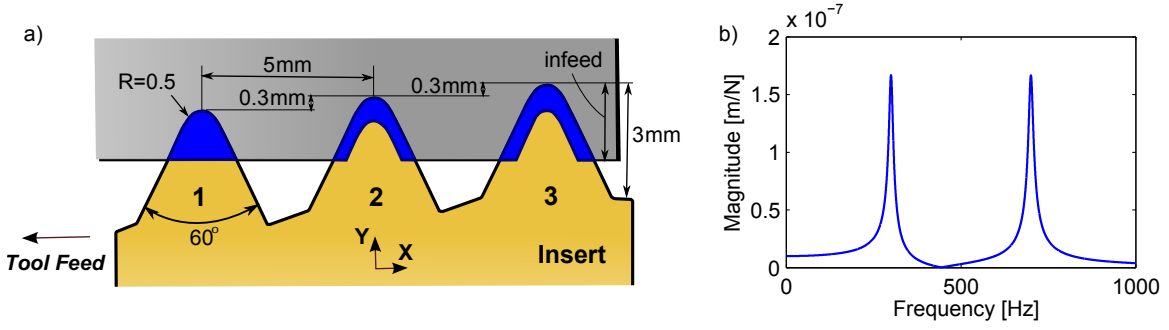


Figure 4.6: Simulation setup: a) sample multi-point V-profile insert, b) FRF of the workpiece in the radial direction.

where

$$\begin{cases} \mathbf{E}_3 = 2\mathbf{I} - \Delta t(\mathbf{C}_{m,1} + \mathbf{C}_{m,2}(t_i)) \\ \mathbf{E}_2 = -\mathbf{I} + \Delta t(\mathbf{C}_{m,1} + \mathbf{C}_{m,2}(t_i)) - \Delta t^2(\mathbf{K}_{mc,1} + \mathbf{K}_{mc,2}(t_i)) \\ \mathbf{E}_1 = -\Delta t^2 \mathbf{K}_{md}(t_i) \\ \mathbf{E}_0 = \Delta t^2 \mathbf{F}_{sm}(t_i) \end{cases} \quad (4.65)$$

All the initial conditions are assumed to be zero.

4.8.1 Remarks: Cutter Disengagement Due to Large Vibrations

In the case of large vibrations, one or more teeth can disengage from the workpiece for part of the vibration cycle. At each time t_i , if the vibrations separating the tool and workpiece are larger than the chip thickness on tooth j , the boolean function $g_j(t_i)$ (Eq. (4.26)) is set to zero until the tooth comes back in the cut. In the case when all teeth jump out of cut, all the forcing coefficients in Eq. (4.50) become zero except the structural matrices $\mathbf{C}_{m,1}$ and $\mathbf{K}_{mc,1}$. In this case, both the tool and workpiece undergo free vibration state until they engage again. A sample simulation involving out-of-cut jumps is presented in the next section (Figure 4.7.e).

4.9 Sample Simulation Results and Discussions

This section highlights important technical and numerical remarks in modelling and simulation of multi-point threading operations. A sample V-profile insert shown in Figure 4.6.a has been used for the simulations. The pitch of the thread is 5 mm, and all passes are performed at 1850 rpm spindle speed. The workpiece material

Table 4.1: Dynamic parameters of the workpiece used in simulations.

	ω_n [Hz]	ζ	k_s [N/m]
Mode 1	300	2%	1.5×10^8
Mode 2	700	1%	3.0×10^8

is AISI1045 steel with cutting force coefficients identified in Section 3.7.1. The indentation coefficient used in the process damping model is $K_{sp} = 4 \times 10^{13}$ N/m³. As shown in Figure 4.6.b, it is assumed that the structural dynamics of the workpiece is dominated by two modes in the radial direction. Table 4.1 provides the dynamic parameters for these two modes.

Nyquist criterion in frequency domain has been used to analyze the stability of the process for each pair of infeed value (Δa) and spindle speed (n). Figure 4.7.a shows the predicted stability chart for the first pass, where the area below the lobes represent the stable region. In order to capture the shape of the lobes with more details, a grid of 100 infeed values and 500 spindle speeds has been used. On a PC with i5 core and 3.10 GHz CPU, it takes about 10 minutes to generate this chart with such a dense grid (50,000 points). In practice, however, the absolute stability limits can be detected reliably in less 30 seconds using a coarser grid.

In order to verify the frequency domain stability chart in Figure 4.7.a, the time-marching numerical method presented in Section 4.8 has been used to simulate the relative displacement between the tool and workpiece over 50 spindle revolutions. Figures 4.7.b-d show the results for three infeed values close to the stability limit at 1850 rpm spindle speed. It can be seen that the point below the lobes (1.6 mm, 1850 rpm) results in decaying vibrations while the point above (2.0 mm, 1850 rpm) leads to instability. The process is marginally stable at (1.8 mm, 1850 rpm), which fully agrees with the frequency domain lobes. Figure 4.7.e shows the system response to an aggressive infeed of 3 mm. Even though the process is unstable, the vibrations cannot grow indefinitely due to cutter disengagement (Section 4.8.1).

It can be observed in Figure 4.7.b that in addition to the high frequency vibrations, there is a 0.02 mm average offset in the simulated displacements. This is due to the static deflection of the workpiece under the cutting forces, and results in undercutting the thread profile over the current pass. The uncut material adds to the chip load and cutting forces in the following pass; the static deflections over

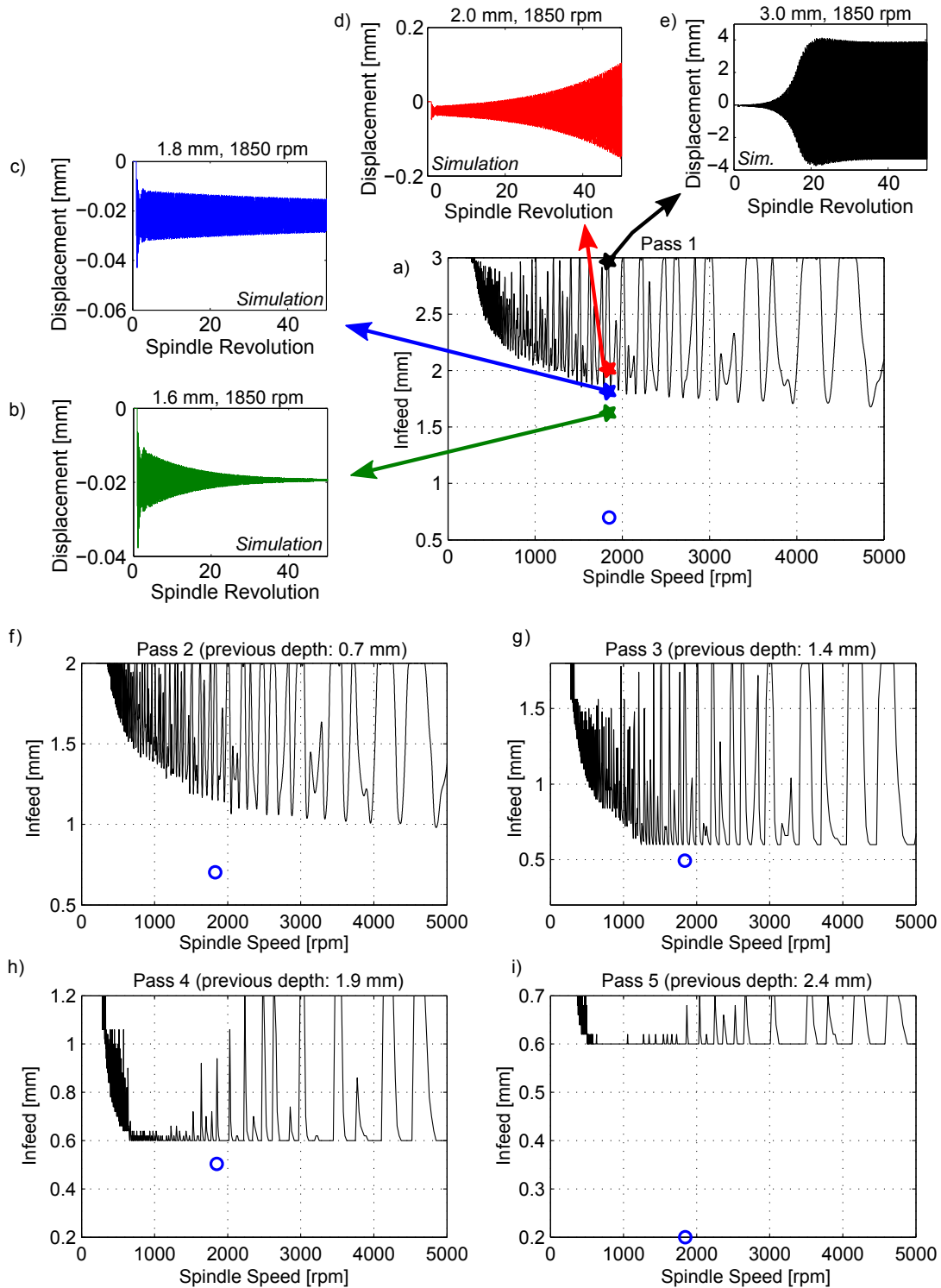


Figure 4.7: Stability charts and time simulations for threading with three-point V-profile insert (material: AISI 1045).

the final pass directly translates to defects and inaccuracy in the thread profile. In practice, the infeed value over the final pass is chosen relatively small to reduce these errors.

Stability over each pass depends on the previous thread depth. As marked by small circles in Figures 4.7.a and f, assume that the infeeds for both the first and second passes are chosen as 0.7 mm (to avoid large cutting forces). The stability charts for the third and fourth passes are shown in Figures 4.7.g and h, respectively. The absolute stability limit at 1850 rpm is only 0.6 mm, which means cutting with only two teeth (#2 and #3); engaging tooth #1 leads to instability for any infeed value. Considering a safety margin, the infeeds for both third and fourth passes are chosen as 0.5 mm. Assume that the desired final depth for this application is 2.6 mm. Figure 4.7.i shows the stability chart for the final pass with the previous depth of 2.4 mm. The final infeed is thus 0.2 mm, which leads to cutting with only tooth #3.

4.10 Numerical Remarks

4.10.1 Efficiency of Time-marching Numerical Methods

Semi-discretization and Euler's methods (Section 4.8) have been used to simulate the stable point (1.6 mm, 1850 rpm) in Figure 4.7.b over 50 spindle revolutions. The two methods have been compared based on two criteria:

1. *Stability*: Minimum number of discretization intervals m (per spindle revolution) required to correctly predict the stability of the threading process.
2. *Convergence*: Minimum number m such that further increase in m does not change the amplitudes and shape of the simulated vibrations considerably.

Table 4.2 summarizes the comparison results, and the simulated vibrations are shown in Figure 4.8. It can be seen that SD method is stable with $m = 70$ while Euler's method requires at least $m = 57,000$. For convergence, SD method requires $m = 115$ and can simulate the process over 50 spindle revolutions in 0.06 seconds. Euler's method, on the other hand, requires at least $m = 230,000$ and 35 seconds to simulate the same process. This is due to the fact that SD technique solves

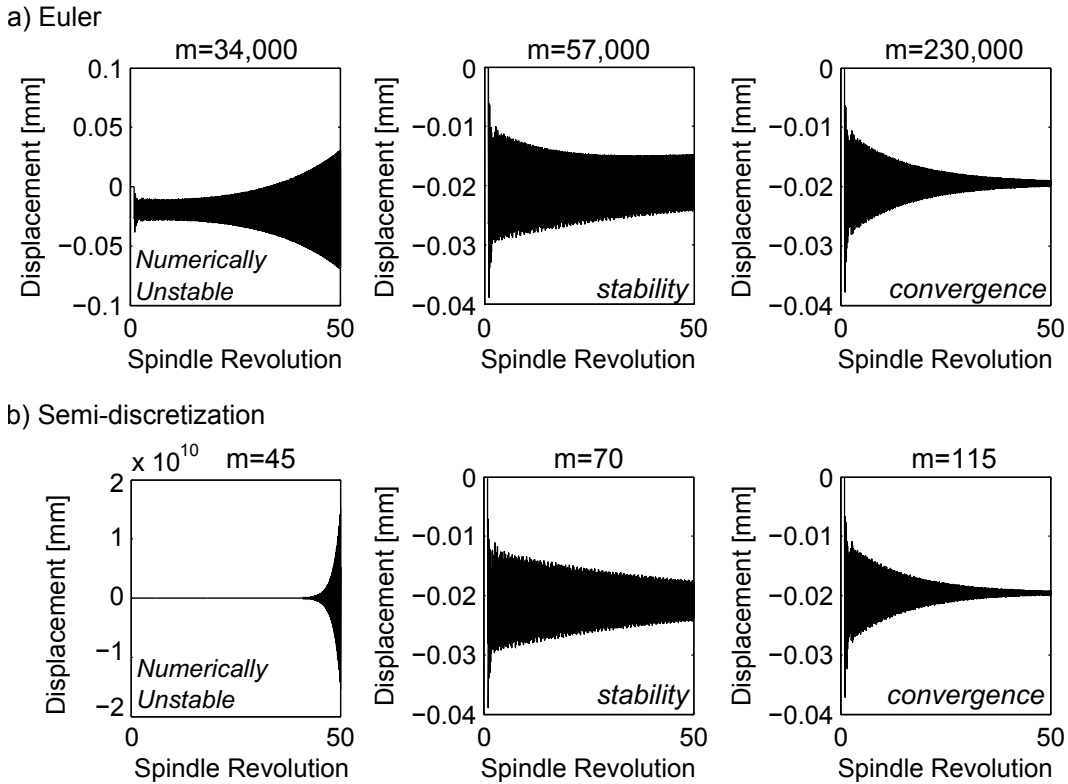


Figure 4.8: Comparison of Semi-discretization and Euler's methods for time-marching numerical simulation (structural frequencies: 300 Hz and 700 Hz, spindle speed: 1850 rpm, infeed: 1.6 mm).

Table 4.2: Minimum discretization intervals for stability and convergence of time-marching simulations.

	Stability m	Convergence m	Simulation Time (50 rev, convergence)
Semi-discretization	70	115	0.06 s
Euler's method	57,000	230,000	35 s

the approximated ODEs analytically in each time step while Euler's method solves algebraic equations by approximating all the derivative terms numerically.

In conclusion, not only SD method is faster than Euler discretization (by a factor of 500 in this example) but also it requires significantly less memory due to smaller number of time steps.

Remark 1. Since the presented numerical method in Section 4.8 is used to determine the instability of the machining process, it is important to ensure that the

numerical method itself is not unstable. Hartung et al. [80] proved mathematically that there exist a minimum discretization number (m) which guarantees the stability and convergence of the semi-discretization method. The minimum m depends on the process parameters and cannot be determined analytically. The suggested approach is to first simulate the vibrations for low infeed values where the process is stable, find the minimum discretization number for stability of the numerical method, and then generate the stability charts.

Remark 2. Sensitivity of the predicted stability lobes (Figure 4.7.a, three-point V-profile insert) to the discretization number m is analyzed in Figure 4.9. The 'ex-

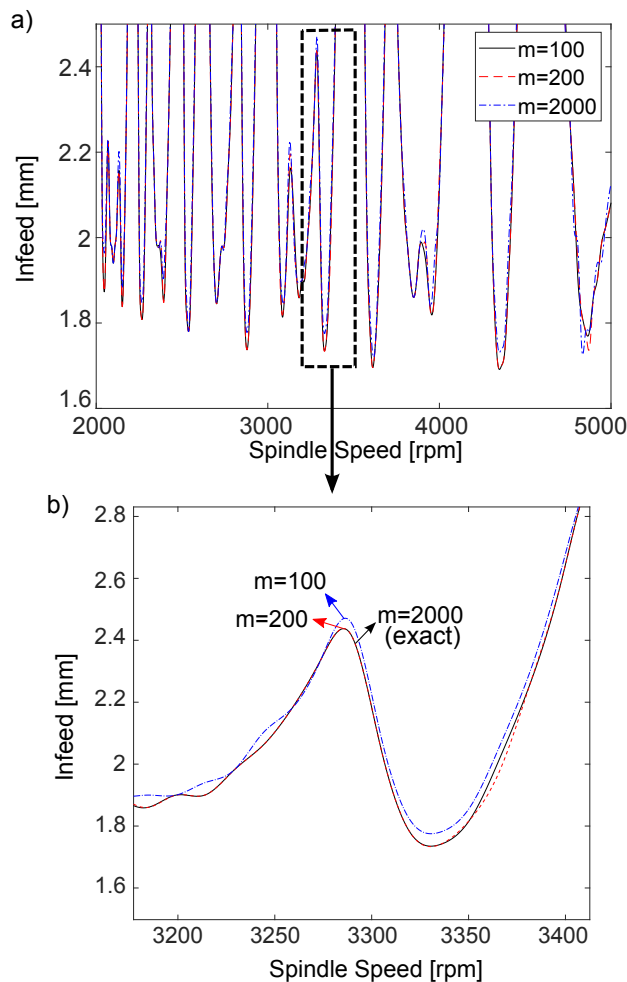


Figure 4.9: Sensitivity of the stability lobes to numerical semi-discretization, a) stability lobes for the three-point V-profile insert, material: AISI 1045, b) comparison for different number of discretization m .

act' stability chart has been generated using $m = 2000$ points. The stability charts for $m = 100$ and $m = 200$ are also shown in Figure 4.9. It can be seen that while there is a slight difference between the exact solution and the lobes for the case with $m = 100$, using $m = 200$ gives nearly identical stability lobes as $m = 2000$. Therefore, using $m > 200$ has no practical effect on the predicted stability charts in this operation.

4.10.2 Frequency Resolution in Nyquist Stability Analysis

As presented in Section 4.6, stability of the process is analyzed by plotting $\Lambda(j\omega)$, (repeated from Eq. 4.41)

$$\Lambda(j\omega) = \mathbf{I}_{3 \times 3} - \mathbf{G}(j\omega) ([\mathbf{K}_{dc}] - [\mathbf{K}_{dd}]e^{-Tj\omega} + [\mathbf{C}_p]j\omega) \quad (4.66)$$

for $\omega \in (\omega_1 : \Delta\omega : \omega_2)$, where $\Delta\omega$ is the frequency resolution (increment). If $\Delta\omega$ is not sufficiently small, Nyquist criterion may lead to false stability prediction. To demonstrate this, consider a sample point (3 mm, 1500 rpm) in Figure 4.7.a. Figure 4.10.a shows $\Lambda(j\omega)$ for ω in the range of 0-1000 Hz with 0.1 Hz increments. It can be seen that $\Lambda(j\omega)$ forms a spiral shape with varying diameter; the circling is mostly due to the phase contribution of the complex exponential term

$$e^{-Tj\omega} = \cos T\omega - j \sin T\omega, \quad (4.67)$$

which has a periodic frequency equal to the spindle frequency

$$\omega_{sp} = \frac{2\pi}{T} \quad (4.68)$$

where T is the spindle period. This means that as ω is swept over the range of frequencies, $\Lambda(j\omega)$ completes a full circle over each spindle frequency. The diameters of the circles are mainly determined by the FRF of the structure ($\mathbf{G}(j\omega)$) at each frequency. The bigger circles, which determine the stability of the process, are formed as ω approaches the resonance of the structure. It is therefore crucial that the swept frequencies include all the dominant structural modes.

Figure 4.10.b and c show the plotted $\Lambda(j\omega)$ for the same range of frequencies but with resolutions of 2 Hz and 5 Hz, respectively. It can be seen that despite the undulations, the plot with $\Delta\omega = 2$ Hz still encircles the origin, thus correctly

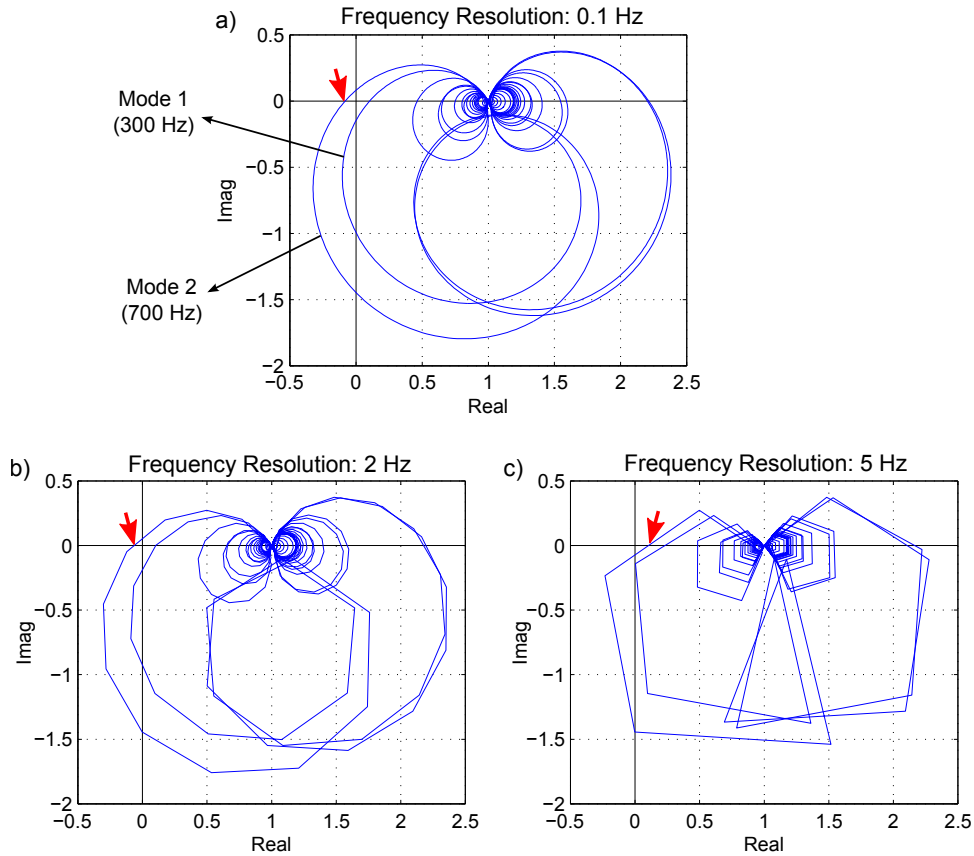


Figure 4.10: Nyquist plots with different frequency resolutions (structural frequencies: 300 Hz and 700 Hz, spindle speed: 1500 rpm, infeed: 3 mm).

implies instability. However, if 5 Hz resolution is used (Figure 4.10.c), $\Lambda(j\omega)$ no longer crosses the negative side of the imaginary axis, and the process is falsely predicted as stable.

In order to capture the shape of the circles reliably, at least 10 to 20 data points are required along each circle. Hence, the frequency resolution must be smaller than

$$\Delta\omega_{max} = \frac{\omega_{sp}}{10} = \frac{2\pi/T}{10} \quad (4.69)$$

where T is the spindle period. If the measured FRF of the structure has been recorded with a coarser resolution, it must be numerically interpolated before using Nyquist analysis. In the presented example with spindle speed of 1500 rpm, $\omega_{sp} = 157 \text{ rad/s} = 25 \text{ Hz}$, thus $\Delta\omega_{max} = 2.5 \text{ Hz}$. In analyzing low speed threading of oil pipes (120 rpm), the frequency resolution has to be as low as 0.2 Hz.

4.11 Process Optimization

One of the main capabilities of the integrated systematic model developed in this thesis is that not only can it simulate the process for a given condition, but also it can work backwards and help with process planning. An iterative optimization engine has been developed to automatically determine the number of passes and infeed values for maximum productivity while respecting user-defined constraints. For a given tool-workpiece setup, the operator selects the desired final thread depth and the cutting speed. The following practical constraints can be imposed:

- Minimum chip thickness: to avoid severe ploughing
- Maximum chip thickness: to avoid chip evacuation issues
- Tangential force on tooth: to avoid tooth breakage
- Radial force: to limit workpiece deflections
- Axial force: to avoid pulling the workpiece out of the chuck
- Spindle torque/power: to avoid machine stall
- Stability margin: e.g. 20% below the marginal stability limit

The optimization module uses a binary search algorithm to find the maximum infeed which satisfies the defined constraints. Optimization starts with the first pass, and for the first iteration, the lower and upper limits are set equal to the minimum and maximum allowed infeed values, respectively. The resultant chip thickness, forces, torque, and power are then calculated for the upper limit. If any of these outputs violate the constraints, the solution is rejected, and the upper limit is updated to the average of the previous lower and upper limits. The search continues until the size of the search window is smaller than few microns. Considering the typical infeed values in threading (smaller than 1 mm), the solution can always be found in less than 10 iterations ($2^{10} > 1000$). The converged value for the infeed is then compared to the predicted stability limit (at the desired spindle speed) in the current pass. If it is unstable, the stability limit (minus the user-defined margin) must be chosen as the optimized infeed. After the first pass, new passes are added and optimized one by one until the desired thread depth is reached.

Table 4.3: Optimization constraints for the case study with three-point V-profile insert (material: AISI 1045).

Chip Thickness		Forces			Spindle		Stability
Min	Max	Axial	Radial	Tangential	Torque	Power	Margin
0.04 mm	0.3 mm	1000 N	2000 N	5000 N	80 Nm	20 KW	20%

Table 4.4: Optimization results and the limiting factors (material: AISI 1045, insert: three-point V-profile).

	Pass 1	Pass 2	Pass 3	Pass 4
Selected Infeed	0.9 mm	0.8 mm	0.48 mm	0.42 mm
Limiting Factor	Max Chip Thickness	Max Torque	Stability	Final Depth

The case study presented in Section 4.9 (Figure 4.6) has been optimized to achieve final thread depth of 2.6 mm subject to the constraints defined in Table 4.3. The selected infeed values and their corresponding limiting factors are provided in Table 4.4. Figure 4.11 shows the calculated values and stability charts for the optimized process. As marked by LF1 in Figure 4.11.a, the first pass has been limited by the maximum allowed chip thickness (0.3 mm), resulting in total infeed of 0.9 mm. The second pass has been capped at infeed of 0.8 mm based on the maximum spindle torque (Figure 4.11.e). For the third pass, stability is the limiting factor; based on Figure 4.11.i, infeed values up to 0.6 mm are stable. Considering the required 20% stability margin, the infeed for the third pass has been determined as 0.48 mm. Finally, the desired thread depth can be achieved over the fourth pass using infeed of 0.42 mm, which satisfies all the constraints. On a PC with i5 core and 3.10 GHz CPU, optimization of each pass takes less than 10 seconds.

4.12 Summary

This chapter studies the dynamics and stability of multi-point thread turning operations. Chip regeneration model for custom multi-point inserts has been developed by studying the effect of current and previous vibrations. Dynamic cutting forces and process damping forces have been calculated by projecting the vibrations in the direction of local thickness at each point along the cutting edge. Dynamic equation of motion has been derived in the time and frequency domains, and stability of the

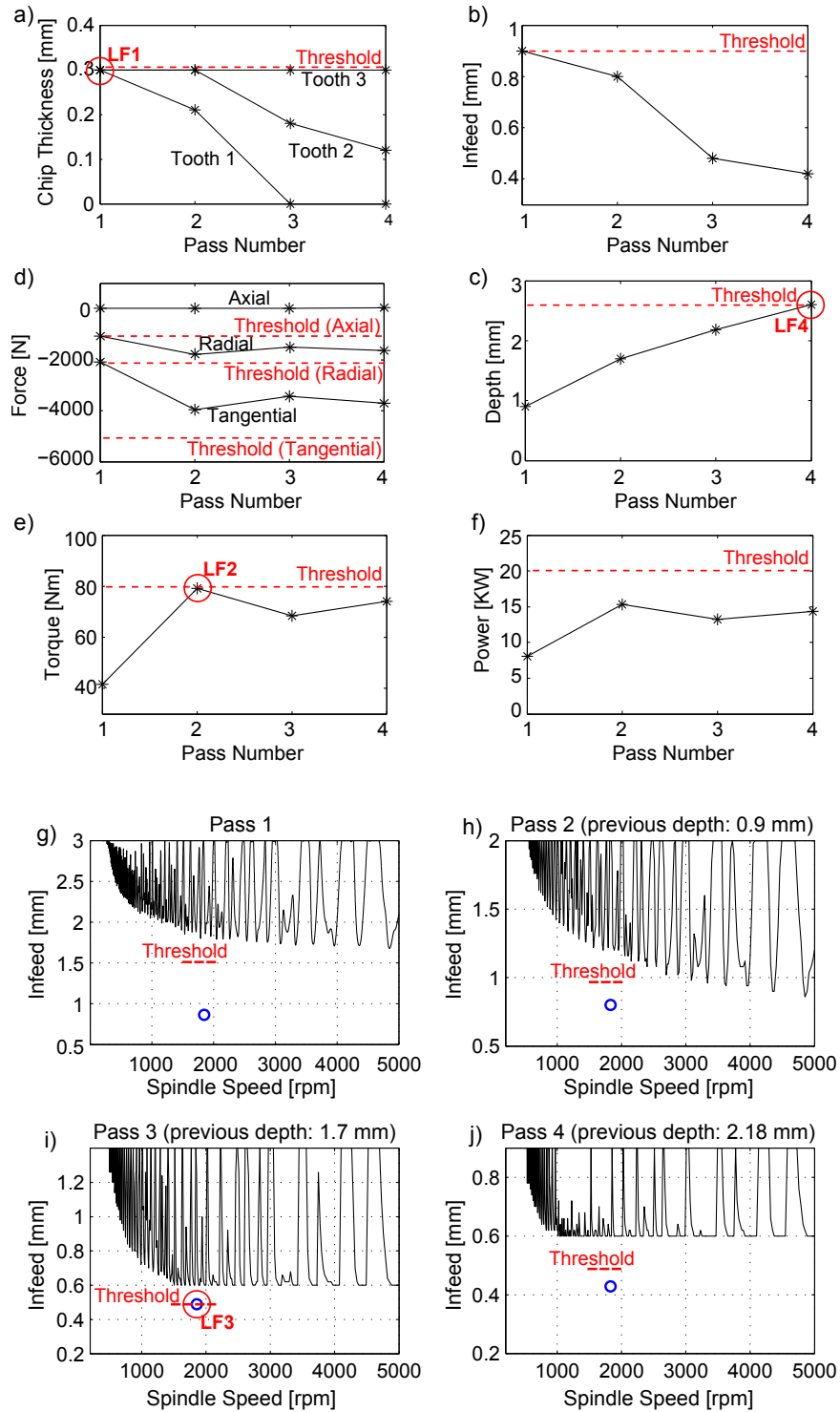


Figure 4.11: Simulated results for the optimized plan (material: AISI 1045, insert: three-point V-profile).

process is predicted using Nyquist criterion. A time-marching numerical method has been presented to simulate the process during the entire operation. Finally, the developed models have been implemented in an optimization engine to maximize productivity while respecting user-defined constraints.

Chapter 5

Threading Thin-Walled Oil Pipes

5.1 Overview

This chapter extends the dynamic model developed in Chapter 4 to threading thin-walled workpieces. Structural dynamics of clamped cylindrical shells are briefly discussed in Section 5.2, and the dynamic equation of motion for thin-wall threading is derived in Section 5.3. The remainder of the chapter is dedicated to experimental validation of the proposed dynamic model. Extensive threading tests have been conducted on real scale oil pipes in TenarisTAMSA, Veracruz, Mexico¹. The experimental setup is first introduced in Section 5.4, followed by finite element and experimental modal analysis of the pipes in Section 5.5. Sample chatter experiments are presented and compared against simulations in Section 5.6. Section 5.7 presents approaches for chatter suppression, and the developed threading simulation engine is presented in Section 5.8. The chapter is summarized in Section 5.9.

5.2 Structural Dynamics of Cylindrical Shells

Figure 5.1 illustrates different vibration modes associated with a clamped cylindrical workpiece. The dominant vibration pattern depends on the ratio of the diame-

¹Process planning, measurements and analyses have been carried out by the author during his industrial visit in August 2016.

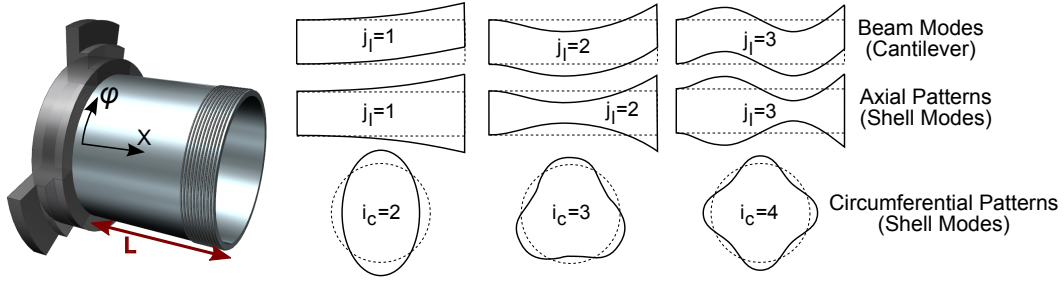


Figure 5.1: Vibration modes of a clamped thin-walled workpiece.

ter (d_w) to wall thickness (t_w) as [81]:

$$\frac{d_w}{t_w} \begin{cases} < 5 & \rightarrow \text{beam mode} \\ > 60 & \rightarrow \text{shell mode} \\ \approx 30 & \rightarrow \text{beam + shell} \end{cases} \quad (5.1)$$

For a cylindrical shell with the length of L , the instantaneous radial vibration at each point on the workpiece surface can be written in general form as [65]:

$$q_r(x, \varphi, t) = \sum_{j_l=1}^{\infty} \sum_{i_c=2}^{\infty} A_{j_l, i_c}(t) \cos(i_c \varphi) \sin(j_l \frac{x}{L} \pi + \theta_{j_l}) + \sum_{j_l=1}^{\infty} \sum_{i_c=2}^{\infty} B_{j_l, i_c}(t) \sin(i_c \varphi) \sin(j_l \frac{x}{L} \pi + \theta_{j_l}) \quad (5.2)$$

where t denotes time, and $0 \leq x \leq L$ and $0 \leq \varphi \leq 2\pi$ are the axial and circumferential coordinates of the point, respectively (Figure 5.1); $i_c = 2, 3, \dots$ is the number of waves (lobes) in the circumferential pattern, and $j_l = 1, 2, \dots$ is the number of half-waves in the axial pattern. A_{j_l, i_c} , B_{j_l, i_c} , and θ_{j_l} are determined from the boundary conditions.

Dynamic response of thin-walled workpieces during machining operation is discussed in the following section.

5.3 Response of Cylindrical Shells to Threading Loads

The dynamic threading model developed in Chapter 4 is based on the assumption that the workpiece behaves as a cantilever beam. The model is extended in this section to threading thin-walled workpieces by addressing the following two main differences:

- In machining cylindrical shells, radial flexibilities of the workpiece are the most dominant source of regenerative vibrations. All other flexibilities can be neglected.
- Due to the low-damped shell mode patterns, cutting forces result in different vibration amplitudes around the circumference of the workpiece. These residual vibrations affect the chip thickness when the corresponding point arrives in the cutting region. In order to model the process, instantaneous vibrations at all points must be determined.

The dynamic model presented below evaluates the shell vibrations in each cross section individually based on the local structural dynamics.

5.3.1 Dynamic Equation of Motion

As illustrated in Figure 5.2, assume that the circumference of the workpiece is discretized by m number of points. The instantaneous radial vibration at each point k is denoted by scalar $q_k(t)$ ($k = 1, 2, \dots, m$), where outward vibrations are considered positive. The generalized radial vibration vector $\mathbf{Q}_r(t)$ is formed by stacking all the point vibrations:

$$\mathbf{Q}_r(t) = \begin{Bmatrix} q_1(t) \\ q_2(t) \\ \vdots \\ q_m(t) \end{Bmatrix}_{[m \times 1]} \quad (5.3)$$

At each time t , the radial vibration at the cutting point can be obtained as:

$$q_{cr}(t) = \mathbf{N}_c(t) \mathbf{Q}_r(t) \quad (5.4)$$

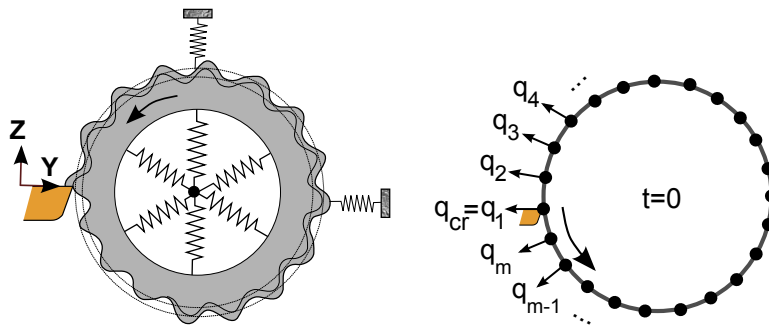


Figure 5.2: Response of cylindrical shells to machining loads.

where the row vector $\{\mathbf{N}_c(t)\}_{[1 \times m]}$ is the instantaneous shape function at the cutting point. All entries of $\mathbf{N}_c(t)$ are zero except for the entry corresponding to the point in the cutting zone, which is set to one. If necessary, higher order continuity can be achieved by interpolating (weighted average) over few points around the cutting region. Based on the defined tool coordinate system shown in Figure 5.2 (same in previous chapters), the three-dimensional vibration vector of the workpiece at the cutting location can be represented as:

$$\mathbf{q}_w(t) = \begin{Bmatrix} 0 \\ -q_{cr}(t) \\ 0 \end{Bmatrix} \quad (5.5)$$

Since the tool is considered rigid, $\mathbf{q}_t(t) = \{0, 0, 0\}^T$. The three-dimensional relative vibration vector between the tool and workpiece is (Eq. 4.2):

$$\mathbf{q}(t) = \mathbf{q}_t(t) - \mathbf{q}_w(t) = \begin{Bmatrix} 0 \\ q_{cr}(t) \\ 0 \end{Bmatrix} = \mathbf{e}_r q_{cr}(t) \quad (5.6)$$

where $\mathbf{e}_r = \{0, 1, 0\}^T$ is the unit vector in the radial direction at the cutting point. Combining Eqs. (5.4) and (5.6) yields:

$$\mathbf{q}(t) = \mathbf{e}_r \mathbf{N}_c(t) \mathbf{Q}_r(t) \quad (5.7)$$

The resultant three-dimensional cutting forces on the tool is obtained by substituting $\mathbf{q}(t)$ in Eq. (4.28):

$$\mathbf{F}_c(t) = \mathbf{F}_s(t) + \mathbf{K}_{dc}(t) \mathbf{e}_r \mathbf{N}_c(t) \mathbf{Q}_r(t) - \mathbf{K}_{dd}(t) \mathbf{e}_r \mathbf{N}_c(t) \mathbf{Q}_r(t-T) + \mathbf{C}_p(t) \mathbf{e}_r \mathbf{N}_c(t) \dot{\mathbf{Q}}_r(t) \quad (5.8)$$

where the static force vector \mathbf{F}_s and dynamic matrices \mathbf{K}_{dc} , \mathbf{K}_{dd} , and \mathbf{C}_p are defined in Eqs. (4.29)-(4.32), respectively. The reaction force $-\mathbf{F}_c$ is exerted on the workpiece but only the radial force component, denoted as $f_{cr}(t)$, affects the chip regeneration process:

$$f_{cr}(t) = -\{0, 1, 0\} \{\mathbf{F}_c(t)\} = -\mathbf{e}_r^T \mathbf{F}_c(t) \quad (5.9)$$

The generalized force vector $\{\mathbf{F}_{Gr}(t)\}_{[m \times 1]}$, which consists of the instantaneous radial forces at all m discrete points around the circumference, can be obtained using the shape function \mathbf{N}_c :

$$\{\mathbf{F}_{Gr}(t)\}_{[m \times 1]} = \mathbf{N}_c^T(t) f_{cr}(t) \quad (5.10)$$

which combined with Eq. (5.9) yields:

$$\mathbf{F}_{Gr}(t) = -\mathbf{N}_c^T(t) \mathbf{e}_r^T \mathbf{F}_c(t) \quad (5.11)$$

All entries of $\{\mathbf{F}_{Gr}(t)\}$ are zeros except for the entry corresponding to the point (or points, depending on the chosen shape function) at the cutting region. The generalized vibration and force vectors are related to each other in Laplace domain as:

$$\mathbf{Q}_r(s) = \mathbf{G}_r(s) \mathbf{F}_{Gr}(s) \quad (5.12)$$

where $[\mathbf{G}_r(s)]_{[m \times m]}$ is the generalized structural dynamics of the workpiece in the radial direction. Each entry ij ($i, j = 1, 2, \dots, m$) in $\mathbf{G}_r(s)$ matrix contains the FRF from the radial force at point j to the radial vibrations at point i . Assume that the structural behaviour of the workpiece can be approximated by m_w number of circumferential shell modes. Similar to Eq. (4.42), the reduced generalized matrix $\mathbf{G}_r(s)$ can be constructed in Laplace domain as [44]

$$\mathbf{G}_r(s) = \hat{\mathbf{U}}_r (\mathbf{I}s^2 + 2\zeta \omega_n s + \omega_n^2)^{-1} \hat{\mathbf{U}}_r^T \quad (5.13)$$

where $\mathbf{I}_{[m_w \times m_w]}$ is the identity matrix, and $\zeta_{[m_w \times m_w]}$ and $\omega_n_{[m_w \times m_w]}$ are the diagonal damping ratio and natural frequency matrices, respectively. $\hat{\mathbf{U}}_{r[m \times m_w]}$ is the mass-normalized radial mode shape matrix:

$$\hat{\mathbf{U}}_r = \left[\begin{array}{c} \left\{ \begin{array}{c} u_{1,1} \\ u_{2,1} \\ \vdots \\ u_{m,1} \end{array} \right\} \\ \left\{ \begin{array}{c} u_{1,2} \\ u_{2,2} \\ \vdots \\ u_{m,2} \end{array} \right\} \\ \dots \\ \left\{ \begin{array}{c} u_{1,m_w} \\ u_{2,m_w} \\ \vdots \\ u_{m,m_w} \end{array} \right\} \end{array} \right]_{m \times m_w} \quad (5.14)$$

where each column corresponds to a circumferential shell mode. As illustrated in Figure 5.1, each circumferential pattern with i_c ($i_c = 2, 3, \dots$) number of waves

(lobes) has an arc wavelength of $2\pi/i_c$ with the corresponding mode shape vector:

$$\begin{aligned}\hat{U}(i_c) &= |A_{i_c}| \cos(i_c \varphi + \varphi_{0,i_c}), \quad 0 \leq \varphi \leq 2\pi \\ &= |A_{i_c}| \cos\left(i_c(k-1)\frac{2\pi}{m} + \varphi_{0,i_c}\right), \quad 1 \leq k \leq m\end{aligned}\quad (5.15)$$

where $|A_{i_c}|$ is the mass-normalized amplitude, and φ_{0,i_c} is a constant determined based on the boundary conditions. Extraction of mode shapes using FE and experimental methods is discussed in Section 5.5.

The generalized radial vibration vector $\mathbf{Q}_r(t)$ is transformed to the modal space using the mode shape matrix $\hat{\mathbf{U}}_r$ as:

$$\mathbf{Q}_r(t) = \hat{\mathbf{U}}_r \boldsymbol{\Psi}_r(t) \quad (5.16)$$

where $\{\boldsymbol{\Psi}_r(t)\}_{[m_w \times 1]}$ is the modal radial displacement vector. Combining Eqs (5.12), (5.13), and (5.16), and following similar derivations presented in Eqs. (4.47)-(??), the dynamic equation of motion in terms of the modal displacement vector can be written in Laplace domain as:

$$(\mathbf{I}s^2 + 2\zeta \boldsymbol{\omega}_n s + \boldsymbol{\omega}_n^2) \boldsymbol{\Psi}_r(s) = \hat{\mathbf{U}}_r^T \mathbf{F}_{Gr}(s) \quad (5.17)$$

The generalized force vector \mathbf{F}_{Gr} is written in terms of modal displacement vector ($\boldsymbol{\Psi}_r$) by combining Eqs. (5.8), (5.11), and (5.16):

$$\begin{aligned}\mathbf{F}_{Gr}(t) &= -\mathbf{N}_c^T(t) \mathbf{e}_r^T \mathbf{F}_c(t) \\ &= -\mathbf{T}_{sc}(t)^T \mathbf{F}_s(t) - \mathbf{T}_{sc}(t)^T \mathbf{K}_{dc}(t) \mathbf{T}_{sc}(t) \hat{\mathbf{U}}_r \boldsymbol{\Psi}_r(t) \\ &\quad + \mathbf{T}_{sc}(t)^T \mathbf{K}_{dd}(t) \mathbf{T}_{sc}(t) \hat{\mathbf{U}}_r \boldsymbol{\Psi}_r(t-T) - \mathbf{T}_{sc}(t)^T \mathbf{C}_p(t) \mathbf{T}_{sc}(t) \hat{\mathbf{U}}_r \dot{\boldsymbol{\Psi}}_r(t)\end{aligned}\quad (5.18)$$

where

$$[\mathbf{T}_{sc}(t)]_{[3 \times m]} = \{\mathbf{e}_r\}_{[3 \times 1]} \{\mathbf{N}_c(t)\}_{[1 \times m]} \quad (5.19)$$

is defined as the equivalent transformation from the generalized shell coordinates (in the radial direction) to the three-dimensional tool CS at the cutting point. Finally, the dynamic equation of motion for the instantaneous response of the cylindrical shell under the threading loads can be written in time domain modal space by

combining Eqs. (5.17) and (5.18):

$$\ddot{\Psi}_r(t) + (\mathbf{C}_{m,1} + \mathbf{C}_{m,2}(t))\dot{\Psi}_r(t) + (\mathbf{K}_{mc,1} + \mathbf{K}_{mc,2}(t))\Psi_r(t) + \mathbf{K}_{md}(t)\Psi_r(t-T) = \mathbf{F}_{sm}(t) \quad (5.20)$$

where

$$\begin{aligned} \mathbf{C}_{m,1} &= [2\zeta \boldsymbol{\omega}_n]_{[m_w \times m_w]}, & \mathbf{C}_{m,2}(t) &= \mathbf{T}_{sc}(t)^T \mathbf{C}_p(t) \mathbf{T}_{sc}(t) \\ \mathbf{K}_{mc,1} &= [\boldsymbol{\omega}_n^2]_{[m_w \times m_w]}, & \mathbf{K}_{mc,2}(t) &= \mathbf{T}_{sc}(t)^T \mathbf{K}_{dc}(t) \mathbf{T}_{sc}(t) \\ \mathbf{K}_{md}(t) &= -\mathbf{T}_{sc}(t)^T \mathbf{K}_{dd}(t) \mathbf{T}_{sc}(t) \\ \mathbf{F}_{sm}(t) &= -\mathbf{T}_{sc}(t)^T \mathbf{F}_s(t) \end{aligned} \quad (5.21)$$

where the static force vector \mathbf{F}_s and dynamic matrices \mathbf{K}_{dc} , \mathbf{K}_{dd} , and \mathbf{C}_p are defined in Eqs. (4.29)-(4.32), respectively.

Since Eq. (5.20) has the exact form as Eq. (4.49), all the state space derivations and time-marching numerical simulation techniques presented in Section 4.8 can be readily used to solve for $\Psi_r(t)$. Once the modal displacement vector $\Psi_r(t)$ is obtained, the radial vibrations at each point k ($k = 1, 2, \dots, m$) can be calculated using Eq. (5.16). The resultant axial, radial, and tangential forces, which include both the static and dynamic components, are evaluated from Eq. (5.8). The instantaneous radial vibration at the cutting point, which generates the finish surface, can be obtained using the shape function in Eq. (5.4).

Remark 1. Due to the time dependency of the shape function $N_c(t)$ (and thus $\mathbf{T}_{sc}(t)$), the stability of the process cannot be analyzed in frequency domain using Nyquist criterion. Instead, time domain techniques such as semi-discretization [20] and full-discretization [39] can be implemented by stacking all the state vectors over one spindle revolution. The stability of the process is then analyzed based on the eigen values of the augmented matrix [44], which has a size of $[2(m \times m_w) \times 2(m \times m_w)]$. However, if the vibration frequency is significantly greater than the spindle rotation frequency, a large discretization number (m) is required to capture the wave length of the vibrations on the workpiece surface. In this case, the resultant augmented matrix becomes impractically large, and the eigen values cannot be evaluated using normal computers. If this is the case, full time history of the process must be simulated using the numerical time-marching techniques (Section 4.8), and stability is investigated based on the decay or growth of the vibrations.

Remark 2. If the vibration frequencies are at least two order of magnitudes greater than the spindle rotation frequency, the effect of residual shell vibrations on stability may be neglected. In this case, the vibration marks are densely packed around the circumference, and instability can occur locally. For these systems, frequency domain stability analysis developed in Chapter 4 can be used along with the FRF at the most dynamically flexible point around the circumference.

5.3.2 Sample Time Simulation Results

In order to demonstrate the response of cylindrical shells under threading loads, the case study presented in Section 4.9 is revisited here. Assume that the three-point V-profile insert shown in Figure 4.6.a is used to thread a thin-walled workpiece with diameter of $d_w = 70$ mm. The structural dynamics of the workpiece in the radial direction at the most dynamically flexible point around the circumference is provided in Figure 4.6.b and Table 4.1. Assume that modes 1 and 2 have two-lobe ($i_c = 2$) and three-lobe ($i_c = 3$) circumferential patterns, respectively (see Figure 5.1). The maximum amplitude of each mass-normalized mode shape vector i can be calculated based on the dynamic parameters in Table 4.1 as:

$$|\hat{U}_i| = \frac{1}{\sqrt{m_i}} = \frac{\omega_{n,i}}{\sqrt{k_{s,i}}} \quad (\omega_n \text{ in rad/s}) \quad (5.22)$$

which gives 0.154 and 0.254 for modes 1 and 2, respectively. Using Eq. (5.15), the mode shape vectors can be obtained as:

$$\begin{aligned} \hat{U}_1(i_c = 2) &= 0.154 \cos\left(\left(k-1\right)\frac{4\pi}{m}\right), \quad 1 \leq k \leq m \\ \hat{U}_2(i_c = 3) &= 0.254 \cos\left(\left(k-1\right)\frac{6\pi}{m}\right), \quad 1 \leq k \leq m \end{aligned} \quad (5.23)$$

where $m = 10,000$ discretization points have been used for the simulations in this section.

The process has been simulated using the same cutting conditions as in Figure 4.7.b, i.e. radial infeed of 1.6 mm and spindle speed of 1850 rpm. Figure 5.3.a shows the simulated vibrations at the cutting point (Eq. (5.4)) over the first 50 spindle revolutions. It can be seen that while the operation is stable, the vibrations continue to exist even after the process reaches “steady” condition. The generated

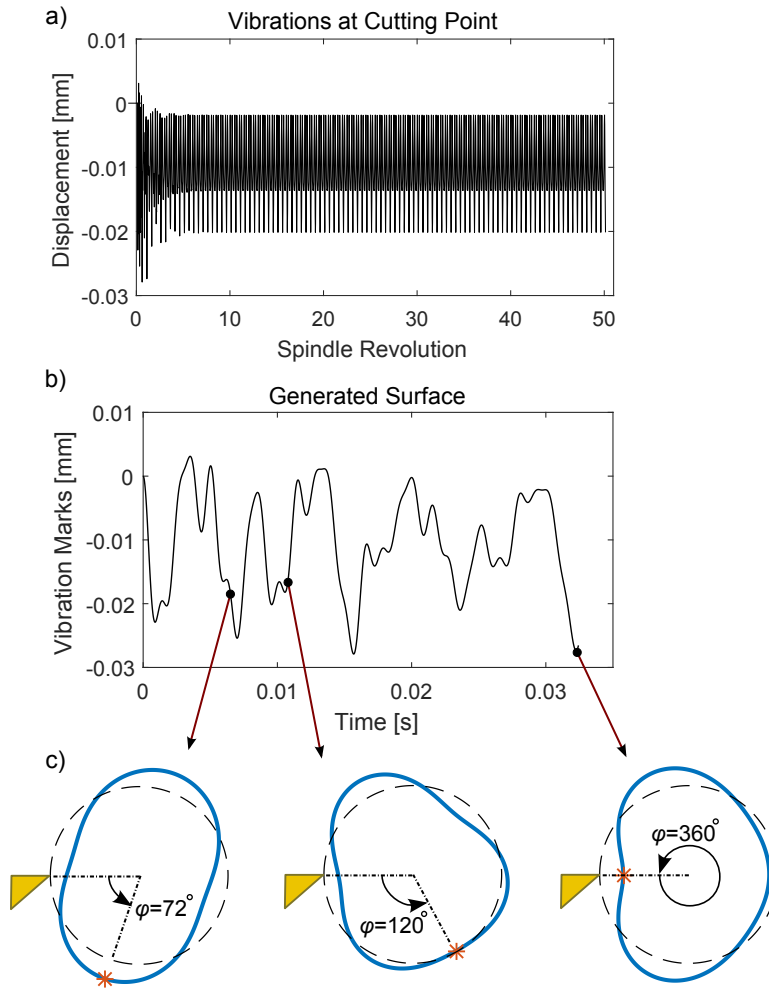


Figure 5.3: Simulated shell response under threading loads, a) vibrations at the cutting point, b) generated surface over the first revolution, c) sample instantaneous shell deformation (scaled, spindle speed: 1850 rpm, $\omega_{n,1} = 300$ Hz, $\omega_{n,2} = 700$ Hz).

surface over the first spindle revolution along with the corresponding shell deformation (Eq. (5.3)) at few instances are shown in Figure 5.3.b and c, respectively. It can be seen that the deformations continuously vary through the mixed two-lobe and three-lobe patterns.

5.4 Application: Threading Oil Pipes

In order to validate the dynamic models developed in Chapters 4 and 5, extensive threading experiments have been conducted on real scale oil pipes. The remainder

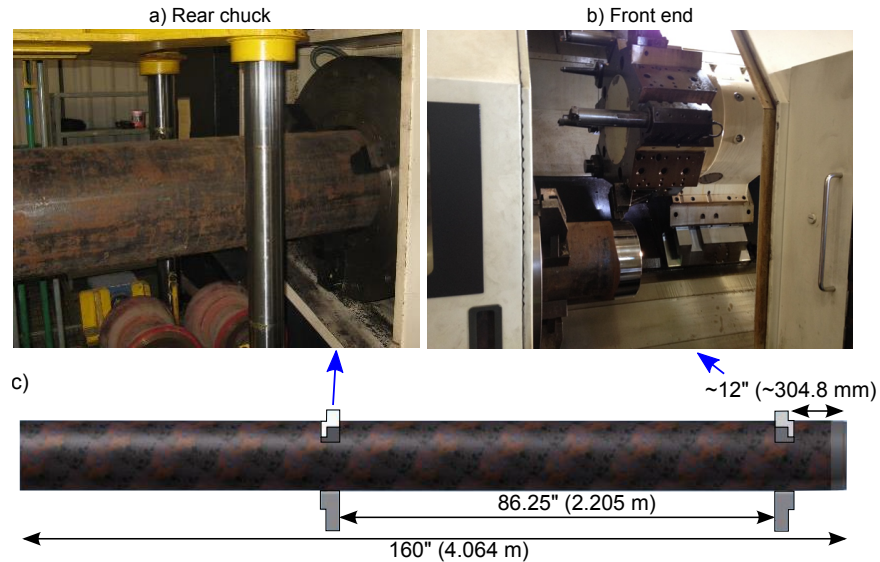


Figure 5.4: Experimental setup: a,b) front and rear clamping chucks in Mazak SLANT-TURN 60 lathe, c) distance between clamping locations.

of the chapter is dedicated to presenting the results and discussions.

5.4.1 Experimental Setup

Figures 5.4 shows a clamped pipe on Mazak SLANT-TURN 60 machining centre. The pipe is 4 m long, and it is held by two three-jaw chucks, one close to the front end and the other one between the centre and the rear end. Two types of pipes with diameters of 7" (177.8 mm) and 13 $\frac{3}{8}$ " (339.7 mm) have been used for the experiments². For simplicity, these pipes are referred to as D7 and D13, respectively. The wall thickness is originally 0.5" (12.7 mm), which is tapered down to 0.43" (10.9 mm) with a small taper angle of $\frac{3}{4}$ " per ft ($1^{\circ}47'$) before threading. The pipe material is custom steel with hardness in the range of 240-250 BHN (23-25 HRC). As shown in Figures 5.5.a and b, the clamping jaws for these two pipes have different contact length, resulting in different structural behaviour and mode shapes of the pipes. Two types of inserts have been used in the experiments (Figures 5.5.c and d):

- 5-point buttress (Ceratizit, 4.371-CE-LP025) with pitch of 5 TPI (5.08 mm) and depth of 0.062" (1.57 mm).

²Imperial units are more common in oil and gas industry. The dimensions in this chapter are presented in inches, and the equivalents in millimetres (rounded) are provided in the parentheses.

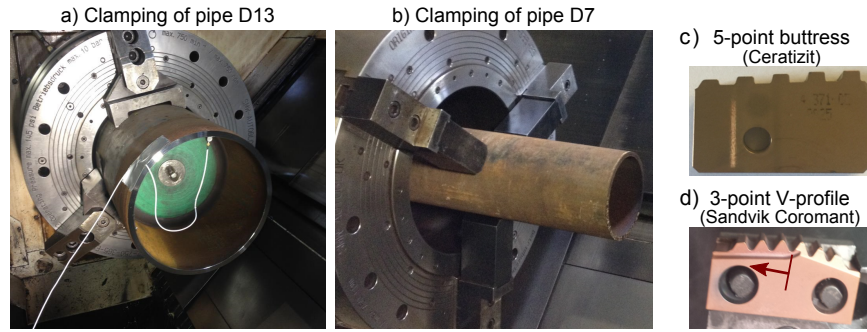


Figure 5.5: Pipes and the cutting inserts used in the experimental tests.

- Three-point V-profile (Sandvik Coromant R166.39G-24RD13-080) with pitch of 8 TPI (3.175 mm) and depth of 0.071" (1.8 mm).

The measurement setup is shown in Figure 5.6. The eccentricity of the pipe is measured using a dial gage and has been kept below 0.030" (0.76 mm) during the initial set up. An instrumented hammer and accelerometers have been used for modal analysis, and sound data during chatter tests have been collected with a microphone. A laser displacement sensor has been mounted normal to the pipe axis to measure the dynamic eccentricity and vibrations.³

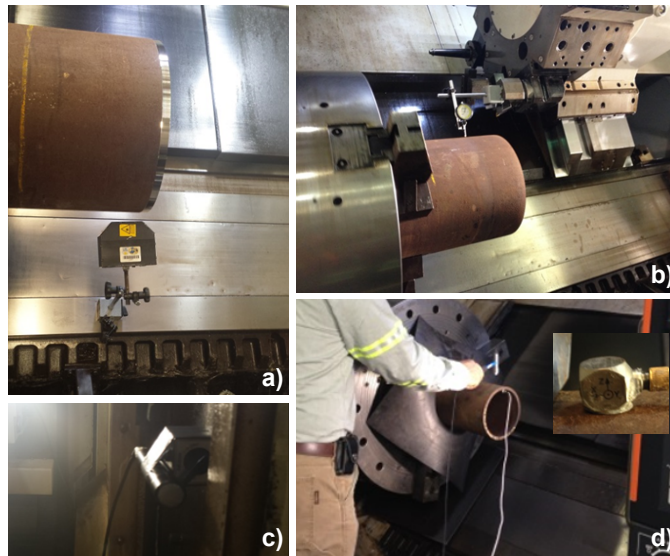


Figure 5.6: Measurement devices: a) laser displacement sensor, b) dial gauge, c) microphone, d) instrumented hammer and accelerometer.

³The laser sensor was not used during the machining operation due to chip entangling concerns.

5.4.2 Dynamic Behaviour Across Clamping Chucks

In order to investigate the effect of chucks on vibration isolation, pipe D7 has been hit at the tip with an instrumented hammer. The vibrations have been measured at three points along the pipe axis (Figure 5.7.a): P1 and P2 right in front and behind of the front chuck, and P3 behind the rear chuck. Figure 5.7.b and c compare the measured FRFs at these three points. It can be seen that the vibrations behind the front chuck (P2) are even larger than those at P1. This is due to the axial pattern of the dominant mode shape, which is analyzed in more details in Section 5.5.2. Nevertheless, this observation confirms that the three-jaw chucks cannot effectively restrict the flexibilities of the pipe at the clamping location. Similar conclusions were deduced from the hammer tests on pipe D13.

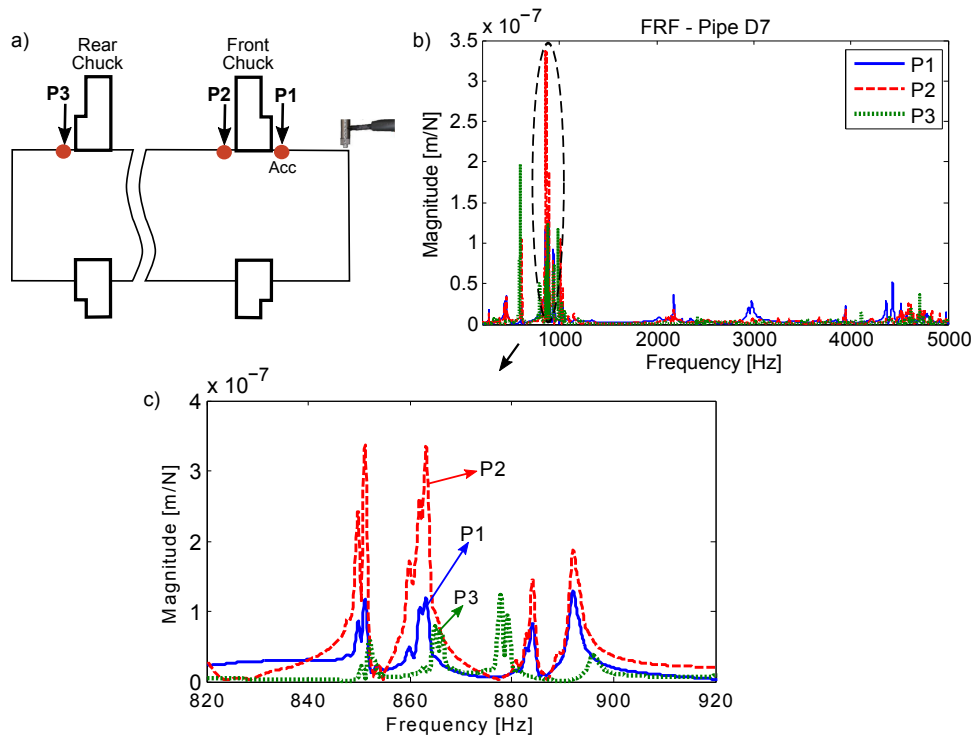


Figure 5.7: Effectiveness of chuck clamping in vibration isolation (pipe D7): a) measurement points, b) FRFs between the tip and the measurement points, c) comparison of FRFs at the dominant mode.

5.4.3 Effect of Jaw Configuration

During the threading operation and as the spindle rotates, the structural dynamics of the pipe at the cutting location can vary as a function of jaw positioning (boundary conditions). In order to investigate the significance of jaw configuration, hammer tests have been performed at two extreme cases shown in Figures 5.8.a and b. The measured FRFs at the tip of pipe D7 are compared in Figures 5.8.c and d. It can be seen that case 1, in which one jaw aligns with the cutting point, results in the lowest stiffness. This is due to the fact that in case 1 there is minimum support at the opposite side of the cutting point to limit the deflections. The measured FRFs for pipe D13 led to the same conclusion. Hence, all the stability charts presented in this chapter have been generated based on case 1 configuration, which is the most flexible setup.

In order to determine the source of flexibilities leading to chatter vibrations, structural behaviour of the pipe is studied in the next section.

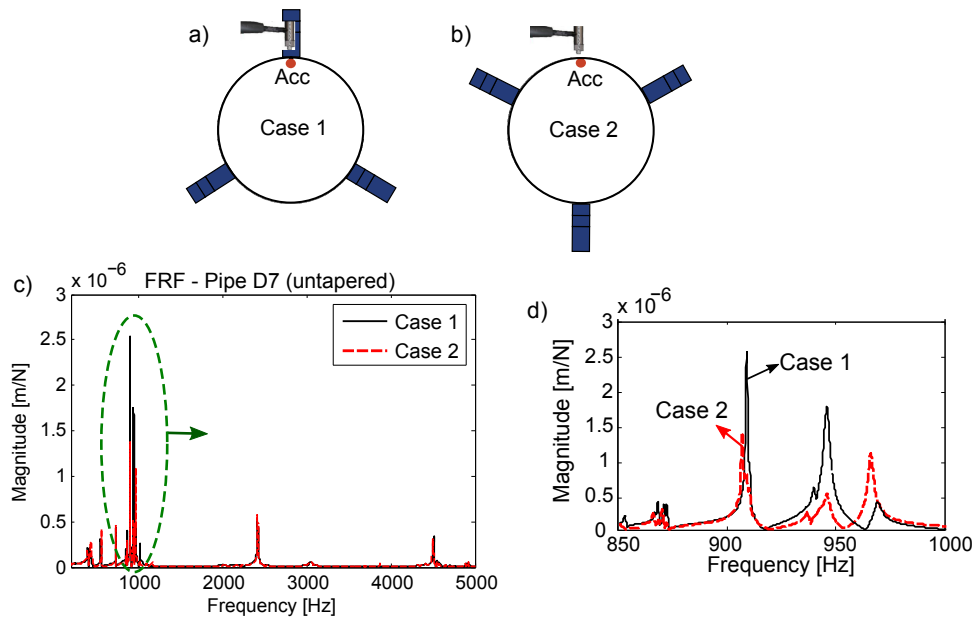


Figure 5.8: Effect of jaw configuration on pipe dynamics: a) Case 1: jaw aligned with the measurement point, b) Case 2: measurement point between two jaws, c) direct FRFs at the tip, d) comparison of FRFs at the dominant mode.

5.5 Mode Shape Analysis of Oil Pipes

Casings and tubes used in pipelines have diameter-to-thickness ratios typically in the range of 15-40, which makes them exhibit dominant shell modes. Finite element analysis of sample pipes is presented in the following section.

5.5.1 Finite Element Mode Shape Extraction

Pipe D13 with thickness of 0.5'' (12.7 mm) and clamping stickout of 12'' (304.8 mm) has been modelled in ANSYS using 8-node SHELL93 elements with six degrees of freedom at each node. The nodes corresponding to the contact area between the jaws and the pipe have been fixed, and modal analysis based on Block Lanczos method has been performed. Figures 5.9.a-c show the first three mode shapes of the clamped pipe.

Assume that each node p has six degrees of freedom denoted as p_k , ($k = x, y, z, \theta_x, \theta_y, \theta_z$). For each mode i , the mass-normalized mode shape vector corresponding to DOFs of node p , i.e.

$$\hat{U}_{p,i} = \begin{Bmatrix} u_{p_x,i} \\ u_{p_y,i} \\ u_{p_z,i} \\ u_{p_{\theta_x},i} \\ u_{p_{\theta_y},i} \\ u_{p_{\theta_z},i} \end{Bmatrix}, \quad (5.24)$$

can be extracted from ANSYS using the script provided in Appendix A. Consider two arbitrary nodes p and q , each having six degrees of freedom represented respectively as p_k and q_n ($k, n \in x, y, z, \theta_x, \theta_y, \theta_z$). If the first m_w number of modes are extracted from the FE analysis, the cross FRF between the arbitrary DOFs p_k and q_n can be approximated by summing the contribution of all m_w modes as

$$G_{p_k,q_n}(j\omega) = \sum_{i=1}^{m_w} \left[\frac{u_{p_k,i} \cdot u_{q_n,i}}{(\omega_{n,i}^2 - \omega^2) + 2j\zeta_i\omega_{n,i}\omega} \right] \quad (5.25)$$

where ζ_i and $\omega_{n,i}$ are the damping ratio and natural frequency of mode i . ζ_i must be estimated (or identified experimentally) and cannot be modelled from FE modal analysis. In Eq. (5.25), if $p_k = q_n$, the resultant frequency function (G_{p_k,p_k}) is called the direct FRF at point p in the direction of DOF k .

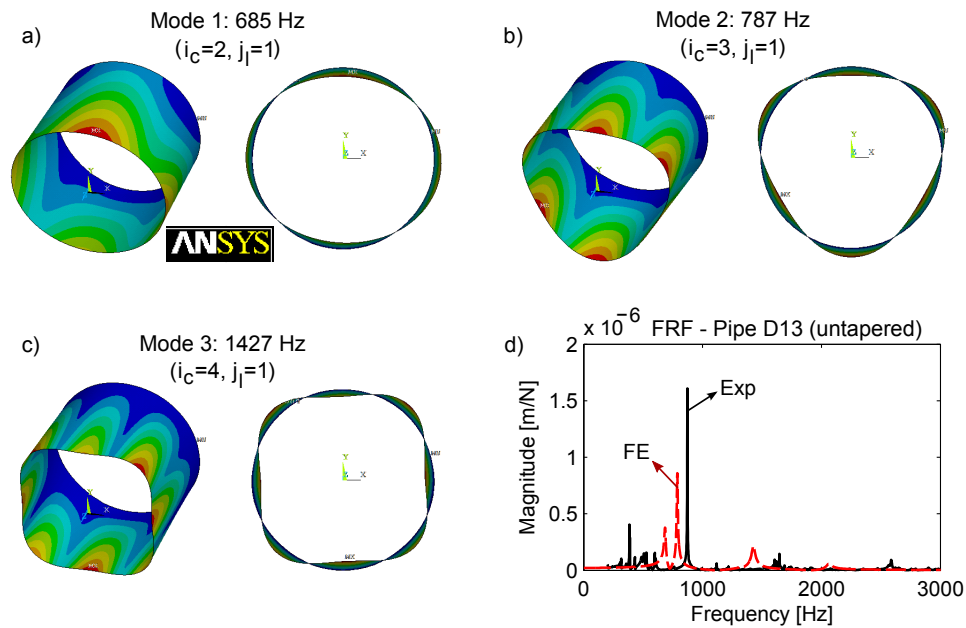


Figure 5.9: Finite element modal analysis of pipe D13 (stickout: 12'' (304.8 mm), thickness: 0.5'' (12.7 mm)): a-c) first three mode shapes, d) comparison of the FE and measured radial FRFs at the tip.

Figure 5.9.d compares the FE and measured direct FRFs in the radial direction at the tip of pipe D13 with stickout of 12'' (304.8 mm). The finite element FRF has been constructed using the first 10 modes and with assigned damping ratio of 0.5% (Eq. (5.25)). It can be seen that there is a considerable discrepancy between the FE and measured FRFs. This is mainly due to the fact that the jaws in the actual setup cannot fully restrict the pipe at the clamping points, as discussed in Section 5.4.2. Accurate FE modelling of the pipe dynamics requires advanced contact analysis, which is not the focus of this thesis. In order to validate the proposed threading models more accurately, the stability charts in this chapter are generated based on the measured FRFs. Experimental modal analysis of the pipe is presented in the following sections.

Remark 1. If the depth of the thread is considerable compared to the thickness of the pipe, the dynamic parameters can change over each pass as a result of material removal. The new FRF after each pass can be obtained using advanced analytical FRF updating methods [82]. Alternatively, if the pipe is modelled in FE using solid elements, the geometry after each threading pass can be re-meshed, and the new FRFs can be extracted. The stability model proposed in Chapters 4 and 5 can

accept different FRFs for different passes. However, it is assumed here that the pipe dynamics do not change considerably over the threading process. This assumption is discussed in more details in Section 5.6.4.

Remark 2. Stability limit for each pass is determined based on the most dynamically flexible point along the pipe axis, which can happen at a location other than the tip due to the shell behaviour of pipes.

5.5.2 Experimental Mode Shape Extraction

As illustrated in Figure 5.10, the circumference of the pipes D7 and D13 have been marked at every 45 degrees at several locations along the pipe axis including few points behind the chuck. The pipes have been hit with an instrumented hammer at each grid point, and the resultant vibrations at the tip have been measured with an accelerometer (in the radial direction).

Assume that the grid point at the location of accelerometer is called point 1. The direct FRF at this point can be approximated by contribution of m_w number of dominant modes as:

$$G_{11}(j\omega) = \sum_{i=1}^{m_w} \left[\frac{1/m_i}{(\omega_{n,i}^2 - \omega^2) + 2j\zeta_i\omega_{n,i}\omega} \right] \quad (5.26)$$

where m_i (i : mode number) is the modal mass, and $\omega_{n,i}$ and ζ_i are the natural frequency and damping ratio. These modal parameters are identified using least square method [83] by fitting Eq. (5.26) to the measured direct FRF. Table 5.1 provides the identified parameters for the most dominant modes of pipes D7 and D13.

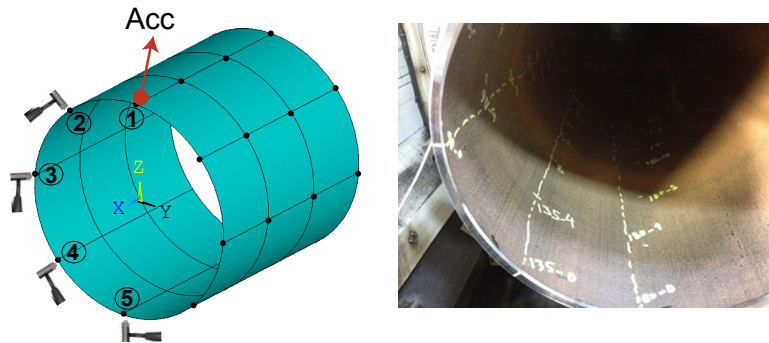


Figure 5.10: Grids for experimental mode shape analysis.

Table 5.1: Measured dynamic parameters of the dominant mode in pipes D7 (stickout: 11" (279.4 mm)) and D13 (stickout 12" (304.8 mm)), both tapered.

	natural frequency ω_n [Hz]	damping ratio ζ	modal stiffness k_s [N/m]	modal mass m [Kg]
Pipe D7	910	0.02%	1.2×10^9	36.7
	circumferential mode shape: -0.435, -0.018, 0.399, 0.076, -0.487			
	axial mode shape (top): 0.435, 0.269, 0.081, -0.038, -0.045			
	axial mode shape (bottom): -0.433, -0.222, -0.037, 0.081, 0.088			
Pipe D13	840	0.3%	2.9×10^8	10.5
	circumferential mode shape: 0.356, -0.277, -0.023, 0.194, -0.332			
	axial mode shape (top): 0.356, 0.252, 0.172, 0.107, 0.083, 0.053, 0.034			
	axial mode shape (bottom): 0.332, 0.238, 0.165, 0.103, 0.074, 0.046, 0.022			

The cross FRF between the hitting point k and the accelerometer (point 1) consists of the same modes as G_{11} but with different amplitudes (contributions):

$$G_{k1}(j\omega) = \sum_{i=1}^{m_w} \left[\frac{R_{k1,i}}{(\omega_{n,i}^2 - \omega^2) + 2j\zeta_i\omega_{n,i}\omega} \right] \quad (5.27)$$

where $R_{k1,i}$ is called the residue of mode i in the FRF between points k and 1. $R_{k1,i}$ values are identified using least square method by fitting Eq. (5.27) to the measured cross FRFs. Once the modal parameters and the residue values are known, the mass-normalized mode shape vector (in the radial direction) for each mode i can be obtained as:

$$\hat{U}_{r,i} = \begin{pmatrix} u_{1,i} \\ u_{2,i} \\ \vdots \\ u_{n_g,i} \end{pmatrix} \quad (5.28)$$

where n_g is the total number of grid points (FRFs), and the entries are calculated as [83]:

$$u_{1,i} = \frac{1}{\sqrt{m_i}} \quad (5.29)$$

$$u_{k,i} = \sqrt{m_i} R_{k1,i} \leftarrow 2 \leq k \leq n_g$$

where m_i and $R_{k1,i}$ are identified from the measured FRFs (Eqs. (5.26) and (5.27)). The experimental mode shapes must be interpolated by m number of discretization points before being used in time-marching simulations (Sections 4.8 and 5.3).

Figure 5.11 demonstrates the circumferential mode shape analysis at the tip of pipe D13. Only half of the circumference is analyzed due to symmetry (the jaw configuration is also symmetric). The magnitude and imaginary parts of the FRFs at the dominant mode (840 Hz) are compared in Figures 5.11.c and d, respectively. Relative displacements of the grid points in the radial direction can be compared

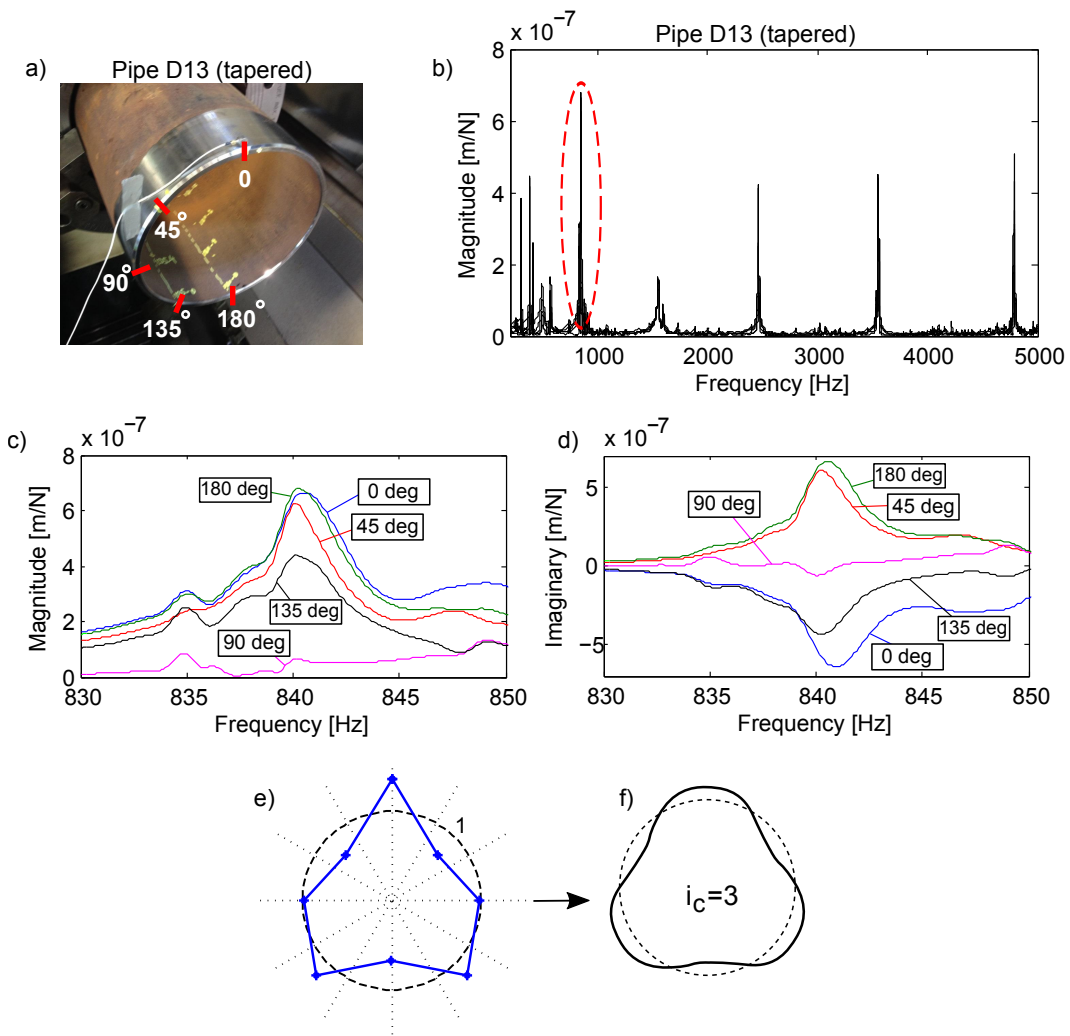


Figure 5.11: Circumferential mode shape analysis of pipe D13 (at the tip): a) measurement points, b) radial direct FRFs at all points, c-d) magnitude and imaginary components of the FRFs at the dominant mode, e-f) circumferential pattern of the dominant mode.

from the magnitude plot, and the relative phase can be deduced from the phase plot. For example, the points at the top (0 deg) and bottom (180 deg) have nearly same magnitude but opposite phase. The identified mode shape components are provided in Table 5.1 and plotted in a polar plane in Figure 5.11.e. It can be seen that pipe D13 exhibits its highest dynamic flexibility in three-lobe ($i_c = 3$) circumferential pattern.

Axial mode shape analysis of pipe D13 is presented in Figure 5.12. The radial FRFs have been measured along the top and bottom of the pipe at the locations shown in Figure 5.12.a. The measured FRFs around the dominant mode (840 Hz) are compared in Figures 5.12.b and c. It can be seen that all the grid points vibrate in-phase, and the amplitudes of vibrations continuously decrease from the tip towards the chuck. The FRFs along the bottom have nearly the same magnitude and imaginary components, thus have not been plotted for conciseness. The identified mode shapes along the top and bottom of the pipe are illustrated in Figure 5.12.d.

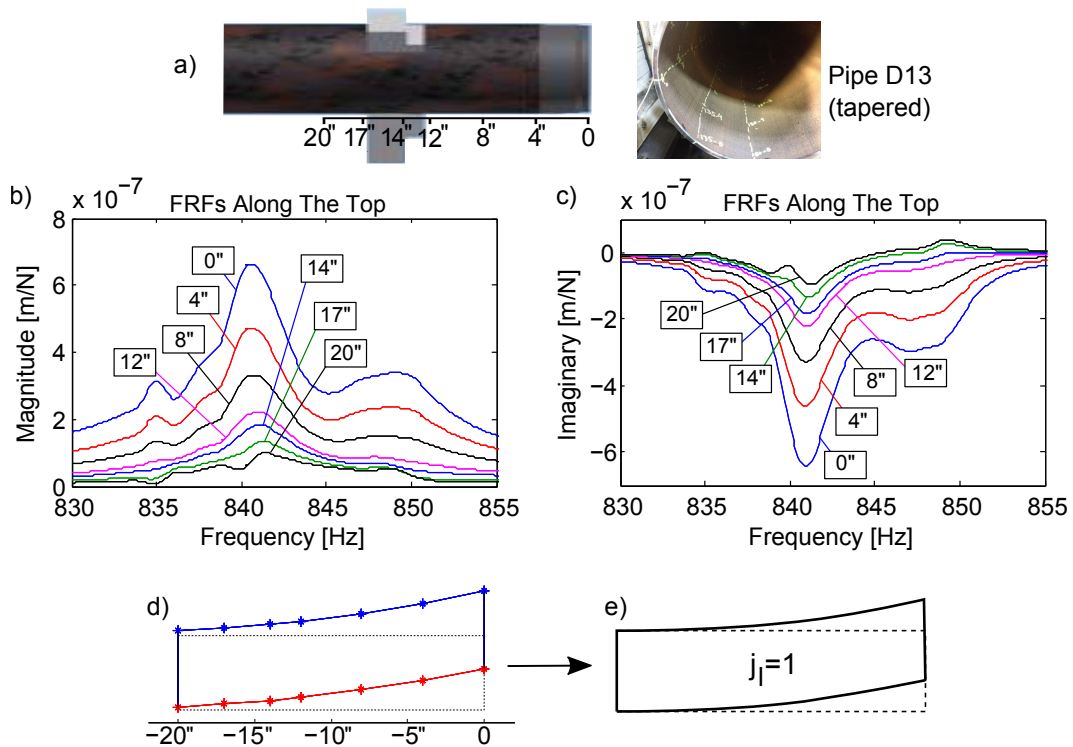


Figure 5.12: Axial mode shape analysis of pipe D13: a) measurement points, b-c) magnitude and imaginary components of the radial direct FRFs at the dominant mode, d-e) axial pattern of the dominant mode.

It can be seen that the dominant mode of pipe D13 has 1st-bending ($j_l = 1$) axial pattern.

Similarly, circumferential and axial mode shape analyses for pipe D7 are presented in Figures 5.13 and 5.14, respectively. Based on the identified parameters, pipe D7 exhibits highest dynamic flexibility in 2-lobe ($i_c = 2$) circumferential pattern (Figure 5.13.e) and 2nd-bending ($j_l = 2$) axial pattern (Figure 5.14.f). The mode shape components for the most dominant modes of pipe D7 and D13 are provided in Table 5.1.

Remark. Since both pipes D7 and D13 exhibit highest dynamic flexibility at the

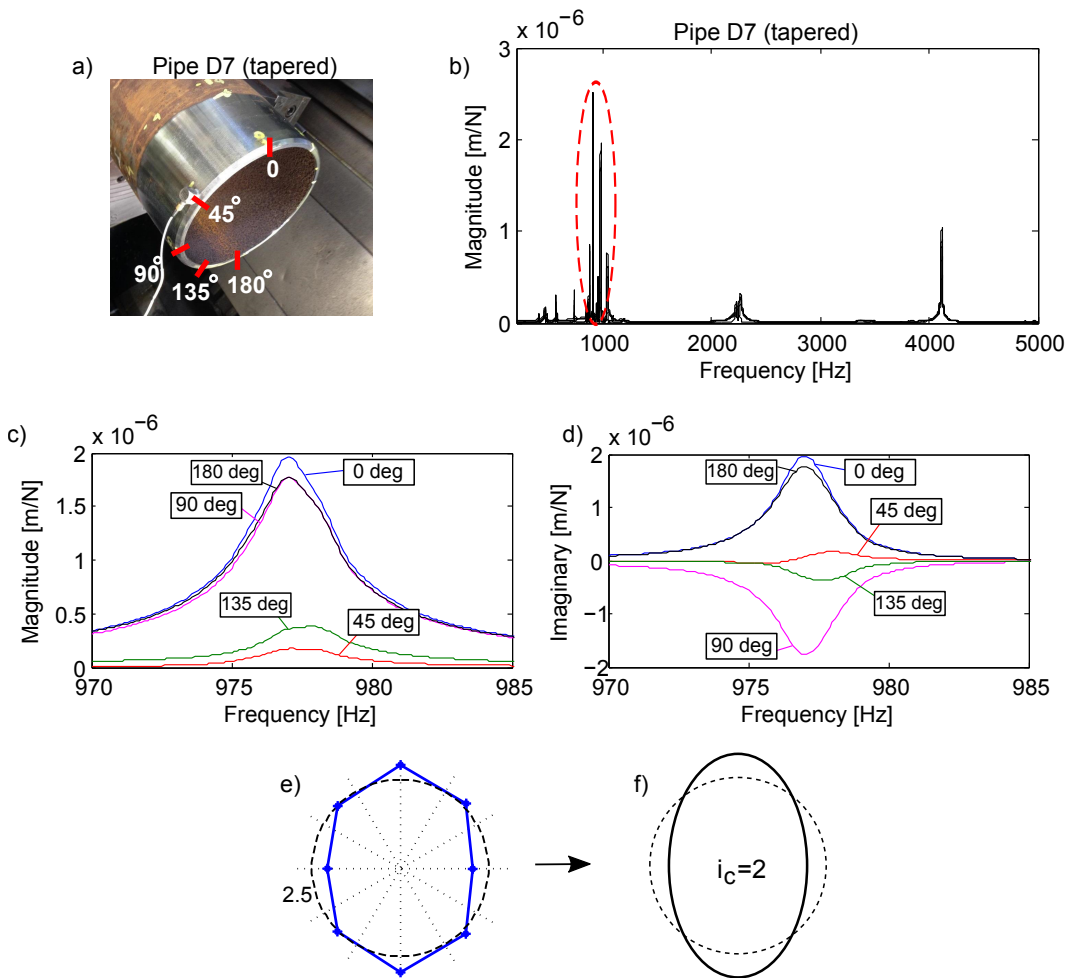


Figure 5.13: Circumferential mode shape analysis of pipe D7 (at the tip): a) measurement points, b) radial direct FRFs at all points, c-d) magnitude and imaginary components of the FRFs at the dominant mode, e-f) circumferential pattern of the dominant mode.

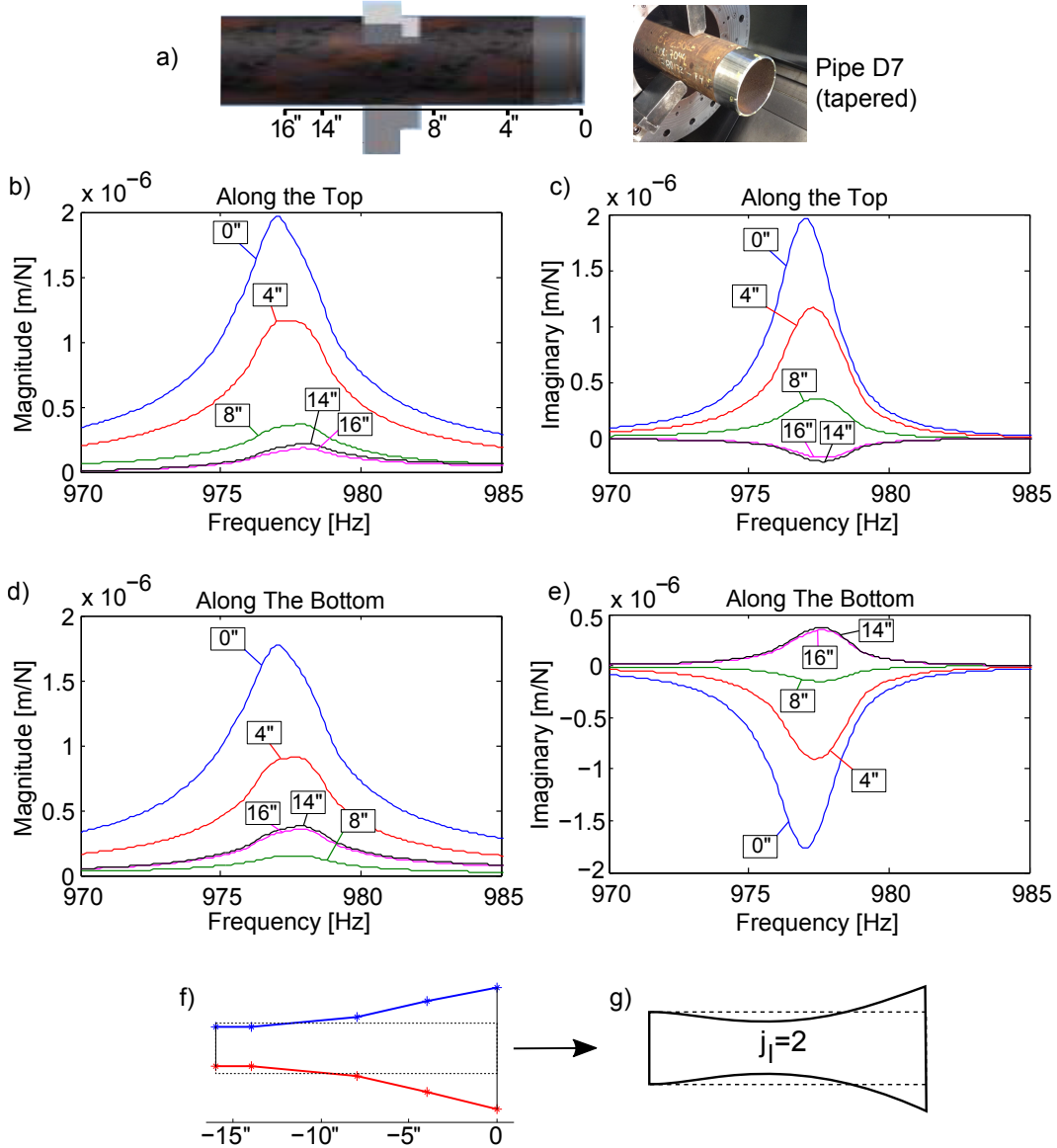


Figure 5.14: Axial mode shape analysis of pipe D7: a) measurement points, b-c) magnitude and imaginary components of the radial direct FRFs at the dominant mode along the top, d-e) FRFs along the bottom, f-g) axial pattern of the dominant mode.

tip, the stability charts presented in the next section have been generated based on the FRFs at the tip.

5.6 Chatter Experiments

Figure 5.15 categorizes different parameters affecting process stability in threading oil pipes. Stability limits subject to change in these parameters have been simulated and validated experimentally. The cutting force coefficients identified in Eq. (3.58) have been used in the simulations. The indentation coefficient and wear land in process damping model (Eq. 4.25) have been estimated as $K_{sp} = 4 \times 10^{13} \text{ N/m}^3$ and $L_w = 0.12 \text{ mm}$, respectively [22]. The predicted and experimental results for the threading tests are presented in the following sections.

Remark 1. Pipe D7 and D13 are machined at 120 rpm and 250 rpm, respectively. This means that the spindle rotation frequency in all experiments is less than 5 Hz while the vibration frequencies are around 1000 Hz. Hence, the frequency domain stability analysis developed in Section 4.6 can be used to predict the stability limits.

Remark 2. Setting up a pipe for threading experiments required a time-consuming procedure including mounting (with eccentricity control), surface cleaning, and tapering. After each set of experiments, the threaded section (or layer) was machined away, and if possible, the next tests were carried out on the same piece without unclamping the pipe. As a result, the FRFs and the stability charts presented in the following sections are different for different tests. In each case, the experimental results have been compared against the corresponding stability lobes.

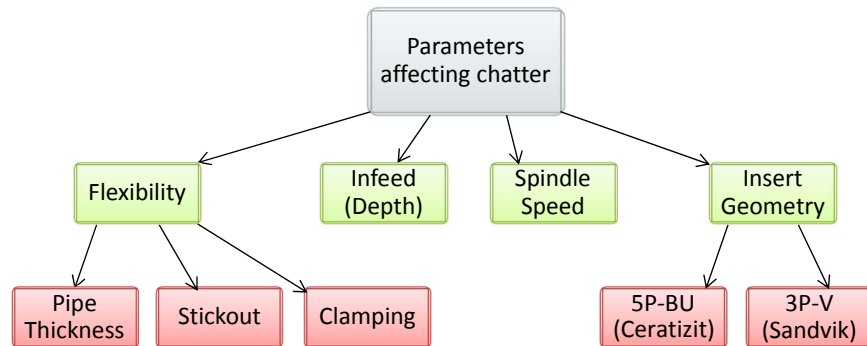


Figure 5.15: Parameters affecting chatter stability in threading oil pipes.

5.6.1 Threading Over Several Passes

In the first set of experiments, pipe D13 with thickness of 0.43'' (10.9 mm) has been threaded at spindle speed of 120 rpm (cutting speed of 130 m/min). Three passes with radial infeed of 0.020'' (0.508 mm)/pass have been cut using Ceratizit 5-point buttress insert. The sound data was collected using a microphone inside the machine. After finishing all three passes, the threaded layer was removed by axial turning, resulting in smaller wall thickness. Similar to the first set, another two sets of three passes at 0.020'' (0.508 mm)/pass were cut on the same piece.

Figure 5.16 shows the radial FRF at the tip of the pipe before conducting each threading set. The predicted stability chart for the first set is shown in Figure 5.17.a, where the experiment point (120 rpm, 0.508 mm) has been marked by a star. Stability lobe for each pass has been capped at the infeed value where the maximum thread depth for the insert is reached. Figures 5.17.b and c show the measured sound signal and its frequency contents, and the resultant surface finish is shown in Figure 5.17.d. Same plots for the second and third sets are presented in Figures 5.18 and 5.19, respectively. The predicted and experimental stability conditions for all passes are compared in Table 5.2. The dominant natural frequency (before each set) and the observed chatter frequency (if any) during each pass are also provided.

Based on the predicted stability lobes, all passes of set 1 are stable, and all passes of set 3 are unstable (heavy chatter). These predictions agree with the experimental results. The threading passes over set 2 exhibited marginal stability or light chatter; it can be seen in Figure 5.18 that the model predicts similar behaviour as

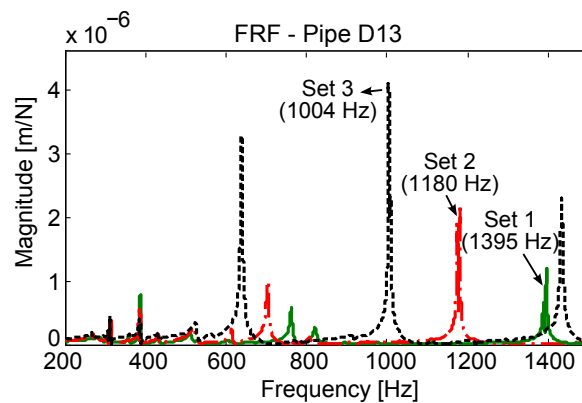


Figure 5.16: Measured FRFs at the tip of pipe D13 before each threading set.

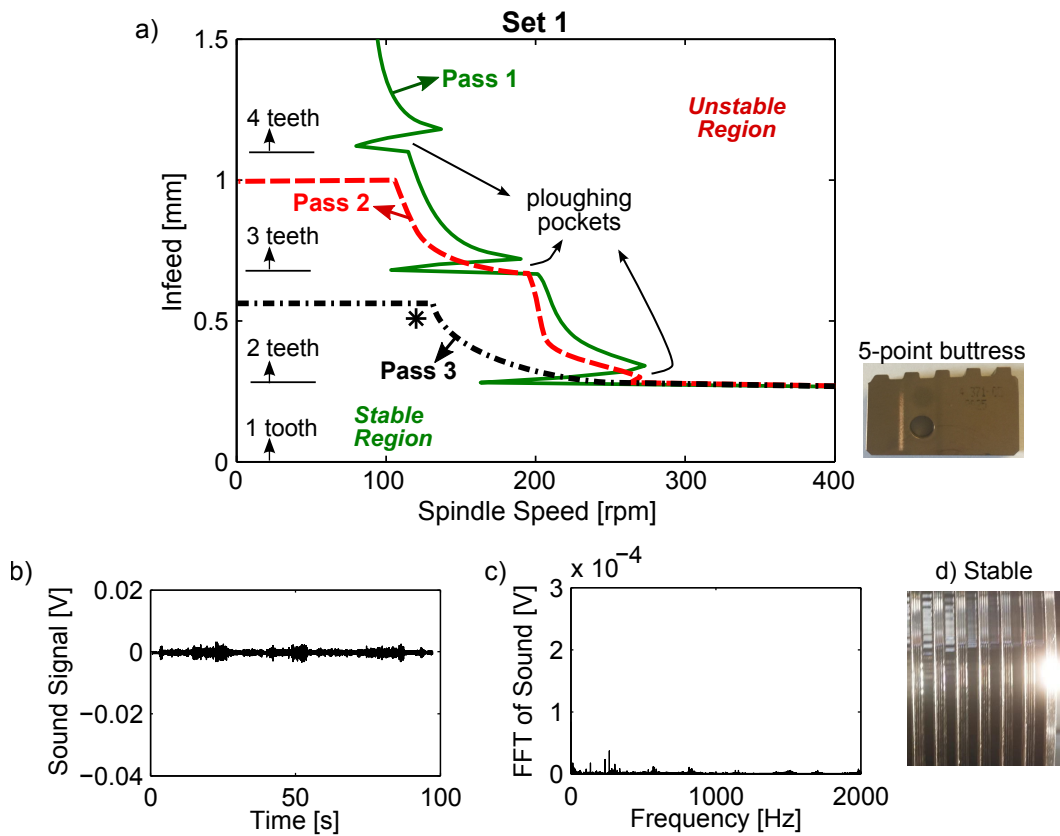


Figure 5.17: Experimental results for threading test Set 1 (pipe D13, 120 rpm, infeed: 0.020" (0.508 mm)/pass, insert: Ceratizit 5-point buttress): a) stability charts and the experiment point (star), b-c) recorded sound signal and its frequency contents, d) surface finish.

the experiment point is very close to the stability lobes, especially over the first and second passes of set 2.

Remarks: Ploughing Pockets in Stability Chart

The number of engaged teeth at each infeed value has been provided in the stability chart in Figure 5.17.a. It can be seen that at spindle speeds over 300 rpm, engaging more than one tooth leads to instability. Due to the large engagement length, cutting with multiple teeth is only feasible at lower spindle speeds where process damping significantly increases the stability limits. However, spindle speed must be above 100 rpm to avoid chip shearing problems.

As illustrated in Figure 5.17.a, at infeed values where an additional tooth engages in the cut, the stability lobes show a deep unstable pocket, which are marked

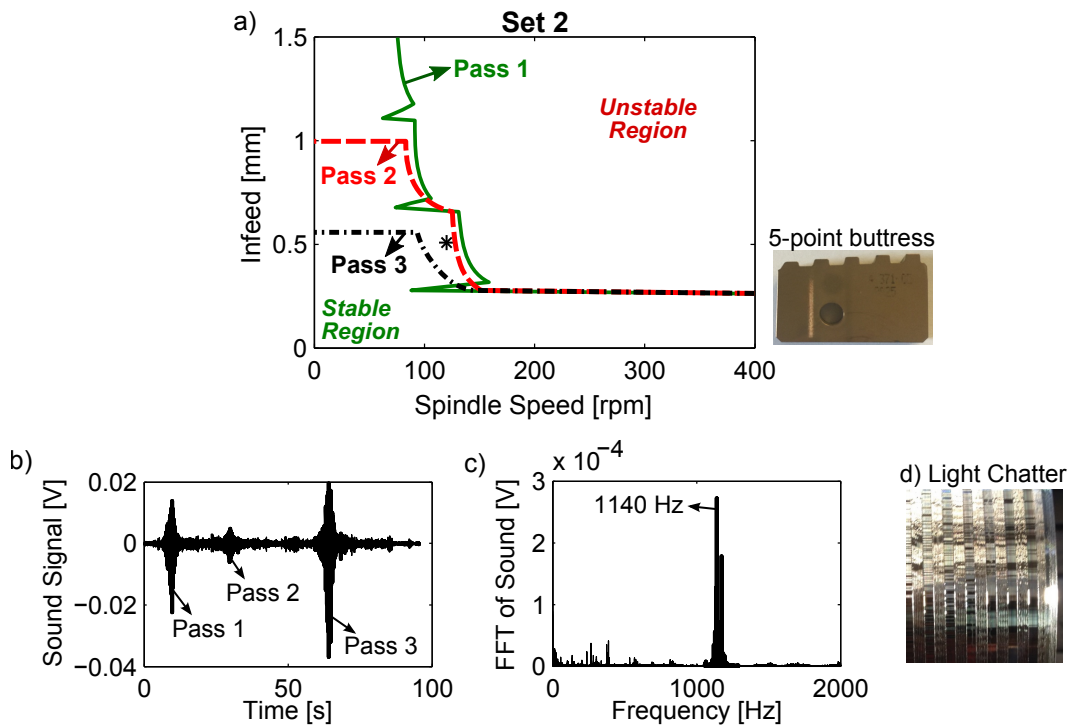


Figure 5.18: Experimental results for threading test Set 2 (pipe D13, 120 rpm, infeed: 0.020'' (0.508 mm)/pass, insert: Ceratizit 5-point buttress): a) stability charts and the experiment point (star), b-c) recorded sound signal and its frequency contents, d) surface finish.

Table 5.2: Comparison of experimental and predicted stability conditions for different passes (pipe D13, 120 rpm, infeed: 0.020'' (0.508 mm)/pass, insert: Ceratizit 5-point buttress) (S: stable, MS: marginally stable, C: chatter, LC: light chatter)

	ω_n [Hz]	Pass 1			Pass 2			Pass 3		
		sim	exp	ω_c [Hz]	sim	exp	ω_c [Hz]	sim	exp	ω_c [Hz]
Set 1	1395	S	S	-	S	S	-	S	S	-
Set 2	1180	S	LC	1173	MS	MS	-	C	C	1140
Set 3	1004	C	C	1001	C	(heavy chatter)		C	(heavy chatter)	

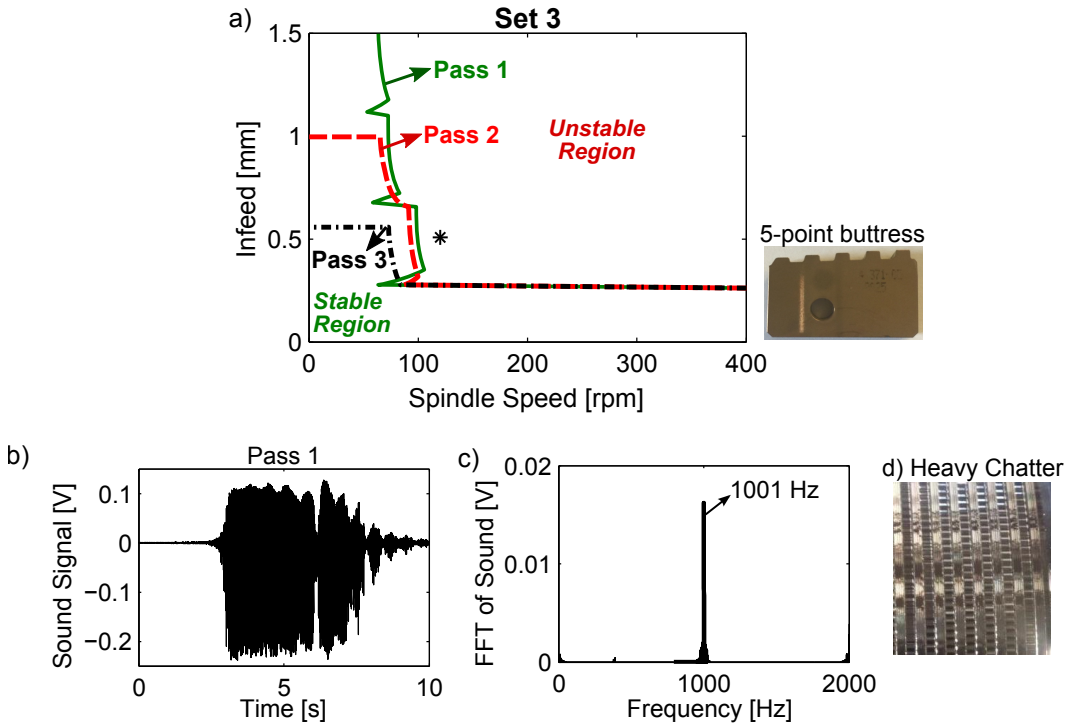


Figure 5.19: Experimental results for threading test Set 3 (pipe D13, 120 rpm, infeed: 0.020'' (0.508 mm)/pass, insert: Ceratizit 5-point buttress): a) stability charts and the experiment point (star), b-c) recorded sound signal and its frequency contents, d) surface finish.

as “ploughing pockets”. This is mainly due to the large ploughing forces as a result of small chip thickness on the added tooth. Since cutting force coefficients in this thesis have been calculated using nonlinear Kienzle model (Eq. (3.49)), the effect of ploughing has been reflected in the stability charts.

5.6.2 Threading at Different Infeed Values

The effect of infeed value on chatter stability has been examined on pipe D13 using Ceratizit 5-point buttress insert. Three experiments at infeed values of 0.020'' (0.508 mm), 0.025'' (0.635 mm), and 0.035'' (0.889 mm) have been conducted at 120 rpm (cutting speed of 130 m/min). Only one pass has been cut at each infeed value, and the threaded layer has been removed after each pass. Based on the insert geometry, the first two infeed values engage two teeth while the final experiment cut with three teeth.

Figure 5.20.a shows the measured radial FRFs at the tip before conducting each

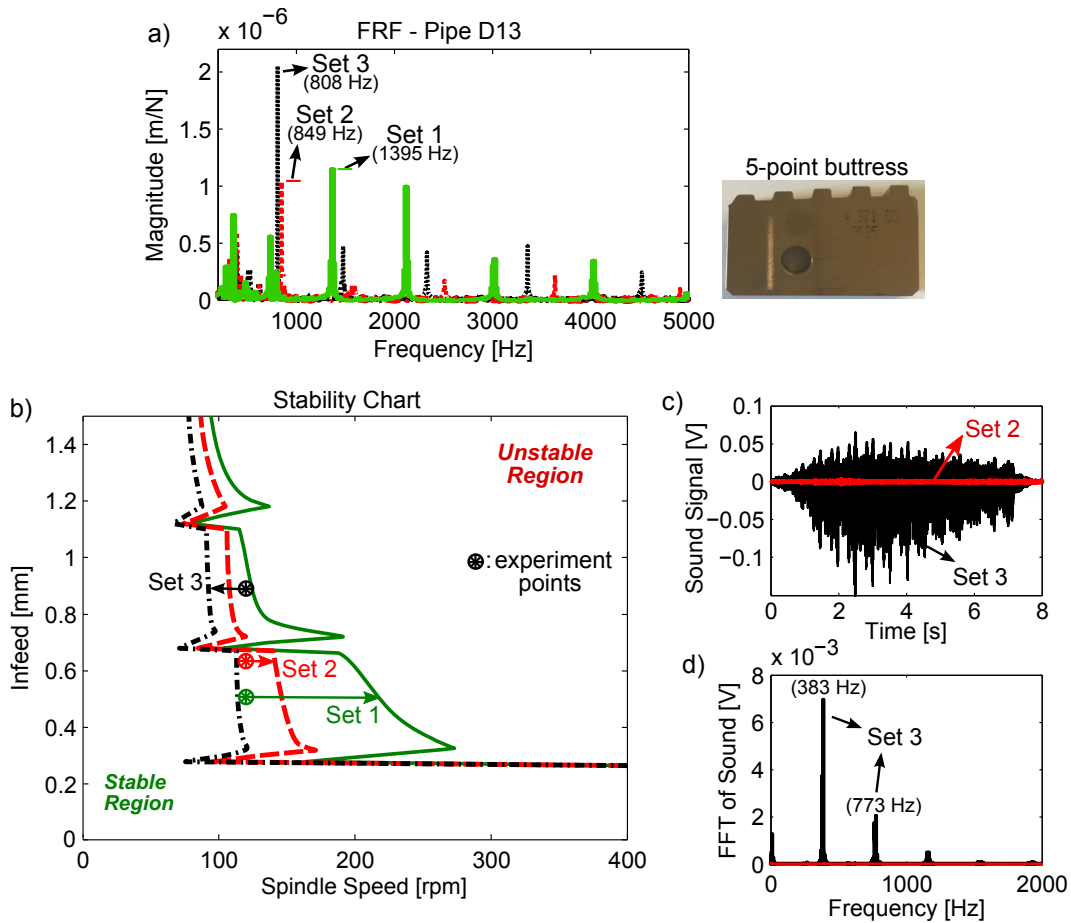


Figure 5.20: Experimental results at different infeed values (pipe D13, 120 rpm, insert: Ceratizit 5-point buttress): a) measured FRFs before each set, b) stability chart and the corresponding experiment point (star) for each set, c-d) sound signals and their frequency contents.

experiment. The predicted stability charts are shown in Figure 5.20.b. The arrows connect the experiment points (marked by stars) to their corresponding stability lobes. It can be seen that the model predicts the process to be stable at infeed values of $0.020''$ (0.508 mm) and $0.025''$ (0.635 mm), and unstable at $0.035''$ (0.889 mm). The recorded sound signals and their frequency contents are shown in Figures 5.20.c and d. As compared in Table 5.3, the predicted and experimental stability conditions agree at all three infeed values.

Remark. Due to the excessively large cutting forces in the third test (infeed of $0.035''$ (0.889 mm)), the structural mode of the clamping chuck has been excited as well. The frequency contents in Figures 5.20.c show chatter frequencies due to

Table 5.3: Experimental and predicted stability conditions at different infeed values (pipe D13, 120 rpm, insert: Ceratizit 5-point buttress) (S: stable, C: chatter)

	Infeed	ω_n [Hz]	sim	Pass 1	
				exp	ω_c [Hz]
Set 1	0.020" (0.508 mm)	1395	S	S	-
Set 2	0.025" (0.635 mm)	849	S	S	-
Set 3	0.035" (0.889 mm)	808	C	C	383, 773

both chuck mode (383 Hz) and pipe mode (773 Hz).

5.6.3 Threading With V-profile Insert

In order to verify the chatter stability model for V-profile threads, several tests have been conducted on pipe D7 with thickness of 0.3" (7.6 mm) using Sandvik Coro-mant three-point V-profile insert. One pass with infeed value of 0.025" (0.635 mm) has been cut at 250 rpm (cutting speed of 140 m/min). The original stickout of the pipe was 11" (279.4 mm). After the first test, the threaded section was cut away, leaving 9" (228.6 mm) stickout. A threading pass with the same infeed was cut on the new section. The procedure was repeated once more at 7" (177.8 mm) pipe stickout.

Figure 5.21.a shows the radial FRF at the tip of the pipe before conducting each test. The predicted stability charts are shown in Figure 5.21.b, where the experiment point (250 rpm, 0.635 mm) is marked by a star. The sound signals and their frequency contents are shown in Figures 5.21.c and d.

The simulation and experimental results are compared in Table 5.4. It can be seen that the model correctly predicts the stability conditions in all three tests with V-profile insert.

5.6.4 Remarks: Change in Pipe Dynamics During Threading

In order to investigate the effect of material removal on pipe dynamics, hammer tests have been conducted on pipe D13 before and after a threading operation. The original pipe thickness is 0.43" (10.9 mm), and the final thread depth (buttress) is 0.035" (0.89 mm). Figure 5.22 compares the FRF at the dominant mode for the

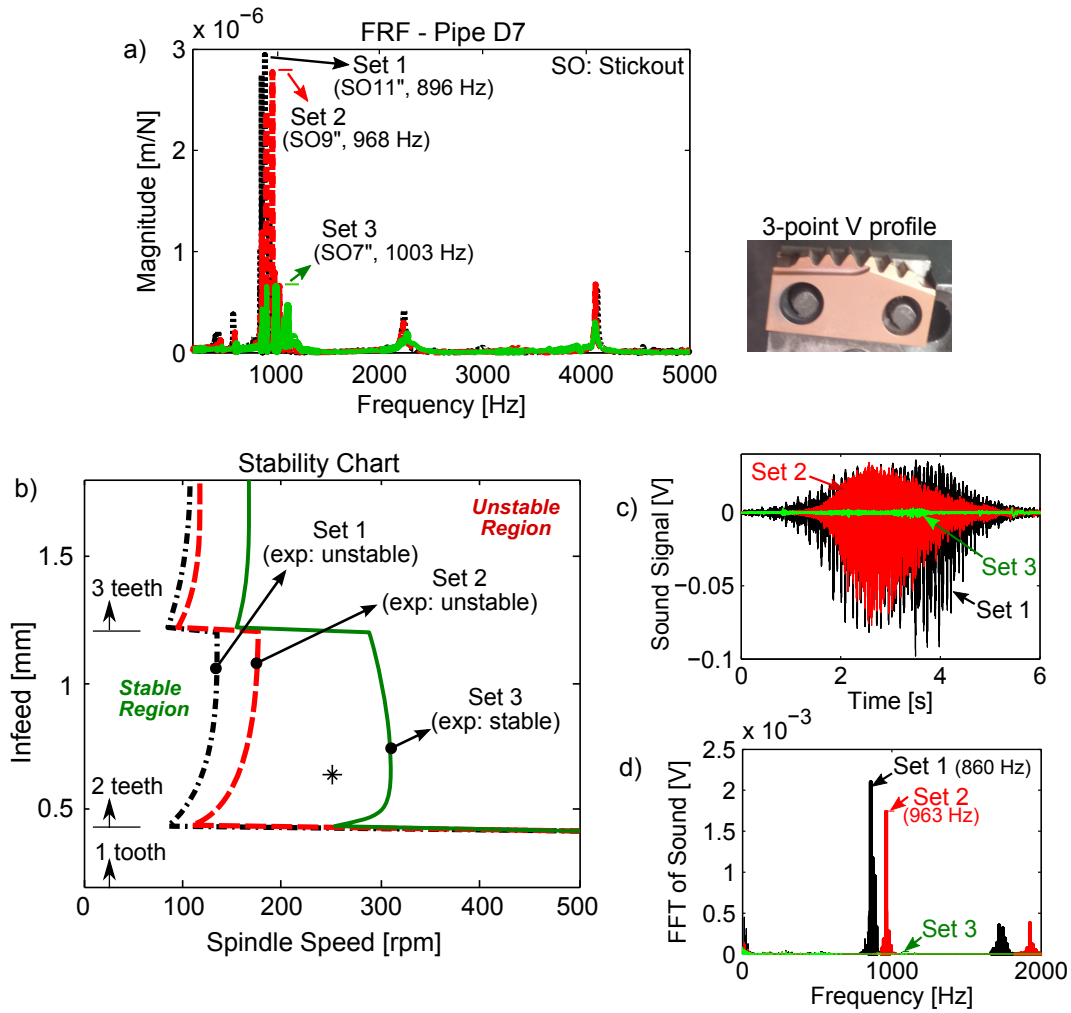


Figure 5.21: Experimental results with three-point V-profile insert at different pipe stickout (pipe D7, 250 rpm, infeed: 0.025'' (0.635 mm), insert: Sandvik Coromant 24RD13-080): a) measured radial FRFs before each set, b) stability charts and the experiment point (star), c-d) recorded sound signals and their frequency contents.

Table 5.4: Experimental and predicted stability conditions for three-point V-profile insert (pipe D7, infeed: 0.025'' (0.635 mm)) (s: stable, C: chatter).

	Pipe Stickout	ω_n [Hz]	sim	Pass 1	
				exp	ω_c [Hz]
Set 1	11'' (279.4 mm)	896	C	C	860
Set 2	9'' (228.6 mm)	968	C	C	963
Set 3	7'' (177.8 mm)	1003	S	S	-

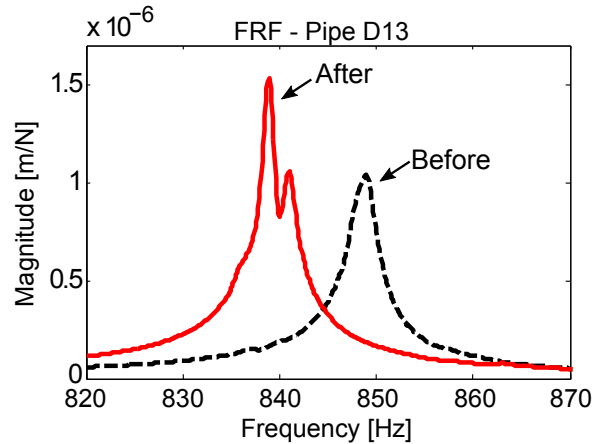


Figure 5.22: Change in the FRF of pipe D13 after a threading pass (thread depth: 0.035" (0.889 mm), buttress profile)

Table 5.5: Dynamic parameters of pipe D13 before and after threading (wall thickness: 0.43" (10.9 mm), thread depth: 0.035" (0.889 mm), buttress).

	natural frequency ω_n [Hz]	damping ratio ζ	modal stiffness K_s [N/m]	modal mass m [Kg]
Before	849	0.16%	3.0×10^8	10.5
After	839	0.16%	2.3×10^8	8.0

original and threaded pipe, and the modal parameters are compared in Table 5.5. It can be seen that even though the depth of the thread is less than 10% of the wall thickness, the dynamic stiffness at the dominant mode has decreased by nearly 40% after threading. This is mainly due to the sensitivity of shell modes to wall thickness. The natural frequency has shifted only about 1%.

Based on the experimental investigations, the pipe dynamics can change at least 10%-20% over each pass. Advanced FRF updating methods [82] can be employed to further improve the stability predictions especially over deeper passes.

5.7 Chatter Suppression Strategies

Thread turning is a restrictive operation in that the width of cut is dictated by the thread profile. Assuming that the insert and workpiece are already chosen, the only process parameters which can be selected by the operator are the spindle speed and infeed values. In multi-point inserts, however, the infeed settings affect the

chip geometry on the first tooth only. It is more effective to integrate the infeed strategies into the insert design; for example, the total width of cut can be reduced by implementing flank infeed or partial root engagement on some teeth (Figure 3.4).

Strategies which enhance the dynamic stiffness of the system or disrupt the chip regeneration process can effectively increase the stability limits in threading operations. Two sample approaches are presented in the following sections.

5.7.1 Effect of Additional Damping

As shown in Figure 5.23.a, a rubber ring has been mounted tightly inside pipe D13. The wall thickness of the pipe has been intentionally reduced to 0.25" (6.35 mm) to amplify the flexibilities. The radial FRF at the tip with and without the rubber ring are compared in Figure 5.23.b. Based on modal analysis of the FRFs, the modal damping at the dominant mode (640 Hz) has increased from 0.06% to 0.95%, i.e. more than 15 times. It can be seen in Figure 5.23.c that both FRFs have the same values at lower frequencies, which means that the damping ring has not changed the static stiffness.

A threading pass with infeed of 0.020" (0.508 mm) has been cut at 120 rpm

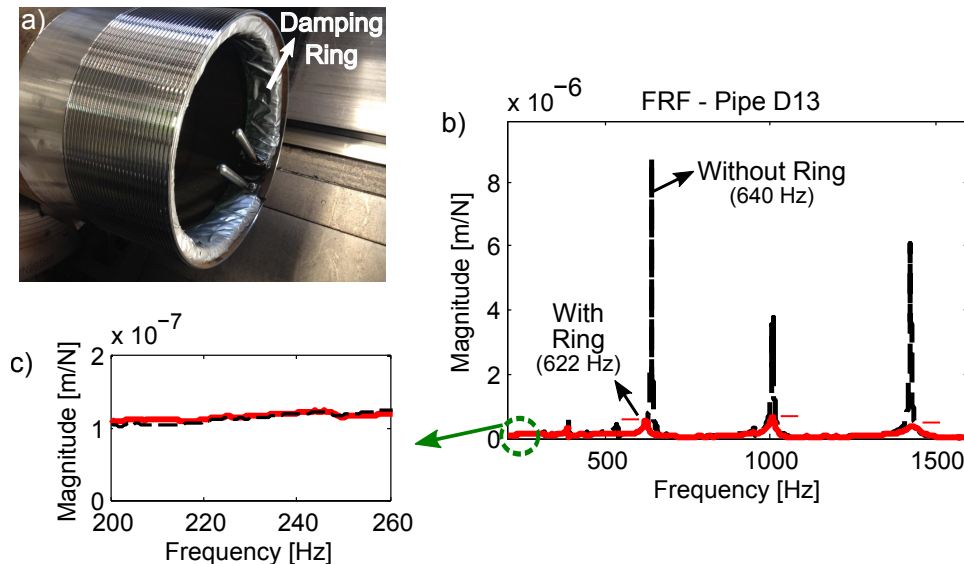


Figure 5.23: Effect of the damping ring on pipe dynamics (pipe D13, wall thickness: 0.25" (6.35 mm)): a) damping ring mounted inside, b) measured radial FRFs at the tip with and without the ring, c) comparison of the FRFs at low frequency region.

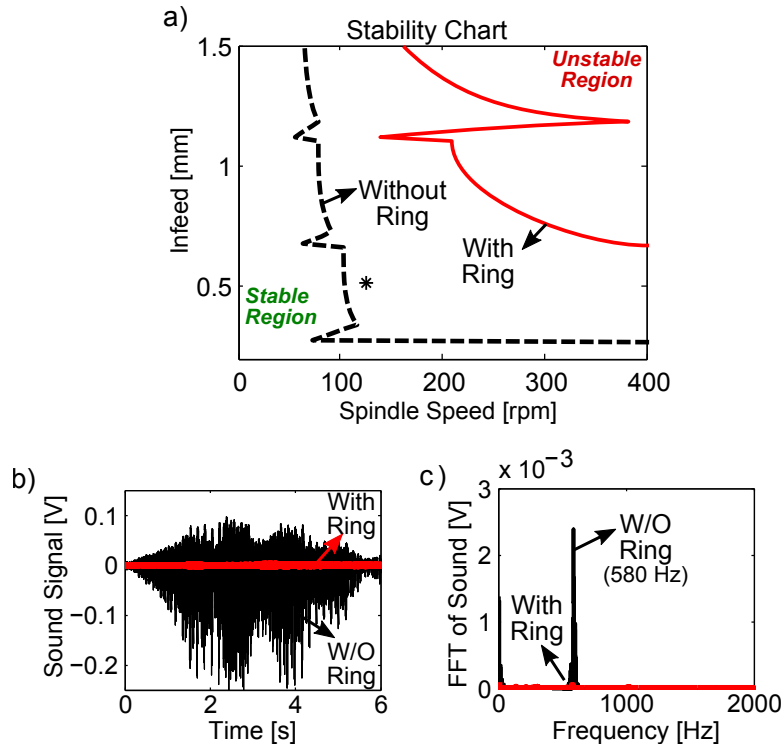


Figure 5.24: Effect of the damping ring on stability (pipe D13, Ceratizit 5-point buttress insert, 120 rpm): a) stability charts and the experiment point (star), b-c) recorded sound signals and their frequency contents.

using Ceratizit 5-point buttress insert. Figure 5.24.a shows the predicted stability lobes with and without the damping ring. The experiment point (120 rpm, 0.508 mm) is marked by a star. It can be seen that the damping ring significantly increases the stability limits. The recorded sound signals and their frequency contents are shown in Figures 5.24.b and c. The experimental results confirm that the process becomes fully stable when the damping ring is included.

It should be noted, however, that additional damping affects the stability limits only if it stiffens the dominant mode. This is the case when using the damping ring since the dominant modes have shell behaviour. As shown in Figure 5.25.a, instead of the damping ring, a thick layer of rubber has been placed between the pipe and the clamping jaws. Figure 5.25.b compares the FRF at the tip with and without the rubber. It can be seen that while some of the modes have been damped out significantly (possibly beam modes), the added rubber has had very little effect on the dynamic stiffness at the dominant mode. This is again due to the fact that

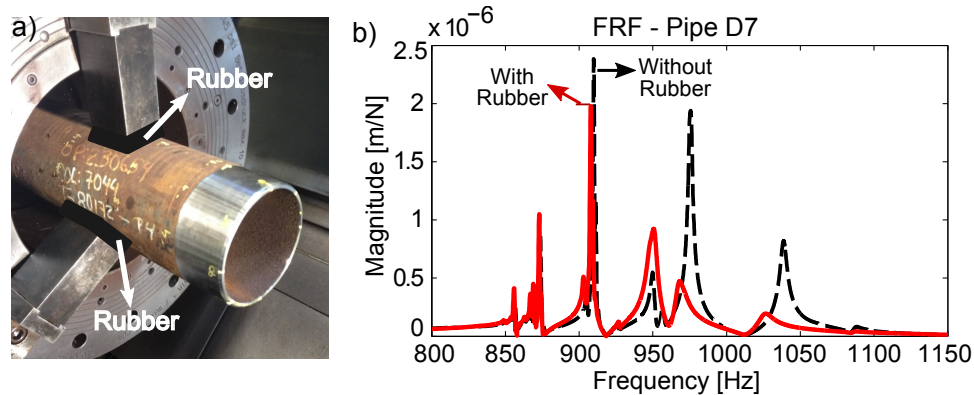


Figure 5.25: Effect of adding rubber between the pipe and the clamping jaws, a) pipe D7 with the added rubber, b) measured radial FRFs at the tip with and without the rubber.

the dominant mode has a shell behaviour, and adding rubber at the chuck does not absorb the shell vibrations at the tip.

5.7.2 Using Different Spindle Speeds For Subsequent Passes

In typical turning operations, chip regeneration can be disrupted by continuous spindle speed variation. In threading processes, however, the axial feed is locked to the spindle speed based on the thread pitch. Due to the limited bandwidth of servo drives, change in the spindle speed can cause lead errors in the thread path. While some modern machine tools claim to have achieved the required precision, spindle speed variation during threading is still not recommended.

However, using a similar idea, the effect of vibration marks from the previous passes can be attenuated by selecting slightly different spindle speeds for subsequent passes. The feasibility of this approach has been tested experimentally in threading pipe D7 with Ceratizit 5-point buttress insert. In the first set, two passes with infeed value of $0.020''$ (0.508 mm)/pass were cut both at spindle speed of 250 rpm. The first pass was stable and the second pass was unstable. The process was repeated on a similar pipe with the same infeed values, but this time the second pass was performed at 225 rpm, which eliminated chatter. Figure 5.26 shows the recorded sound signals and their frequency contents for the second passes in each set. It can be seen that the process has not exhibited chatter vibrations in the case of using different spindle speeds (Figure 5.26.c).

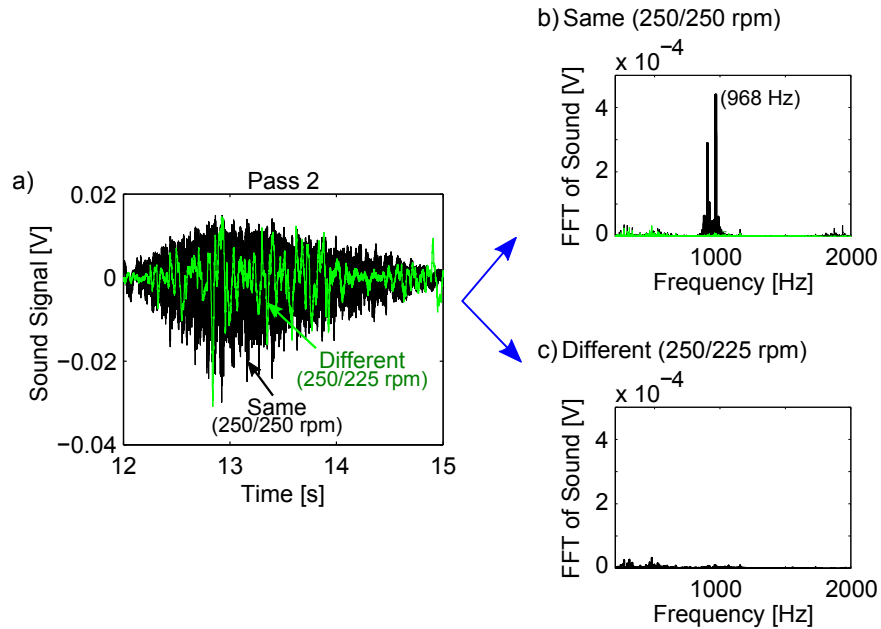


Figure 5.26: Effect of using different speeds for chatter suppression (pipe D7, infeed: 0.020'' (0.508 mm), Ceratizit 5-point buttress insert, Set 1: two passes both at 250 rpm, Set 2: first pass at 250 rpm and second pass at 225 rpm): a) recorded sound data during the second pass in each set, b-c) frequency contents of the sound signal for each case.

5.8 Threading Toolbox Simulation Software

The threading models developed in this thesis have been implemented in a simulation engine along with a user interface in MATLAB. The research software, called *Threading Toolbox*, has been released as one of the modules of CUTPRO[®] Virtual Machining software. It is currently being used by the collaborating company (TenarisTAMSA) in analyzing the threading process of oil pipes.

Figure 5.27 shows the interface of the developed threading toolbox. The geometry of the custom multi-point insert is imported as a DXF file directly from a CAD model. The workpiece material can be selected from the available library, or the cutting force coefficients can be directly entered based on linear or Kienzle force models. The software operates in two modes: simulation and optimization. In the simulation mode, the user selects the infeed settings, i.e. infeed strategy, number of passes, and infeed per pass. The threading engine then simulates the following outputs for each tooth and over each pass: chip geometry (including engagement length and chip area), axial/radial/tangential cutting forces, spindle torque and power. The

numerical results can be exported as a CSV file to MS Excel for further analysis.

Alternatively, the software can be used in optimization mode for process planning. Instead of choosing the number of passes and infeed values, the user selects the final thread depth and imposes optional constraints on minimum/maximum chip thickness, cutting forces, spindle torque/power, and stability margin (see Section 4.11 for constraints). The threading engine then finds the required number of passes and infeed values to achieve highest productivity while respecting all the defined constraints.

The developed research software can be used not only for process planning in manufacturing units but also as a design tool for optimization of threading inserts.

5.9 Summary

This chapter investigates the threading process of thin-walled workpieces with specific application to oil pipes. Dominant mode shapes of sample pipes have been determined using finite element and experimental modal analysis. Extensive threading experiments have been conducted on real scale oil pipes, and the results have been compared against the predictions.

It has been shown that the proposed model can reliably predict the stability of the process for different setup dynamics, cutting conditions, and insert geometries. Sample approaches for chatter suppression have been suggested, and their effectiveness has been demonstrated experimentally. All the developed models have been implemented in a simulation engine which can be used for process planning and insert design.

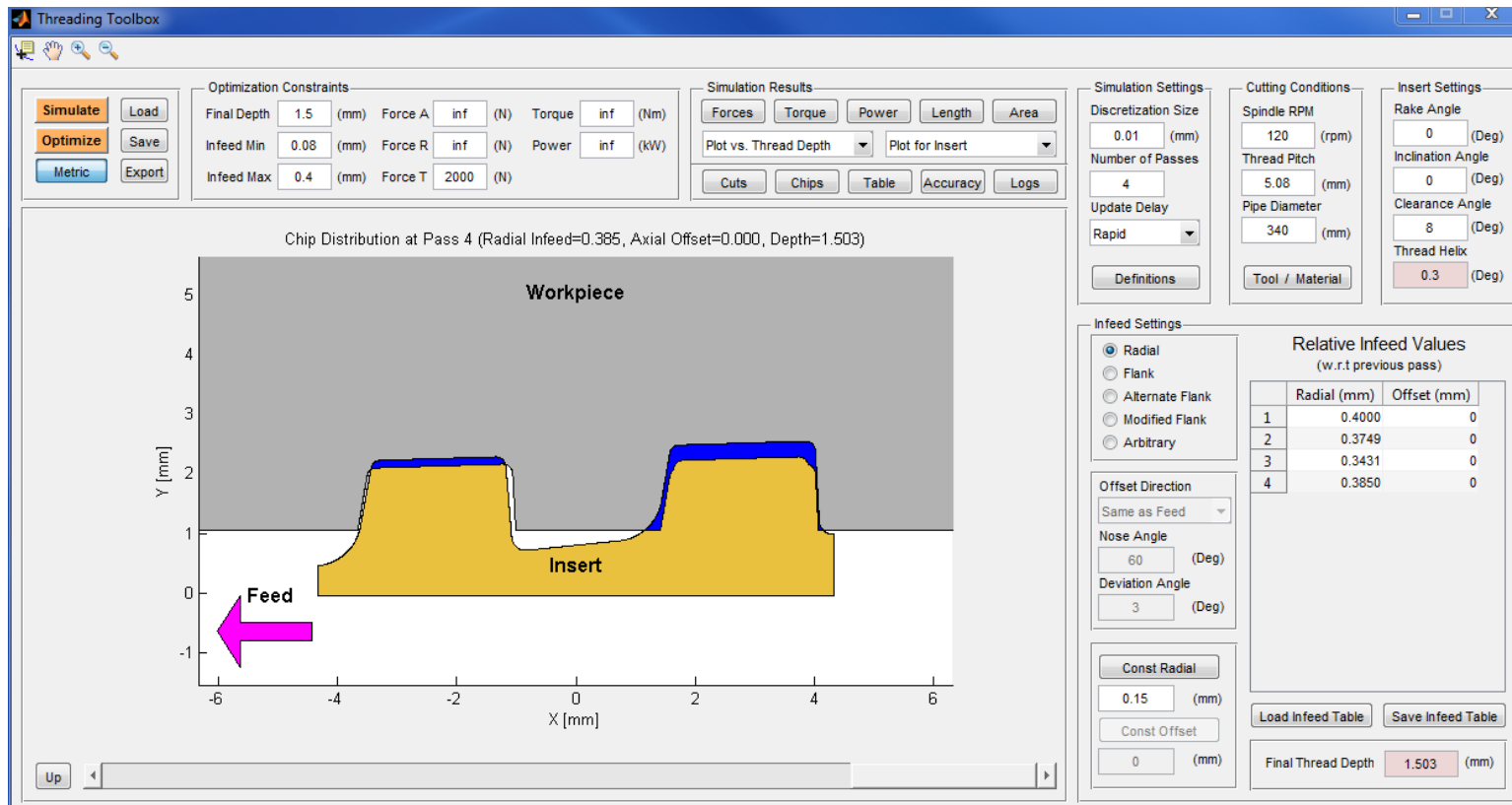


Figure 5.27: User interface of the developed *Threading Toolbox* software package.

Chapter 6

Conclusions and Future Directions

6.1 Summary and Contributions

Accuracy and surface quality of threads is crucial in applications such as offshore pipelines where strong sealing is required. Geometrical errors and vibration marks left during the machining process can lead to stress concentration, fatigue failure, and leakage of the joint. A model which can predict the behaviour of the process ahead of time provides a systematic tool to optimize the cutting tools and process parameters without costly trials.

There are numerous challenges in modelling the mechanics and dynamics of multi-point thread turning. Since threading is a form cutting operation, the resultant chip can have complex geometries. Not only the chip thickness but also the effective oblique cutting angles and direction of local forces can vary significantly along the cutting edge. Due to varying local approach angle, relative vibrations between the tool and workpiece can also have different effect on the local chip thickness. Chip regeneration mechanism in multi-point threading is different than regular turning; since the tool moves one thread pitch over each spindle revolution, the previous vibration marks left by each tooth affects the chip thickness on a different tooth. Threading thin-walled oil pipes involves additional complexities due to the structural beam and shell mode vibrations of the pipe.

This thesis develops a generalized model to determine the chip geometry, cutting forces, and stability during threading of oil pipes. The main contributions can be summarized as:

- A novel semi-analytical methodology has been developed to model the chip geometry for multi-point inserts with custom tooth profiles and arbitrary in-feed plans. The proposed method categorizes possible cases of tool-workpiece engagements, and uses the kinematics of the process and geometrical parameters of the insert to determine the boundaries of the chip. Special cases such as partial root engagement can be modelled as well.
- A systematic discretization method has been developed to divide the chip area along the cutting edge based on the chip flow direction. The algorithm is efficiently run only on a small moving window, and can consider the effect of chip compression (interference) at highly curved segments of the profile.
- A novel cutting force calculation model for threading inserts has been proposed. The local effective oblique cutting angles are systematically determined by defining local coordinate systems and oblique vectors. Cutting force coefficients are evaluated locally for each chip element using nonlinear Kienzle force model and local orthogonal-to-oblique transformations.
- A generalized chip regeneration model for multi-point threading has been developed. The three-dimensional vibrations of the tool and workpiece have been projected in the local chip thickness direction at each point along the cutting edge. The effect of current and previous vibrations on chip thickness have been modelled for the general case where the teeth have different profiles.
- The delay differential equation representing the three-dimensional dynamics of multi-point threading has been developed. Process damping forces are calculated locally by projecting the vibration velocity in the direction of chip thickness at each point along the cutting edge. Dynamic cutting forces are evaluated from chip thickness variation due to the current and previous vibrations. State space representation of dynamic equation of motion in modal space has been derived. A time-marching numerical method based on semi-discretization and Simpson's integration rule has been presented to simulate the vibrations and dynamic forces during the threading operation.
- A chatter stability model for multi-point threading has been developed. Given the insert geometry and structural dynamics of the tool and workpiece, the

model can generate stability diagrams for each pass showing the maximum allowed infeed at each spindle speed.

- A novel dynamic model for threading thin-walled workpieces have been proposed by modelling the effect of residual shell vibrations on chip thickness. The circumference of the workpiece is discretized, and the dynamic equation of motion is solved in modal space to find the instantaneous vibrations at each point along the circumference.
- An optimization algorithm has been developed to plan the number of passes and infeed settings for each pass. The algorithm can consider user-defined constraints on: spindle torque/power, axial/radial/tangential forces on each tooth, and minimum/maximum chip thickness on each tooth. The process is optimized based on stability, productivity, uniform load distribution over different passes, tooth breakage avoidance, chip evacuation, and surface quality.
- As a practical application, threading real scale oil pipes has been investigated experimentally. It has been shown that the developed models can predict the stability of the process with reasonable accuracy.
- A threading simulation software (*Threading Toolbox*) has been developed for industrial use. It can be used not only for process planning but also as a design tool for optimization of the cutting inserts and tooling systems.

6.2 Future Research Directions

The models presented in this thesis are the first iteration in generalized modelling of thread turning operations. There are still several aspects of this research which can be further refined or extended:

- Cutting force coefficients in this thesis are identified mechanistically through cutting experiments. Semi-analytical methods such as slip line field [78] and finite element models can be used to predict the coefficients based on material's characteristics and cutting edge parameters.
- Chip evacuation is a serious issue in threading. While chip geometry and discretization has been presented in this thesis, the three-dimensional chip

flow [84] was not modelled. Finite element methods can be used to simulate the chip formation process.

- The accuracy of cutting force prediction can be improved by including the effect of strain hardening [10] over subsequent passes. Finite element models must be developed to study the effect of ploughing on surface hardness and cutting force coefficients.
- Thermal models [85] can be developed to investigate temperature distribution and optimize the insert coating accordingly.
- Structural dynamics of thin-walled pipes were mainly identified experimentally in this thesis. Finite element models can be developed by defining realistic contact conditions between the jaws and cylindrical workpiece.
- The effect of varying structural dynamics of the pipe as a result of material removal has not been considered in this thesis. Online FRF updating methods [82] can be used to re-evaluate the dynamic parameters during the threading operation.
- Active damping control techniques along with magnetic actuators can be used to suppress the vibrations in real time.

The ultimate goal would be to accurately model chip formation, stress and temperature distribution, cutting forces, stability, surface finish, and tribological characteristics of the final threads.

Bibliography

- [1] Rezayi Khoshdarregi, M., and Altintas, Y., 2015. “Generalized modeling of chip geometry and cutting forces in multi-point thread turning”. *International Journal of Machine Tools and Manufacture*, **98**, pp. 21–32. → cited on p. v, 46
- [2] Smith, G. T., 1989. *Advanced Machining: The Handbook of Cutting Technology*. IFS/Springer-Verlag. → cited on p. 1
- [3] Cao, T., and Sutherland, J. W., 2002. “Investigation of thread tapping load characteristics through mechanistics modeling and experimentation”. *International Journal of Machine Tools and Manufacture*, **42**(14), pp. 1527–1538. → cited on p. 1
- [4] Carla Araujo, A., Luis Silveira, J., Jun, M. B. G., Kapoor, S. G., and DeVor, R., 2006. “A model for thread milling cutting forces”. *International Journal of Machine Tools and Manufacture*, **46**(15), pp. 2057–2065. → cited on p. 1, 8
- [5] API Standard-Spec 5B : Specification for Threading, Gauging and Thread Inspection of Casing, Tubing, and Line Pipe Threads, 2008. American Petroleum Institute. → cited on p. 2, 39
- [6] Shahani, A. R., and Sharifi, S. M. H., 2009. “Contact stress analysis and calculation of stress concentration factors at the tool joint of a drill pipe”. *Materials and Design*, **30**(9), pp. 3615–3621. → cited on p. 6
- [7] Luo, S., and Wu, S., 2013. “Effect of stress distribution on the tool joint failure of internal and external upset drill pipes”. *Materials and Design*, **52**, pp. 308–314. → cited on p. 6
- [8] Yuan, G., Yao, Z., Han, J., and Wang, Q., 2004. “Stress distribution of oil tubing thread connection during make and break process”. *Engineering Failure Analysis*, **11**(4), pp. 537–545. → cited on p. 6
- [9] Ibrahmi, A., Hbaieb, M., and Krichen, A., 2017. “Experimental study of the effect of the threading process on the mechanical and tribological behaviors of

- the triangular thread”. *The International Journal of Advanced Manufacturing Technology*, **88**(1), pp. 269–276. → cited on p. 6
- [10] Fetullazade, E., Akyildiz, H. K., and Saritas, S., 2010. “Effects of the machining conditions on the strain hardening and the residual stresses at the roots of screw threads”. *Materials and Design*, **31**(4), pp. 2025–2031. → cited on p. 7, 116
- [11] Akyildiz, H. K., and Livatyali, H., 2010. “Effects of machining parameters on fatigue behavior of machined threaded test specimens”. *Materials and Design*, **31**(2), pp. 1015–1022. → cited on p. 7
- [12] Klocke, F., Gorgels, C., and Herzhoff, S., 2011. “Tool load during multi-flank chip formation”. In *Modelling of Machining Operations*, Vol. 223 of *Advanced Materials Research*, Trans Tech Publications, pp. 525–534. → cited on p. 7
- [13] Erkorkmaz, K., Katz, A., Hosseinkhani, Y., Plakhotnik, D., Stautner, M., and Ismail, F., 2016. “Chip geometry and cutting forces in gear shaping”. *CIRP Annals - Manufacturing Technology*, **65**(1), pp. 133 – 136. → cited on p. 7
- [14] Bouzakis, K.-D., Friderikos, O., and Tsiafis, I., 2008. “FEM-supported simulation of chip formation and flow in gear hobbing of spur and helical gears”. *CIRP Journal of Manufacturing Science and Technology*, **1**(1), pp. 18 – 26. → cited on p. 7
- [15] Brecher, C., Klocke, F., Brumm, M., and Hardjosuwito, A., 2013. *Analysis and Optimization of Bevel Gear Cutting Processes by Means of Manufacturing Simulation*. Springer Berlin Heidelberg, Berlin, Heidelberg, pp. 271–284. → cited on p. 7
- [16] Fromentin, G., and Poulachon, G., 2010. “Geometrical analysis of thread milling-part 1: Evaluation of tool angles”. *International Journal of Advanced Manufacturing Technology*, **49**(1-4), pp. 73–80. → cited on p. 8
- [17] Fromentin, G., and Poulachon, G., 2010. “Geometrical analysis of thread milling-part 2: Calculation of uncut chip thickness”. *International Journal of Advanced Manufacturing Technology*, **49**(1-4), pp. 81–87. → cited on p. 8
- [18] Jun, M. B. G., and Araujo, A. C., 2010. “Modeling of the thread milling operation in a combined thread/drilling operation: Thrilling”. *Journal of Manufacturing Science and Engineering*, **132**(1), p. 014505. → cited on p. 8
- [19] Wan, M., and Altintas, Y., 2014. “Mechanics and dynamics of thread milling process”. *International Journal of Machine Tools and Manufacture*, **87**, pp. 16–26. → cited on p. 8

- [20] Insperger, T., and Stepan, G., 2004. “Updated semi-discretization method for periodic delay-differential equations with discrete delay”. *International Journal for Numerical Methods in Engineering*, **61**(1), pp. 117–141. → cited on p. 8, 9, 61, 62, 83
- [21] Araujo, A. C., Mello, G. M., and Cardoso, F. G., 2015. “Thread milling as a manufacturing process for API threaded connection: Geometrical and cutting force analysis”. *Journal of Manufacturing Processes*, **18**, pp. 75–83. → cited on p. 8
- [22] Eynian, M., and Altintas, Y., 2009. “Chatter stability of general turning operations with process damping”. *Journal of Manufacturing Science and Engineering*, **131**(4), p. 041005. → cited on p. 8, 98
- [23] Reddy, R. G., Ozdoganlar, O. B., Kapoor, S. G., DeVor, R. E., and Liu, X., 2002. “A stability solution for the axial contour-turning process”. *Journal of Manufacturing Science and Engineering*, **124**(3), p. 581. → cited on p. 8
- [24] Lazoglu, I., Atabey, F., and Altintas, Y., 2002. “Dynamics of boring processes: Part III-time domain modeling”. *International Journal of Machine Tools and Manufacture*, **42**(14), pp. 1567–1576. → cited on p. 8
- [25] Ozlu, E., and Budak, E., 2007. “Analytical modeling of chatter stability in turning and boring operations-Part I: model development”. *Journal of Manufacturing Science and Engineering*, **129**(4), p. 726. → cited on p. 8, 9
- [26] Akyildiz, H. K., and Livatyali, H., 2011. “Prediction and experimental analysis of cutting forces during machining of precision external threads”. *Machining Science and Technology*, **15**(4), pp. 485–506. → cited on p. 8
- [27] Akyildiz, H. K., 2013. “Evaluating of cutting forces in thread machining”. *The International Journal of Advanced Manufacturing Technology*, **68**(5-8), pp. 1601–1612. → cited on p. 8
- [28] Fetullazade, E., Akyildiz, H., and Livatyali, H., 2003. “The determination of shear angle in cutting processes of complex shaped part”. In *Second Machine Design and Manufacturing Technology Congress*, pp. 13–29. → cited on p. 8
- [29] Kafkas, F., 2010. “An experimental study on cutting forces in the threading and the side cut turning with coated and uncoated grades”. *Journal of Manufacturing Science and Engineering*, **132**(4), p. 041012. → cited on p. 8
- [30] Taylor, F., 1907. *On the Art of Cutting Metals*. American society of mechanical engineers. → cited on p. 9
- [31] Tobias, S., 1965. *Machine-tool vibration*. J. Wiley. → cited on p. 9

- [32] Koenigsberger, F., and Tlustý, J., 1970. *Machine tool structures*. Pergamon Press. → cited on p. 9
- [33] Merritt, H., 1965. “Theory of self-excited machine-tool chatter: Contribution to machine-tool chatter research”. *ASME Journal of Engineering Industry*, **87**(4), pp. 447–454. → cited on p. 9
- [34] Schmitz, T. L., and Smith, K. S., 2008. *Machining Dynamics: Frequency Response to Improved Productivity*. Springer Science & Business Media. → cited on p. 9
- [35] Altintas, Y., and Weck, M., 2004. “Chatter stability of metal cutting and grinding”. *CIRP Annals - Manufacturing Technology*, **53**(2), pp. 619 – 642. → cited on p. 9
- [36] Minis, I., Yanushevsky, R., Tembo, A., and Hocken, R., 1990. “Analysis of linear and nonlinear chatter in milling”. *CIRP Annals - Manufacturing Technology*, **39**(1), pp. 459 – 462. → cited on p. 9
- [37] Budak, E., and Altintas, Y., 1998. “Analytical prediction of chatter stability in milling, part i: General formulation”. *Journal of Dynamic Systems, Measurement, and Control*, **120**(1), Mar., pp. 22–30. → cited on p. 9
- [38] Insperger, T., and Stepan, G., 2002. “Semi-discretization method for delayed systems”. *International Journal for Numerical Methods in Engineering*, **55**(5), pp. 503–518. → cited on p. 9, 11
- [39] Ding, Y., Zhu, L., Zhang, X., and Ding, H., 2010. “A full-discretization method for prediction of milling stability”. *International Journal of Machine Tools and Manufacture*, **50**(5), pp. 502 – 509. → cited on p. 9, 83
- [40] Ding, Y., Zhu, L., Zhang, X., and Ding, H., 2011. “Numerical integration method for prediction of milling stability”. *Journal of Manufacturing Science and Engineering*, **133**(3), p. 031005. → cited on p. 9, 62
- [41] Asl, F. M., and Ulsoy, A. G., 2003. “Analysis of a system of linear delay differential equations”. *Journal of Dynamic Systems, Measurement, and Control*, **125**(2), June, pp. 215–223. → cited on p. 9
- [42] Butcher, E. A., Ma, H., Bueler, E., Averina, V., and Szabo, Z., 2004. “Stability of linear time-periodic delay-differential equations via chebyshev polynomials”. *International Journal for Numerical Methods in Engineering*, **59**(7), pp. 895–922. → cited on p. 9

- [43] Mann, B. P., Young, K. A., Schmitz, T. L., and Dilley, D. N., 2004. “Simultaneous stability and surface location error predictions in milling”. *Journal of Manufacturing Science and Engineering*, **127**(3), July, pp. 446–453. → cited on p. 9
- [44] Eksioğlu, C., Kilic, Z. M., and Altintas, Y., 2012. “Discrete-time prediction of chatter stability, cutting forces, and surface location errors in flexible milling systems”. *ASME Journal of Manufacturing Science and Engineering*, **134**(6), pp. 061006–13. → cited on p. 9, 59, 81, 83
- [45] Honeycutt, A., and Schmitz, T. L., 2016. “A new metric for automated stability identification in time domain milling simulation”. *Journal of Manufacturing Science and Engineering*, **138**(7), Mar., pp. 074501–074501–7. → cited on p. 9
- [46] Lazoglu, I., Vogler, M., Kapoor, S. G., and DeVor, R. E., 1998. “Dynamics of the simultaneous turning process”. *Transactions of NAMRI/SME*, **26**, pp. 135–139. → cited on p. 9, 10
- [47] Budak, E., and Ozturk, E., 2011. “Dynamics and stability of parallel turning operations”. *CIRP Annals - Manufacturing Technology*, **60**(1), pp. 383–386. → cited on p. 10
- [48] Brecher, C., Epple, A., Neus, S., and Fey, M., 2015. “Optimal process parameters for parallel turning operations on shared cutting surfaces”. *International Journal of Machine Tools and Manufacture*, **95**, pp. 13–19. → cited on p. 10
- [49] Albrecht, P., 1960. “New developments in the theory of the metal-cutting process: Part I. The ploughing process in metal cutting”. *Journal of Engineering for Industry*, **82**(4), pp. 348–357. → cited on p. 10
- [50] Sisson, T. R., and Kegg, R. L., 1969. “An explanation of low-speed chatter effects”. *Journal of Engineering for Industry*, **91**(4), pp. 951–958. → cited on p. 10
- [51] Shaw, C., and Desalvo, G. J., 1970. “On the plastic flow beneath a blunt axisymmetric indenter”. *Journal of Engineering for Industry*, **92**(2), pp. 480–492. → cited on p. 10, 53
- [52] Chiou, R. Y., and Liang, S. Y., 1998. “Chatter stability of a slender cutting tool in turning with tool wear effect”. *International Journal of Machine Tools and Manufacture*, **38**(4), pp. 315–327. → cited on p. 10, 54
- [53] Clancy, B. E., and Shin, Y. C., 2002. “A comprehensive chatter prediction model for face turning operation including tool wear effect”. *International*

- Journal of Machine Tools and Manufacture*, **42**(9), pp. 1035 – 1044. → cited on p. 10
- [54] Altintas, Y., Eynian, M., and Onozuka, H., 2008. “Identification of dynamic cutting force coefficients and chatter stability with process damping”. *CIRP Annals - Manufacturing Technology*, **57**(1), pp. 371–374. → cited on p. 10
- [55] Budak, E., and Tunc, L. T., 2009. “A new method for identification and modeling of process damping in machining”. *Journal of Manufacturing Science and Engineering*, **131**(5), p. 051019. → cited on p. 10
- [56] Ahmadi, K., and Altintas, Y., 2014. “Identification of machining process damping using output-only modal analysis”. *ASME Journal of Manufacturing Science and Engineering*, **136**(c), pp. 1–56. → cited on p. 10
- [57] Ahmadi, K., 2017. “Analytical investigation of machining chatter by considering the nonlinearity of process damping”. *Journal of Sound and Vibration*, **393**, pp. 252 – 264. → cited on p. 10
- [58] Tyler, C. T., Troutman, J. R., and Schmitz, T. L., 2016. “A coupled dynamics, multiple degree of freedom process damping model, part 1: Turning”. *Precision Engineering*, **46**, pp. 65 – 72. → cited on p. 10
- [59] Meirovitch, L., 1967. *Analytical methods in vibrations*. Series in advanced mathematics and theoretical physics. Macmillan. → cited on p. 11
- [60] Leissa, A., 1973. *Vibration of shells*. NASA. Scientific and Technical Information Office, National Aeronautics and Space Administration. → cited on p. 11
- [61] Love, A., 1892-2013. *A Treatise on the Mathematical Theory of Elasticity*. Cambridge University Press. → cited on p. 11
- [62] Donnell, L., 1933. *Stability of Thin-walled Tubes Under Torsion*. NACA-R-479. NACA. → cited on p. 11
- [63] Evensen, D. A., 1963. “Some observations on the nonlinear vibration of thin cylindrical shells”. *AIAA Journal*, **1**(12), Dec., pp. 2857–2858. → cited on p. 11
- [64] Evensen, D. A., 1966. “Nonlinear flexural vibrations of thin circular rings”. *Journal of Applied Mechanics*, **33**(3), Sept., pp. 553–560. → cited on p. 11
- [65] Dowell, E., and Ventres, C., 1968. “Modal equations for the nonlinear flexural vibrations of a cylindrical shell”. *International Journal of Solids and Structures*, **4**(10), pp. 975 – 991. → cited on p. 11, 78

- [66] Rahman, M., and Ito, Y., 1985. “Stability analysis of chatter vibration in turning processes”. *Journal of Sound and Vibration*, **102**(4), pp. 515 – 525. → cited on p. 11
- [67] Lai, G., and Chang, J., 1995. “Stability analysis of chatter vibration for a thin-wall cylindrical workpiece”. *International Journal of Machine Tools and Manufacture*, **35**(3), pp. 431 – 444. → cited on p. 11
- [68] Dospel, V., and Keskinen, E., 2011. “Thin-shell response to machining loads”. In ASME 2011 International Mechanical Engineering Congress and Exposition, Vol. 7, pp. 413–422. → cited on p. 11
- [69] Chanda, A., Fischer, A., Eberhard, P., and Dwivedy, S. K., 2014. “Stability analysis of a thin-walled cylinder in turning operation using the semi-discretization method”. *Acta Mechanica Sinica*, **30**(2), pp. 214–222. → cited on p. 11
- [70] Chen, D., Lin, B., Han, Z., and Zhang, Y., 2013. “Study on the optimization of cutting parameters in turning thin-walled circular cylindrical shell based upon cutting stability”. *The International Journal of Advanced Manufacturing Technology*, **69**(1), pp. 891–899. → cited on p. 11
- [71] Fischer, A., and Eberhard, P., 2012. “Simulation-based stability analysis of a thin-walled cylinder during turning with improvements using an adaptronic turning chisel”. *Archive of Mechanical Engineering*, **58**(4), p. 367391. → cited on p. 11
- [72] Mehdi, K., Rigal, J.-F., and Play, D., 2002. “Dynamic behavior of a thin-walled cylindrical workpiece during the turning process, part 1: Cutting process simulation”. *Journal of Manufacturing Science and Engineering*, **124**(3), July, pp. 562–568. → cited on p. 11
- [73] Mehdi, K., Rigal, J.-F., and Play, D., 2002. “Dynamic behavior of a thin-walled cylindrical workpiece during the turning-cutting process, part 2: Experimental approach and validation”. *Journal of Manufacturing Science and Engineering*, **124**(3), July, pp. 569–580. → cited on p. 11
- [74] Lorong, P., Larue, A., and Perez Duarte, A., 2011. “Dynamic study of thin wall part turning”. In Modelling of Machining Operations, Vol. 223 of *Advanced Materials Research*, Trans Tech Publications, pp. 591–599. → cited on p. 11
- [75] Stabler, G., 2012. “The chip flow law and its consequences”. *Advances in Machine Tool Design and Research*, pp. 243–251. → cited on p. 29, 34

- [76] Kaymakci, M., Kilic, Z. M., and Altintas, Y., 2012. “Unified cutting force model for turning, boring, drilling and milling operations”. *International Journal of Machine Tools and Manufacture*, **54-55**, pp. 34–45. → cited on p. 34
- [77] Kienzle, O., 1951. “Die Bestimmung von Kräften und Leistungen an spänenden Werkzeugen und Werkzeugmaschinen”. *Zeitschrift des Vereines Deutscher Ingenieure (Z-VDI)*, **94**, pp. 299–305. → cited on p. 34
- [78] Jin, X., and Altintas, Y., 2011. “Slip-line field model of micro-cutting process with round tool edge effect”. *Journal of Materials Processing Technology*, **211(3)**, pp. 339 – 355. → cited on p. 35, 115
- [79] Cutpro advanced machining simulation software (ver. 9.3). → cited on p. 37, 39
- [80] Hartung, F., Insperger, T., Stepan, G., and Turi, J., 2006. “Approximate stability charts for milling processes using semi-discretization”. *Applied Mathematics and Computation*, **174(1)**, pp. 51 – 73. → cited on p. 70
- [81] Chang, J., Lai, G., and Chen, M., 1994. “A study on the chatter characteristics of the thin wall cylindrical workpiece”. *International Journal of Machine Tools and Manufacture*, **34(4)**, pp. 489 – 498. → cited on p. 78
- [82] Tuysuz, O., and Altintas, Y., 2017. “Frequency domain prediction of varying thin-walled workpiece dynamics in machining”. *Journal of Manufacturing Science and Engineering*, **139(7)**, pp. 071013–16. → cited on p. 91, 106, 116
- [83] Altintas, Y., 2012, 2002. *Manufacturing Automation: Metal Cutting Mechanics, Machine Tool Vibrations, and CNC Design*. Cambridge University Press. → cited on p. 92, 93
- [84] Jawahir, I., and van Luttervelt, C., 1993. “Recent developments in chip control research and applications”. *CIRP Annals - Manufacturing Technology*, **42(2)**, pp. 659 – 693. → cited on p. 116
- [85] Islam, C., Lazoglu, I., and Altintas, Y., 2015. “A three-dimensional transient thermal model for machining”. *Journal of Manufacturing Science and Engineering*, **138(2)**, Sept., pp. 021003–021003–17. → cited on p. 116

Appendix A

Mode Shape Extraction From ANSYS

After building the geometry and meshing, copy the following code in the Session Editor of ANSYS

```
! SOLVE THE EVP
ANTYPE, 2           ! Modal analysis
MODOPT,LANB,20     ! Block Lancos, number of modes
EQSLV,FRONT       ! Frontal Solver
MXPAND,20         ! Expand number of modes

SOLVE
FINISH
/POST1
SET, LIST

!! Output the eigen values
/output, , frq
set, list
/output, term
```

The following lines write the eigen values and the mass-normalized mode shape vectors to the text file

```
nset, s, node, , 2 ! TCP
nset, a, node, , 4 ! Repeat for all nodes of interest
/output, , eig

*do, i, 0, 10      ! no of modes
    set, , i
    /page, , , 200
    prdisp
*enddo
/output, term
```